RESERVOIR GEOPHYSICS

DEPARTMENT OF EARTH SCIENCE
UNIVERSITY OF BERGEN

Master thesis

Acoustic Signatures of Gas Hydrates Observations and Modelling

---

JØRGEN TVEIT

June 1, 2017

Abstract

Interpretation of a Bottom Simulating Reflector (BSR) associated with gas hydrate accumulations in seismic, depend on gas hydrate saturation and distribution in pore voids. The BSR cannot predict gas hydrate saturation or distribution in pore voids. Hence, forward rock physics techniques are extensively used to quantify gas hydrate accumulations. This thesis work utilize rock physics and seismic modelling to observe the seismic response of different gas hydrate saturations and distributions. Detection and mapping of gas hydrates are important because of: their energy potential, role as a geo-hazard, and effect on the global climate change. It is important to develop an understanding related to gas hydrate distribution in sediments. In order to prevent slope instabilities, release of greenhouse gases into oceans/atmosphere, and potentially producing methane gas for energy consumption.

Three pore-void distribution schemes are proposed, where gas hydrates, 1) cement grains at grain-contact, 2) cement entire grains, and 3) are deposited away from grain-contact. Scheme 1) and 2) have been related to major increase in sediment stiffness, while scheme 3) display little or no effect. Gas hydrates have been encountered where no BSR reflection is observed in seismic, which means that the BSR has limitations associated with small gas hydrate saturations.

Different cases are outlined in this study, in order to look at both gas hydrate and free gas effect on the BSR. Free gas have a great impact on seismic reflections, because it decrease the P-wave velocity of sediments greatly. For smaller gas hydrate saturations the study reveals that free gas make the greatest contribution to the observed BSR reflection. For gas hydrates cementing grains at higher saturations, the increased sediment stiffness result in a strong velocity contrast even without free gas beneath. A correlation model between gas hydrate saturation and distribution reveals that cementation of grains occur at a specific critical saturation. Synthetic seismic sections are based on the gas hydrate system at the Storegga slide area outside the mid-Norwegian margin. Comparison with real seismic data, reveals that the observed BSR at this area mainly arise from free gas situated below the BSR. Results in this thesis sheds light on the importance of understanding gas hydrate formation and distribution in sediments, to better interpret the BSR.

Acknowledgments

This thesis work has been written at the University of Bergen, at the Department of Earth Science, and I would like to thank the University for giving me this opportunity.
Writing this thesis has been both challenging and rewarding, in a sense I never would have expected. The end of five long years as a student marks a new chapter in my life, with loads of exciting opportunities ahead. I would like to acknowledge everyone that in some way helped or motivated me during this work.

First and formerly, I would like to thank my supervisor Tor Arne Johansen for his guidance, professional input and for allowing me to work on this topic. I would also like to thank my co-supervisor Berit O. Hjelstuen for helping me out with the seismic data, geology aspects and corrections during this thesis work.

I would like to extend my sincere gratitude to both Åsmund Drottning and Isabelle Lecomte for helping me with MATLAB, NORSAR, and SeisRoX. Without your help and input, this thesis work would have been nearly impossible. Also, a special thanks to Åsmund Drottning and Erling Jensen at Rock Physics Technologies for providing me with a MATLAB-package used in the rock physics modelling.

I would like to thank the University and NORSAR for the academic use of its ray-based software NORSAR-2D, NORSAR-3D, SeisRoX, and its assigned NORSAR 2016 manual.

I would like to thank Tor Arne's research group, for important discussions and input. In addition, I would like to thank my lunch group for keeping my moral up, and listening to all of my complaints and problems along the way.

Also, a thanks to Bjørn Kvamme and the other co-authors of the article I was so fortunate to be a part of during this masters degree.

In the end, I would like to thank my mom and dad, for believing in me and supporting me always. Your support have been crucial during these five years, both emotional and financial.

Contents

Chapter 1

Introduction

1.1 Motivation

Gas hydrates are ice-like compounds consisting of guest gas molecules trapped by a surrounding water molecule lattice (Cage). They form when gas and water comes into high pressure and/or low temperature regions, typical offshore or permafrost areas (Sloan and Koh, 2007). There is a large occurrence of gas hydrates worldwide as illustrated in Figure 1.1, and the amount of natural gas in hydrates exceed the known volume of conventional hydrocarbons. It is estimated that if only 20% of the known gas volume in gas hydrates was produced, the world would have enough energy to last almost 200 years (Makogon, 2010). It is unarguably a great potential energy resource. However, some limitations with gas hydrates are the availability, discontinuous accumulations and the cost to extract the gas from hydrates (Collett, 2002).

It is believed that the world population will increase by 2.6 billion by 2050 [1]. This means that the world will need considerable amounts of energy. While most of the energy today comes from conventional hydrocarbon sources (e.g oil, natural gas, coal), these resources will not meet our energy demands in the future (Makogon et al., 2007). Natural gas trapped inside gas hydrates gives a viable option. By understanding how and where

[1] The population growth is an estimate given in the article by Cohen (2003)

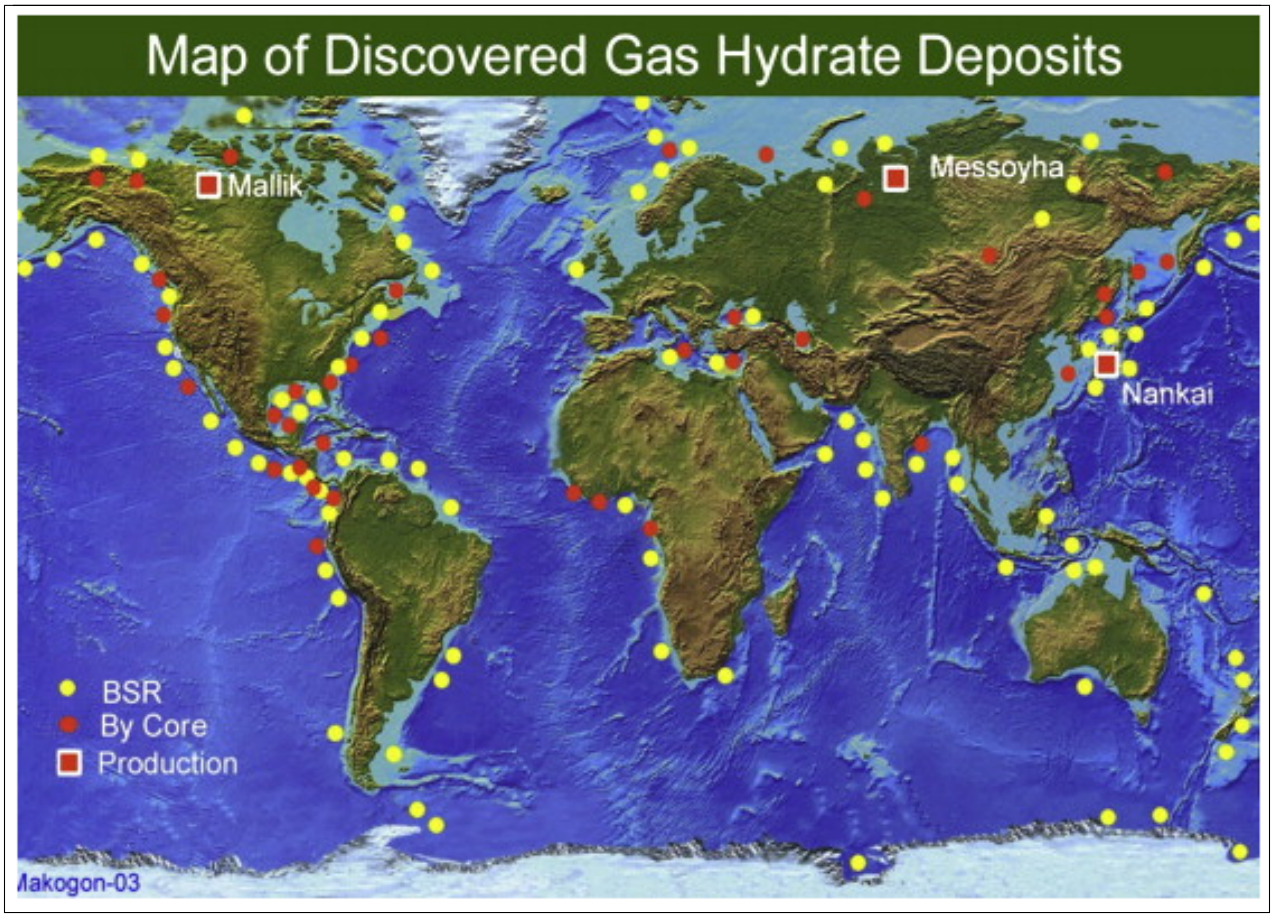

Figure 1.1: Distribution of recovered and inferred gas hydrate accumulations worldwide. Map adopted from (Makogon, 2010)

hydrates are formed, the production cost and availability of the gas can be improved. The first step is to locate the gas hydrate reservoirs. By the use of marine seismic acquisition, gas hydrate bearing sediments can be located by the Bottom Simulating Reflector (BSR). The BSR is a seismic reflector which coincides with the base of the gas hydrate stability zone (BHSZ). The BSR can be detected in seismic from different attributes. The BSR:

- mimic the sea-floor reflector.
- have a reversed negative polarity.
- have a strong amplitude.
- often cross-cut stratigraphic layers.

The reflector is believed to originate from the considerable difference in acoustic impedance between a gas hydrate bearing layer and free gas layer beneath (Mienert et al., 2005).

Dissociation of gas hydrates can be associated with small and large movement of sediments in deep-water ocean environments. The base of gas hydrate stability zone (BGSZ) is temperature and pressure dependent, and is thereby greatly related to changes in temperature, overlying sediments and/or sea level. Gas hydrates may cement grains if the saturation is high enough, creating a temporary stiffness to the sediments. Dissociating hydrates will make the sediments unstable, and the sea-floor may collapse. As an example, it has been suggested by Berndt et al. (2004) that the Storegga slide event was triggered by dissociating gas hydrates. In addition, a major concern for oil and gas platforms are expected in areas with the potential of dissociating hydrates (Maslin et al., 2010). Gas hydrates may also pose as a potential threat when drilling wells, plugging the blow out preventer, making an unsafe environment for platform workers (Sloan and Koh, 2007).

In order to produce methane from gas hydrates, a sufficient volume concentration in the sediment pore voids need to be present. Permafrost areas often exhibit high gas hydrate saturations, while off-shore reservoirs have a low average saturations (Sloan and Koh, 2007). However, the off-shore gas hydrate distribution is vast, and the potential even greater. Some countries such as Japan and Korea import most of their energy today, resulting in huge transportation costs. Several off-shore gas hydrate accumulations have been found in these areas, providing an important opportunity for these countries to become self-reliable in energy (Makogon et al., 2007). Therefore, the search and understanding of reservoirs containing high local gas hydrate saturation off-shore is important to investigate.

The BSR can only give information regarding the presence of gas hydrates, and not the saturation or distribution in the pore voids. In this regard, it is of increasing interest to use forward modelling rock physics techniques in order to compare various saturations and distributions to real seismic data (Sain et al., 2010). Quantification of gas hydrates is important for pre-drilling information or assessment of slope stability.

Forward modelling techniques are used in order to understand which parameters affects the seismic reflections, and how they do it (Guéguen and Palciauskas, 1994). This study will have emphasis on seismic reflections related to the BSR, and will provide a method for investigating gas hydrate saturation and distribution.
There are many aspects when considering the potential and geo-hazards associated with gas hydrates. It is important to know more about the nature of the gas hydrate, how they are distributed in sediment voids, and methods for locating them.

1.2 Objective

The aim for this thesis work is to investigate the gas hydrate saturation effect on seismic reflection data. Small gas hydrate concentrations have reportedly small effects on the seismic reflection, and detection of a BSR is mainly due to trapped gas beneath (Bünz et al., 2005). In order to investigate the gas hydrate saturation effect on the BSR, a hybrid rock physics method coupling Contact Cement Theory (CCT) with the Self Consistent Approximation (SCA), is utilized. The procedure is described by Dvorkin et al. (1999) and Johansen et al. (2003), revolving around gas hydrates cementing grains. Dvorkin et al. (1999) proposed that only small concentrations of cement at grain-contact would increase the stiffness of the sediments remarkably. Distribution of gas hydrates have been proposed to follow four different schemes: 1) hydrates as inclusions in the pore void away from grain contact, 2) hydrate cementing at grain contacts, 3) hydrate cement coating the grains, and 4) hydrates acting as sediment grains (Ecker et al., 1998; Helgerud et al., 1999; Jakobsen et al., 2000; Winters et al., 2004). Schemes 1), 2) and 3) are modeled in this study work. By using a similar procedure described by Johansen et al. (2003), gas hydrates cementing grains can be proposed to occur at a critical saturation. Creating a rock physics model, predicting the gas hydrate saturation where cementing of grains occur, will be of special importance when looking at the BSR reflection associated with gas hydrates.

Seismic modelling is performed by using NORSAR-2D, NORSAR-3D, and SeisRox modelling tools. Geological models are made for three cases, exploring the seismic response between gas hydrate, free gas, and brine-saturated sediments. By investigating the gas hydrate and free gas response on the BSR reflection, important information about

the validity of BSR as a gas hydrate indicator, can be derived. For the purpose of comparing synthetic with real seismic data, the reservoir models have been made similar to the gas hydrate system at the southern Vøring plateau investigated by Bünz et al. (2005) and Andreassen et al. (2003). Geologic information from this area is used in both the rock physics and seismic modelling procedures for all three cases.

1.3 Modelling programs

In this thesis work, rock physics models have been created using the MATLAB software. A MATLAB-package was provided by Erling Jensen and Åsmund Drottning (Rock Physics Technologies). All MATLAB scripts used in this thesis work are based on, or modified from the MATLAB-package.
For the seismic modelling geological models was created using NORSAR-2D, NORSAR-3D, while the ray-based software SeisRoX have been utilized to create seismic images. In addition, PETREL have been used to some degree, in order to present the real seismic data obtained from the DISKOS database.

1.4 Outline

The outline of this thesis will follow the structure below:

Chapter 1: Motivation and objective of the thesis.

Chapter 2: Outline of fundamental theory behind gas hydrates existing in sediments.

Chapter 3: Outline of brief theory and modelling procedures for rock physics and seismic modelling.

Chapter 4: Outline of the methods and data used in the seismic modelling.

Chapter 5: Results obtained from rock physics, and seismic modelling.

Chapter 6: Discussion focused on results obtained, and methods used in this study.

Chapter 7: Concluding remarks, highlighting the most important findings, and suggestions for future work.

Chapter 2

Fundamental Theory

The fundamental theory behind gas hydrates is outlined in this chapter. The chapter will introduce some insight into the nature of gas hydrates, and how they are formed in natural sediments. It is important to understand how and why gas hydrates occur, in order to better predict and understand the BSR in seismic.

2.1 Gas hydrate structure

The hydrogen bonded lattice surrounding the guest molecules in gas hydrates, can have different structures and sizes. Three types of hydrate structures exist (Figure 2.1), cubic structure I and II or hexagonal structure H. Structure I is formed when the guest molecule is small (typical Biogenic source [1]), while structure II forms with larger molecules (Thermogenic hydrocarbon source [2]). Structure H is a very complex structure, which rarely occurs in nature, and form from heavy gas molecules such as iso-pentane or neohexane in mixture with smaller gases (Sloan and Koh, 2007).
Structure l hydrates are the most common structure type occurring in nature. It contains small guest molecules, such as $CH_4, CO_2, N_2, H_2, H_2S, C_{2+}$, where methane

[1] When the guest gas molecule arise from biological degradation of organisms, it is called a Biogenic source

[2] When the guest gas molecule arise from fluid migration of deep conventional hydrocarbon sources, it is called a thermogenic source

(CH_4) hydrates are the most common (Kvenvolden, 1993). Structure ll hydrate form when larger guest molecules, typically C_{3+}, C_{4+} are mixed with water. Most commercialized reservoirs today are associated with structure l and ll hydrates (Sloan, 2003).

Figure 2.1, illustrates the different cavity types observed in gas hydrates. It can be noted that the different cavities have been assigned numbers such as 5^{12}, to explain the different structures. Structure l and ll hydrates consist of guest gas molecules, and water cages structured by hydrogen bonding. Structure l hydrates consist of 2 small cavities (5^{12}), 6 large cavities ($5^{12}6^2$), and 46 water molecules. Structure ll hydrates have 16 small cavities (5^{12}), 8 large ($5^{12}6^4$), and 136 water molecules as observed in Figure 2.1 (Sloan and Koh, 2007). The three different cavity crystals are considered as building blocks in the hydrate.

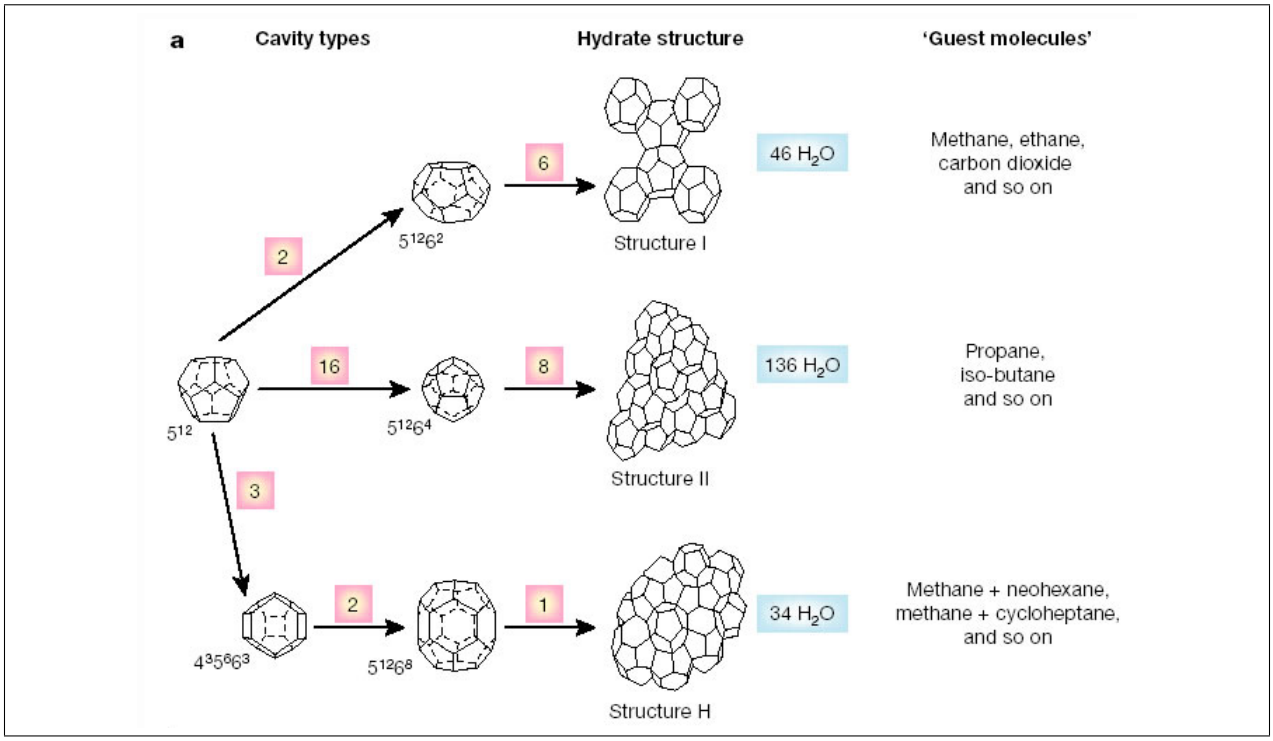

Figure 2.1: Different cavity types, corresponding to structure 1,2, and H. *Source: (Sloan, 2003).*

Pentagonal dodecahedra (5^{12}), have 12 faces bonded together to create the cavity crystal. This crystal fills its cavity with small gas molecules, but for larger gas molecules the strain is to high, causing the hydrogen bonds to break. In order to fill the large cavity and relieve the strain, hexagonal faces ($6^2, 6^4$) are introduced into the pre-existing crystal structure.

Structure l forms tetrakaidecahedron ($5^{12}6^2$) with two hexagonal faces, while structure ll forms hexakaidecahedral ($5^{12}6^4$) with four additional hexagonal faces (Sloan, 2003).
When all hydrate cavities are filled with guest molecules, both structure l and ll have the component concentration of approximately 85 mol% molecules and 15 mol% guest molecules (Sloan, 2003). Consequently gas hydrates have many properties similar to ice. Ice have a hexagonal structure, where each water molecule is hydrogen bonded to four others (Sloan and Koh, 2007). Ice have shear strength compared to fluids (liquid, gas), because structured hydrogen bonds act to stiffen the material. In general, the main difference between ice and hydrates, is the presence of guest molecules. The guest gas molecules alter the hydrogen bonded cage structure, resulting in a different structure with different elastic properties. Gas molecules in hydrates usually lowers the bulk and shear modulus slightly compared to ice.

Several compression tests performed on gas hydrates and sediments containing them, found that the presence of methane hydrates in the pore space, enhanced the compressive strength compared to sediments with no hydrate. Hydrate formation in sediments also depend on the wettability of the rock. For water-wet rocks, the compressive strength increases with the hydrate saturation. For neutral or oil-wet situations, the compressive strength is constant until the hydrate saturation reaches 25% (Sloan and Koh, 2007).

2.2 Stability conditions

Gas hydrates are meta-stable, which means that its stability depend on both temperature and pressure conditions. For gas hydrates to form, four conditions are needed: presence of gas, water, high pressures, and/or low temperatures (Makogon, 2010).
The region where temperature and pressure are at a static equilibrium, is the threshold for hydrate growth or dissociation. The threshold is often called the base of gas hydrate stability zone (BGHS), and coincide with the bottom simulating reflector (BSR) in seismic (Bünz et al., 2005). However, discrepancies have been discovered between the BGHS and the BSR at for example the Blake Ridge field. The deviation in depth at this location is believed to be because water in sediments are much less saline than sea-water, and

presence of other gas molecules such as CO_2 and H_2S may increase the stability. The BGHS is calculated based on laboratory experiments, but in some cases the measured BGHS will be tens of meters different from the observed BSR in seismic (Clennell et al., 1999).

Gas hydrates are confined to the uppermost part of marine sediments, which is due to the positive geothermal gradient down into the earth. The gas hydrate stability depth is confined between the sediment-water interface, and the sub-bottom depth where the geothermal gradient intersects the methane-hydrate-water equilibrium curve (Dickens and Quinby-Hunt, 1997) (Figure 2.2). When gas rises from either a hydrocarbon reservoir below, or a biological source, it is trapped by water molecules. When reaching the temperature/pressure region sufficient for hydrate growth, the water is chilled, and hydrate formation is initiated (Haq, 1999). Although, the hydrate stability zone in Figure 2.2 has a high vertical reach, gas hydrate reservoirs are rarely higher than about 50-100 m above the BGHS. The reason for this is the variation of gas and water influx from below. When hydrates are forming, they are often blocking the pore voids, hence reducing the vertical permeability. When water and gas are prevented to penetrate through the existing hydrate layer, the hydrate formation stops due to a lack of fluid supply (Clennell et al., 1999).

As observed in Figure 2.3, the stability curve shifts to the left when seawater is mixed with methane gas instead of pure water. Only a small fraction (about 1%) of either H_2S, CO_2, ethane or heavier hydrocarbons will have the same effect on the methane hydrate stability, shifting it to the left. This small shift of around 1-2 $^{\circ}C$, might change the BGHS by tens of meters, considering a normal geothermal gradient (Clennell et al., 1999).

2.3 Hydrate formation and dissociation

Maybe the most difficult topic regarding gas hydrates, is how they form, grow, and dissociate (Sloan and Koh, 2007). Hydrate formation and dissociation processes are found through experiments in laboratories for different compositions of gases and water, at

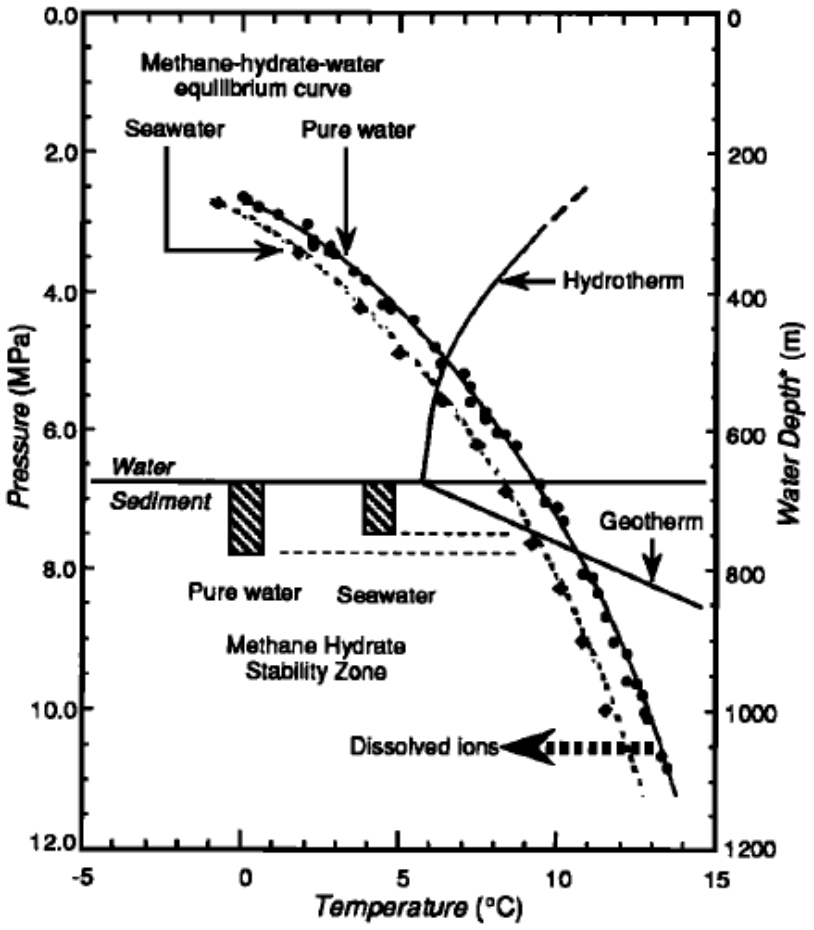

Figure 2.2: The methane hydrate stability zone lies between the water/sediment interface, and the intercept of the geothermal gradient and methane-hydrate-water equilibrium curve. Higher salinity, shifts the curves making the hydrate zone appear shallower, than would be expected. *Source: (Dickens and Quinby-Hunt, 1997).*

different temperatures and pressures. However, laboratory experiments cannot give exact results due to a variety of factors (Buffett and Zatsepina, 2000). Laboratory experiments fail to display the wide range of pressures found in nature, wide range of growth habits, variation of gas influx, and most importantly do not account for the different host sediment effect on hydrate stability (Clennell et al., 1999). Once the pressure and temperature conditions are within the hydrate stability region, an induction time starts. During the induction time, no hydrate is forming due to its meta-stability (ability to stay at a non-equilibrium state for a long period of time). When the hydrate growth is initiated it forms very rapidly, and gas is concentrated and compressed in the hydrate cages. After

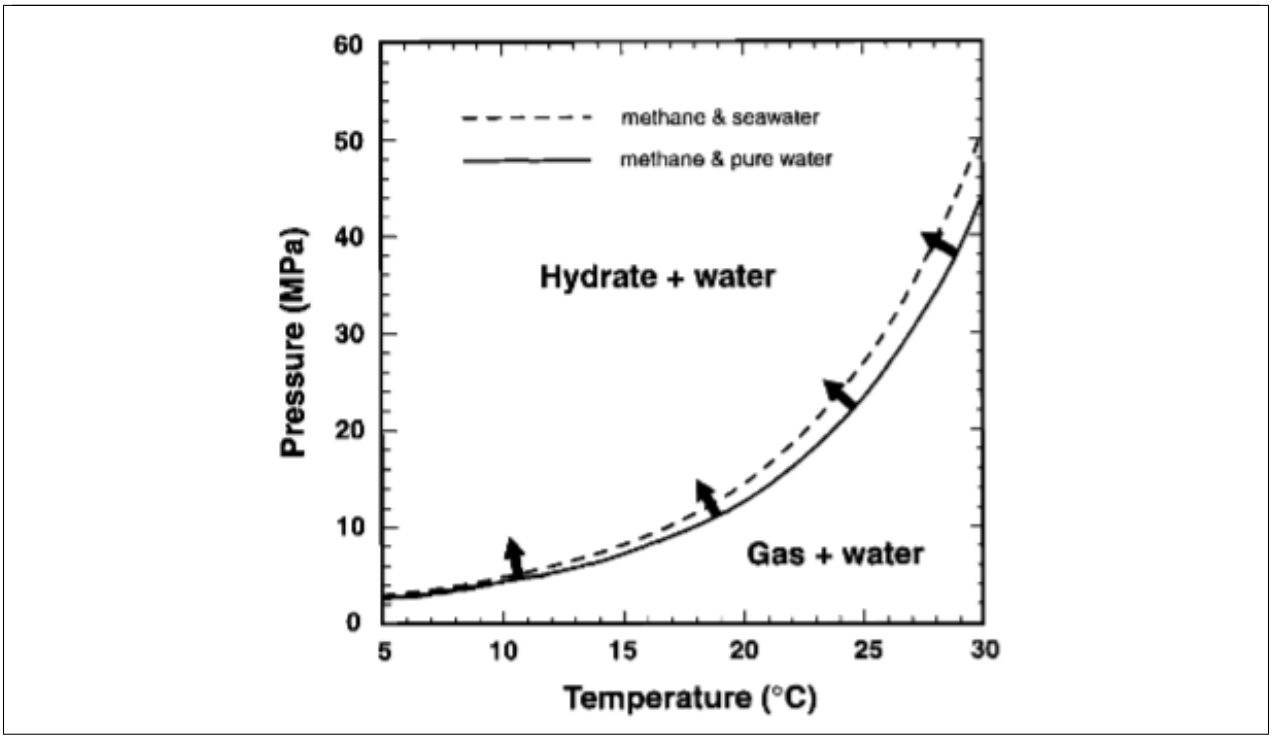

Figure 2.3: Temperature/Pressure phase diagram for pure methane gas and pore water from marine subsurface conditions.The black arrows shows the stability shift from pure to saline water. *Source: (Clennell et al., 1999).*

some time, the gas consumption stabilize and the hydrate becomes stable (Sloan and Koh, 2007).

In the article by Rempel and Buffett (1997), two models for hydrate formation in marine sediments are proposed. The first model assumes a constant influx of gas from thermogenic sources below. Depending on adequate water and gas influx, the hydrate growth will happen rapidly at the base of the hydrate stability zone, but eventually decrease due to thermodynamic and kinetic limitations. The second model relies on gas from biogenic sources located in the hydrate-bearing layer, with no gas influx from below. If the biogenic gas is evenly distributed, hydrates start to grow. If the water and gas influx is sufficient and nucleation heat is transported away, the hydrate reservoir grows in thickness. At one point the increased sedimentation causes the hydrates at the base of the hydrate stability zone to dissociate. The gas from the dissociated hydrates will join formation of new hydrates, causing a formation/dissociation cycle (Buffett and Zatsepina, 2000).

Because gas hydrate stability is temperature and pressure dependent, changes in these conditions might make the hydrates unstable, thus dissociate (Maslin et al., 2010). The Storegga slide outside the Norwegian coast, on the southern Vøring plateau, have been suggested as a dissociated gas hydrate system due to ocean warming (Mienert et al., 2005), (Bouriak et al., 2000). The evidence of a gas hydrate system in the slide area is well reported in literature. However, many authors have proposed other and maybe better solutions for the slide event. Bugge et al. (1987) and Bryn et al. (2005) proposed that the slide was triggered by an earthquake originated from the underlying fault blocks. The earthquake destabilized the sediments, causing the slide event to occur.

Ocean warming will destabilize the gas hydrate system, by moving the base of the gas hydrate stability zone. Dickens et al. (1995) suggested that a temperature increase of 4-8 $^{\circ}C$ over a period of 10^4 years in the Late Paleocene Thermal Maximum (LPTM) (55 Myr), was due to dissociation of a marine methane hydrate system. It has been verified by looking at deep ocean drilling samples, and its negative carbon isotopes. Temperature and pressure variations will have a direct effect on the stability of gas hydrates, and hydrate dissociation process. Dissociation of gas hydrates at sea floor, creates slumps and slides of sediments. This kind of sediment movement is directly related to the safety on off-shore structures, such as platforms, sub-sea structures and pipelines (Sloan, 2003).

2.4 Fluid migration

Gas and water are needed to form gas hydrates, and the gas hydrate reservoir needs a constant fluid influx in order to initiate formation. If one of the fluid constituents are removed, the hydrate formation stops. Free gas originates either from biogenic sources in the respective gas hydrate layer, or as a fluid flow of thermogenic gas from below. In most cases gas hydrate formation is limited by the excess of gas flow into the hydrate formation zone (Rempel and Buffett, 1997). Once the hydrate has formed, the gas and water constituents will struggle to penetrate trough the massive hydrate formation, and gas may be trapped (Bunz et al., 2003). Presence of free gas beneath gas hydrate bearing

sediments have in recent years been proposed to be the main reason for the observed BSR (Andreassen et al., 2003; Bünz et al., 2005). For low gas hydrate saturated sediments, hydrates may only act as a trap for the migrating gas, displaying a weak discontinuous BSR. The presence of free gas is an important part of the gas hydrate system, and is believed to be essential for detection of gas hydrates (Haacke et al., 2007).

Outside the mid-Norwegian margin, several indicators for fluid movement have been observed at the sea floor. Pockmarks, gas chimneys, and gas pipes are present on seismic data, and sometimes on the sea floor. Vertical fluid flow can be distinguished by an upward bending of the seismic reflection, and is often associated with gas chimneys, pockmarks and/or mounds at the sea-floor. Gas chimneys are observed as vertical narrow zones with acoustic wipe-out of upward bending reflections on seismic data (Hustoft et al., 2007). Figure 2.4 shows a conceptual model from the southern Vøring plateau gas hydrate system, at the mid-Norwegian margin. Hustoft et al. (2007) derived the model in Figure 2.4 from high resolution 3D seismic from the same area where the 2D seismic (NH9651-202) data was obtained. The gas originates from the polygonal fault system, and moves up through the Kai and Naust unit W formations. Naust W is an over-pressured unit, where the pore fluid pressure exceeds the principal stress and creates fractures. The gas is expanding, maintaining a high pore-fluid pressure as the fractures propagates vertically. Further, the gas reaches sediments with higher permeability and porosity (indicated by yellow layers), and some of the gas is trapped beneath the gas hydrate zone. Push-downs of the seismic reflector in gas chimneys commonly refers to low P-wave velocity zones, which indicate free gas saturated sediments (Hustoft et al., 2007). Although several authors Mienert et al. (1998); Bunz et al. (2003), agree with Hustoft et al. (2007) that the vertical up-bending of seismic reflections are related to gas and water pipes, it is still debated whether the up-bending is related to pseudo-velocity structures. Pseudo-velocity structures are defined by vertical zones of gas hydrate cementation, or precipitation of authigenic carbonates. Subsequently the acoustic pipes may correspond to mud-diapirs (Hustoft et al., 2007).

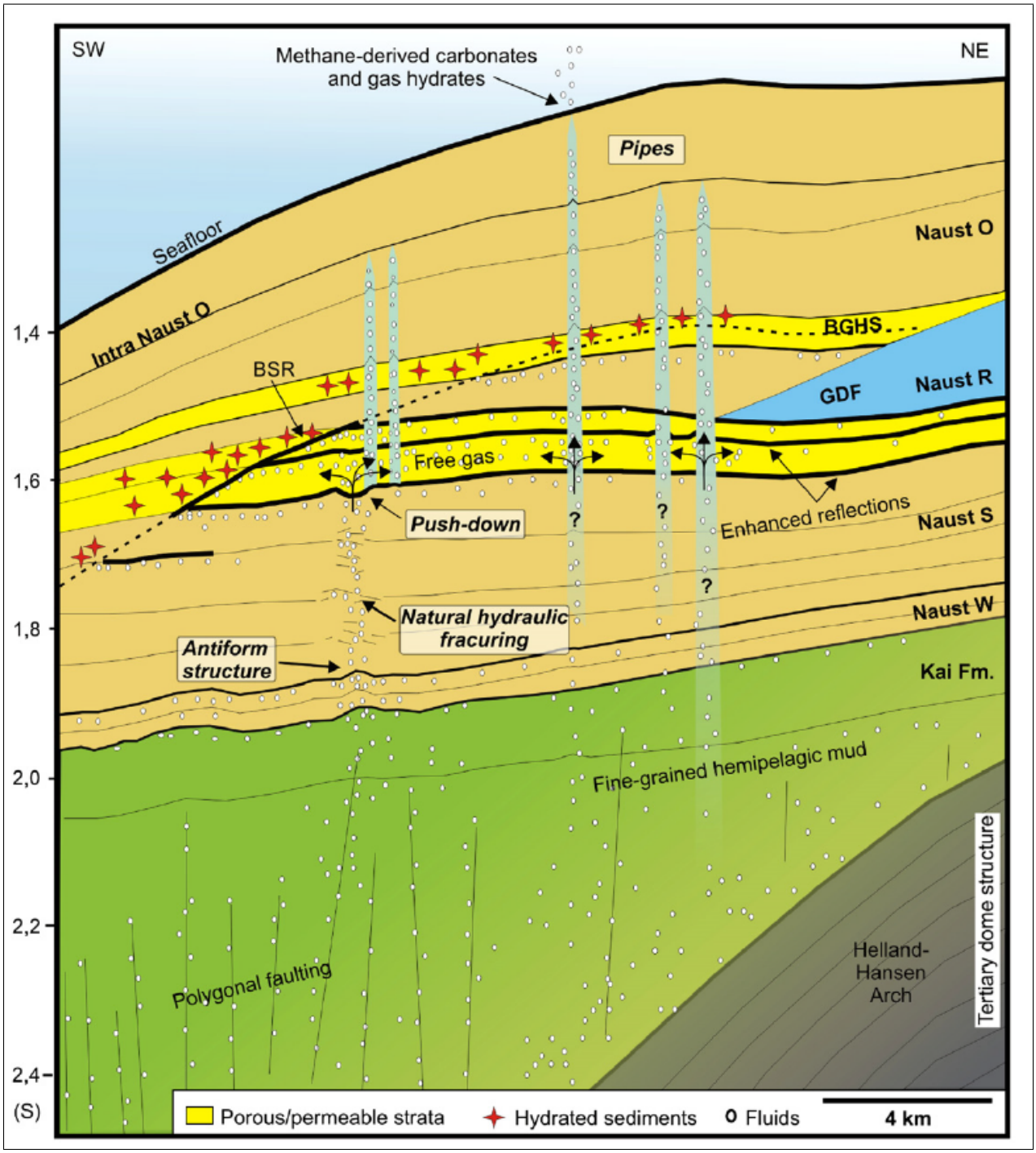

Figure 2.4: Proposed model by Hustoft et al. (2007) of the fluid flow system of the survey area.

2.5 Hydrate in pore voids

The host sediment properties can have a great impact on gas hydrate distribution and saturation in pore voids (Clennell et al., 1999). Permafrost sediments saturated with gas hydrates are often associated with high concentrations of quartz sands and silts. An offshore gas hydrate system at the Cascadia margin have a reportedly high local gas hydrate concentration at an area with high quartz sand concentrations (Riedel et al., 2014). Permafrost areas have a greater depth of overburden sediments, and better consolidated sands, while offshore sediments often are unconsolidated and poorly sorted (Chand et al., 2004). This means that offshore areas with high quartz sand, and low clay content might have a higher potential for gas hydrate cementing grains at high saturations.

Winters et al. (2004), considered three models for the gas hydrate distribution in the Mallik 2L-38 well. Gas hydrates as 1) inclusions with no grain contact, 2) part of the solid frame, or 3) acting as a cement at grain contacts. Ecker et al. (1998), advocated that the gas hydrate system at the Blake Ridge, was most likely inclusions without any grain contact. They compared synthetic data with real seismic data, and the conclusion was that model 1) gave the best fit. Jakobsen et al. (2000) modeled the same case using SCA and DEM theory. The results were similar to those of Ecker et al. (1998), in the sense that the hydrate distribution was found to be unconnected in the pore space (model 1), with a saturation of about 9%. Clennell et al. (1999) have through many experimental data found that hydrates act as segregated bodies in the form of nodules, lenses, pellets and sheets in fine-grained sediments. For coarser sediments, the hydrates often acted as a cement between grains. Model 1) can be used when the fraction of hydrate in the pore space is low (<20-30%) (Jakobsen et al., 2000).

Figure 2.5 illustrates a sketch of different gas hydrate distributions in the pore voids. Model B) in Figure 2.5, shows the gas hydrate as an inclusion with no grain contact, which means that the hydrate have no effect on the grain stiffness. Gas hydrates have both compressional and shear stiffness compared to viscous fluids. Model B) predicts that the gas hydrate will have no effect on the sediment shear stiffness, and only a small effect on the compressional stiffness (Ecker et al., 1998). However, this assumption is only true

for small gas hydrate concentrations when the gas hydrate forms (Sain et al., 2010). Model C) in Figure 2.5 shows that the gas hydrate is a part of the solid grain framework. This model will take the shear and compressional stiffness of the gas hydrates into account. For this model, the porosity will decrease with increasing gas hydrate saturation (Winters et al., 2004).

Another model where the porosity decrease with hydrate saturation, is the cement model D) in Figure 2.5 proposed by Dvorkin et al. (1991). Hydrates act as a cement, either at grain contact (D,1), or as cement coating the grains (D,2). The cement model will increase the stiffness of the sediments greatly for even small hydrate concentrations (Dvorkin et al., 1999). Preliminary results by Tohidi et al. (2001) have shown that the gas hydrate saturations have to be high, for the theory to apply to in-situ conditions. Although results observed in laboratory experiments may not have been completely accurate for real conditions, the principle apply to observed hydrate cementing systems. Tohidi et al.

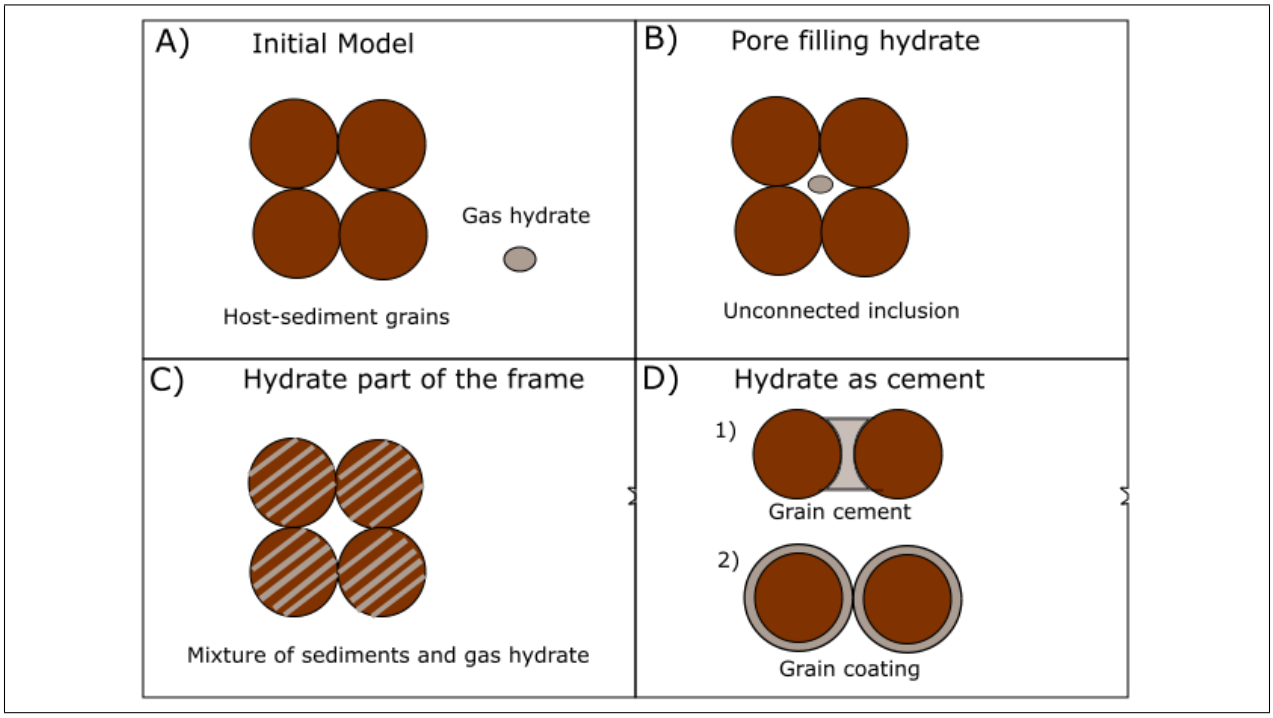

Figure 2.5: 3 hydrate distribution models as outlined by Winters et al. (2004). A) illustrates the simplified model with grains, and gas hydrate inclusion. B) shows hydrate as a pore filling fluid with no connection to the grains. C) shows the case when hydrate act as a solid mixed with other grains as a part of the frame. The last case D) shows hydrate as 1) a cement at the grain contact points, and 2) hydrate as a coating, enveloping the grains.

(2001) performed laboratory tests on hydrate formation, and concluded that the existence of a water film on the grains would force the hydrate formation to occur in the center of the pores. For water-wet sediments, the water would have a permeability around the gas hydrate inclusions, except when the majority of the pore space was saturated with gas hydrates. In the latter case, gas hydrates would have a cementing effect on the grains.

2.6 Elastic properties

In elasticity theory, the relation between stress and strain is formulated through Hook's law. For small deformations, stress is proportional to strain, and Hook's law is valid (Gelius and Johansen, 2010). For a general anisotropic, linear, elastic material, the strain is proportional to the stress, and Hook's law can be written as:

$$\sigma_{ij} = C_{ijkl}\epsilon_{kl} \tag{2.1}$$

where σ and ϵ are the applied stress and strain in the ij and kl direction respectively. C is the elastic stiffness tensor of the 4th order, and defines the elastic properties of the material (Mavko et al., 2009; Gelius and Johansen, 2010).

In seismic, the applied stress is ground motion waves instead of mechanical loading. The wave energy propagate through materials, causing deformations down into the earth. Deformations are small, and the materials behave elastically following Hook's law, returning to its initial state after the stress is removed (Gelius and Johansen, 2010). Materials like rocks, resist deformation with applied stress. Elastic properties have been assigned to explain the behavior of rocks when subdued to stress and strain. Bulk modulus (K) is defined as the reciprocal of compressibility (incompressibility), and shear modulus (μ) is defined as the ratio of the shear stress to the shear displacement (Mavko et al., 2009). There are two types of particle displacement waves or elastic waves: pressure (P) and shear waves (S). P-wave consists of a compressional wave propagating through all materials (solids and fluids) in a compressional/extensional displacement motion. The S-wave propagates through solids but not fluids, following a shearing motion where the movement occurs perpendicular to the direction of the wave (Gelius and Johansen, 2010).

2.7 Identification of gas hydrates

Gas hydrates have a relatively high P- and S-wave velocity, because the hydrate has a greater resistance to compress and shear, than other fluids (water, gas). Because of the velocity elevation, hydrate-bearing sediments often exhibit an increase in velocities (Lee and Collett, 2001). The velocity alone is often not enough to detect hydrates, because hydrate saturation have to be high in order to see a clear difference between hydrate and non-hydrate saturated sediments. Often there exists free gas beneath the gas hydrate layer, because the hydrate zone reduces the vertical permeability, trapping the free gas (Clennell et al., 1999). Free gas bearing sediments causes the P-wave velocity to decrease significantly, by only introducing small amounts of gas. The difference between a high velocity hydrate zone, and an underlying low velocity gas zone, are used as the gas hydrate identification procedure (Bouriak et al., 2000).

The interface between two different layers is in seismic called a reflector, because it is reflecting some of the incoming energy back towards the surface (Gelius and Johansen, 2010). The reflector or interface between the hydrate and gas-bearing layers is called the Bottom Simulating Reflector (BSR), because it mimics the sea-floor reflector. The BSR simulates the sea-floor because the hydrate stability depends a great deal on the overburden pressure from the sediments more than that of water, and therefore mimics the depth variations of the sea-floor reflector. BSR can be seen for other cases than gas hydrates, for example diagnesis-related BSR due to Opal A/Opal CT transition, or a Paleo-BSR as suggested by Berndt et al. (2004). However, gas hydrate related BSR can be distinguished from the other types by its negative acoustic impedance contrast, which gives the reflector a reversed polarity. In addition the BSR is cross-cutting sedimentary strata, as observed in Figure 2.7, where low dipping layers have been terminated by the BSR (Bünz et al., 2005). BSR is a sub- class of cross-cutting reflectors. What characterizes cross-cutting reflectors is that they usually are related to geological processes occurring after deposition of sediments. The BSR reflector is caused by processes related to sub-bottom depth, which means that it is pressure and temperature dependent (Berndt

et al., 2004). The gas hydrate related BSR can be divided into three groups: continuous, discontinuous, and pluming (Hillman et al., 2017). Continuous BSR is identified as a continuous event cross-cutting sediment layers. A discontinuous BSR is distributed as segments or patches, and usually simulates the sea-floor reflector. Pluming BSR is less common, but is viewed as a continuous reflector not simulating the sea-floor reflector, but rather bowed towards the sea-floor because of locally constrained heat flow, due to a strong vertical flux (Hillman et al., 2017).

The BSR originates from the sharp negative acoustic impedance or velocity contrast between the hydrate and underlying gas layers as observed in Figure 2.6. Higher saturations of gas or gas hydrates will give an even higher velocity contrast. In addition to the BSR, another way of detecting gas hydrates is by using the S-wave velocity contrast. Pure gas hydrates have a relatively high S-wave velocity (1.85-2.00 km/s) [3], compared to the typical low S-wave velocity of marine sediments (0.1-0.6 km/s). If the marine sediments contains gas hydrates, the S-wave velocity will increase, while remaining constant for gas and water-filled sediments. With this relation, a S-wave velocity increase can be a direct indication of gas hydrates (Andreassen et al., 2003).

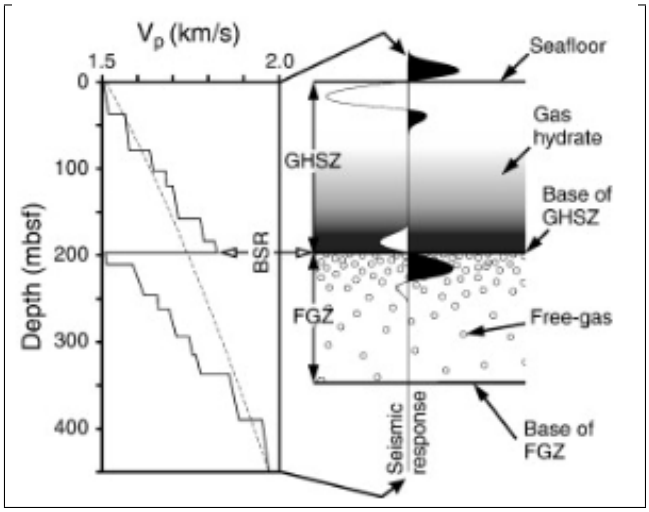

Figure 2.6: Sketch showing how the large velocity contrast between gas and gas hydrate sediments result in a strong negative seismic response. The dotted line shows velocity for sediments without hydrates or gas. Illustration adopted from Haacke et al. (2007).

S-waves do not travel trough water, so shear-waves cannot be detected from a standard marine survey. However, gas hydrate surveys performed by Andreassen et al. (2003); Bünz et al. (2005); Satyavani et al. (2016) have utilized an Ocean Bottom Survey (OBS), where an Ocean Bottom Cable (OBC) with receivers is located on the sea-floor. In this case, the converted S-waves from P-waves will be detected (Gelius and Johansen, 2010).

[3] S-velocity value taken from the book of Sloan and Koh (2007)

All methods for detecting gas hydrates are dependent on gas hydrate saturation in pore voids. Bünz et al. (2005) suggests that the BSR at the Storegga Slide area on the mid-Norwegian, exists mainly because of a free-gas layer. The OBC survey showed no enhancement for the S-wave velocity where the BSR were observed. This suggests that the hydrate saturation was too low to show a sharp increase in acoustic impedance, but sufficient to trap the gas in sediment layers.

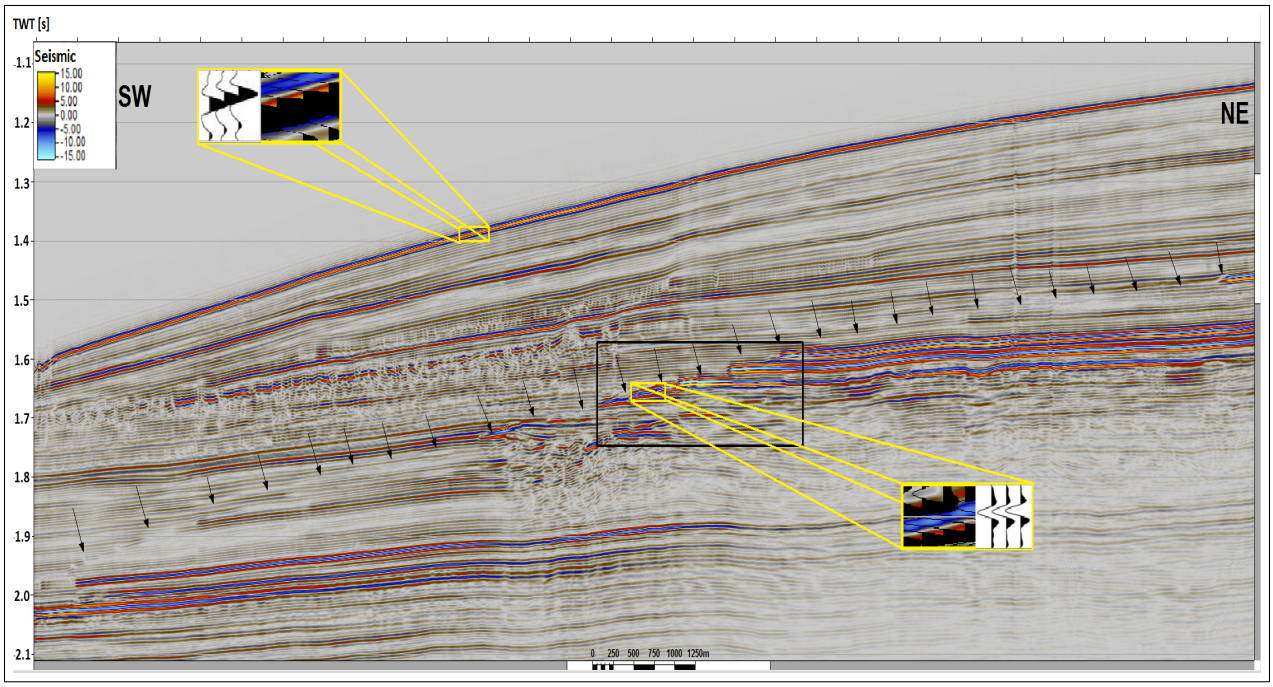

Figure 2.7: Seismic section NH9651-202 taken from the DISKOS database. Showing the BSR distribution on the southern Vøring plateau, north-east from the Storegga Slide area. The BSR are indicated by arrows. A small section are showing the wiggle trace for the sea-floor and the BSR. The BSR has a negative reflector (blue color, trough), while the sea-floor has a positive reflector (red color, peak).

Chapter 3

Modelling Techniques

This chapter will outline the two modelling procedures utilized in this study. Basic theory behind both rock physics and seismic modelling procedures is outlined.
In addition, geological setting from the southern Vøring plateau will be included in the first section. This is due to the fact that mineral constituents and other relevant information from this area is used in the rock physics, and subsequently in the seismic modelling throughout this study. The seismic modelling section will introduce some brief seismic theory, before explaining the 2D convolution simulator and its principles.

3.1 Geological model

In seismic modelling a geological model is created in order to simulate a real stratigraphic model of the earth's subsurface. This study will make use of a geological model similar to the gas hydrate reservoir at the Storegga slide gas hydrate system. Real seismic data have been retrieved from this area, through the DISKOS database. Because of this, the geological model in this study is created based on information regarding the survey area. The survey area is observed in Figure 3.1, where the seismic 2D multichannel-line NH9651-202 is marked. In Figure 3.2 the seismic line is displayed, showing the area where the BSR study of this work is focused on (black square). Each layer in the geological model needs to be assigned properties of P-, S-wave velocity, and density, because these

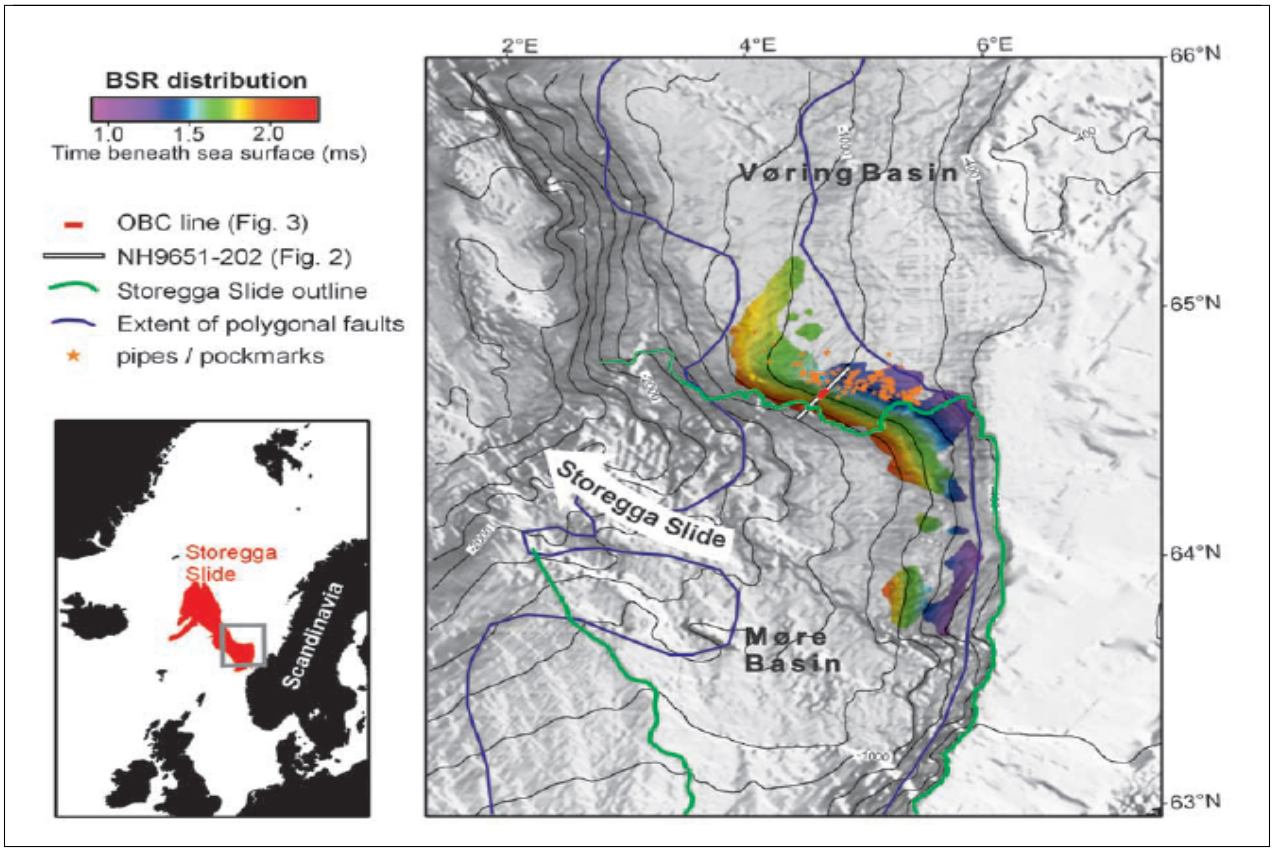

Figure 3.1: The survey area located between the Vøring and Møre basins at the mid-Norwegian margin. The seismic line NH9651-202 is located at the northern headwall of the Storegga Slide area going North-East to South-West. BSR distribution showing that the BSR is dipping with the sea-floor. Figure adopted from Bünz and Mienert (2004).

values are used in the reflectivity calculations for each horizon. The properties for the gas hydrate and free gas bearing sediments are calculated, while the other layers are assigned properties from Bünz and Mienert (2004) and Andreassen et al. (2003). Bünz and Mienert (2004) proposed an equation for calculating P-wave velocity (V_p) from S-wave velocity (V_s),

$$V_p = 0.988 * V_s + 1354 \tag{3.1}$$

The empirical Equation 3.1 is only valid for the regional deposition sediments, and gives velocity values for the sediment layers without gas hydrates or gas, in order to see the effect of gas hydrates and free gas (Bünz et al., 2005). Andreassen et al. (2003) have performed seismic modelling on the same area, using slightly different velocity and density values than Bünz et al. (2005).

3.1.1 Geological setting

In the rock physics modelling performed in this study, information about geology have been gathered from the gas hydrate system on the northern slope of the Storegga slide. In all models created, values retrieved from this area have been used. In order to create the best possible seismic image, the geological setting of the survey area have to be properly understood. The gas hydrate system is located between the Vøring and Møre plateau, at a North-Eastern direction from the Storegga Slide (Figure 3.1). The Storegga Slide event is known to be one of the largest exposed submarine slides, and generated a tsunami that hit the West coast of Norway, Scotland, Shetland and the Faroes. The slide event happened with one main event 8200 years ago, and removed between 2500-3000 km^3 of sediments from the slide area (Bryn et al., 2005). Bugge et al. (1987), proposed that the slide event happened in three stages, but recent studies showed that the slide happened in one main event. The triggering mechanism of the slide have been a widely discussed topic. Bryn et al. (2005) advocates that the most plausible explanation is that the slide started due to an earthquake. The already existing gas hydrate system dissociated, and probably contributed to the slide by removing the strength of the sediments. In Figure 3.2, the northern sidewall of the Storegga slide, can be observed at the South-West boundary of the seismic section. In Figure 3.2, the BSR of the area is indicated by black arrows. The BSR is cross-cutting the stratigraphic layers, and simulating the sea-floor reflector. Gas pipes, or gas chimneys, are indicated by continuous vertical amplitude blanking (Figure 3.2), while some of the pipes reach the sea-floor, resulting in pockmarks at the sea-bottom (Hustoft et al., 2007).

The tectonic and stratigraphic evolution of the Vøring and Møre basin, started with late Jurassic/early Cretaceous rifting that continued until the late Paleocene/early Eocene continental break up. Several compressional periods between late Eocene and mid Miocene times of the mid-Norwegian margin, resulted in North-South oriented dome structures. These dome structures, or anticlines have been important structural-stratigraphic traps for oil and gas in the area, e.g the Ormen Lange gas reservoir. Leakage of gas from these anticlines, are believed to provide the Storegga gas hydrate system with gas (Bunz et al., 2003).

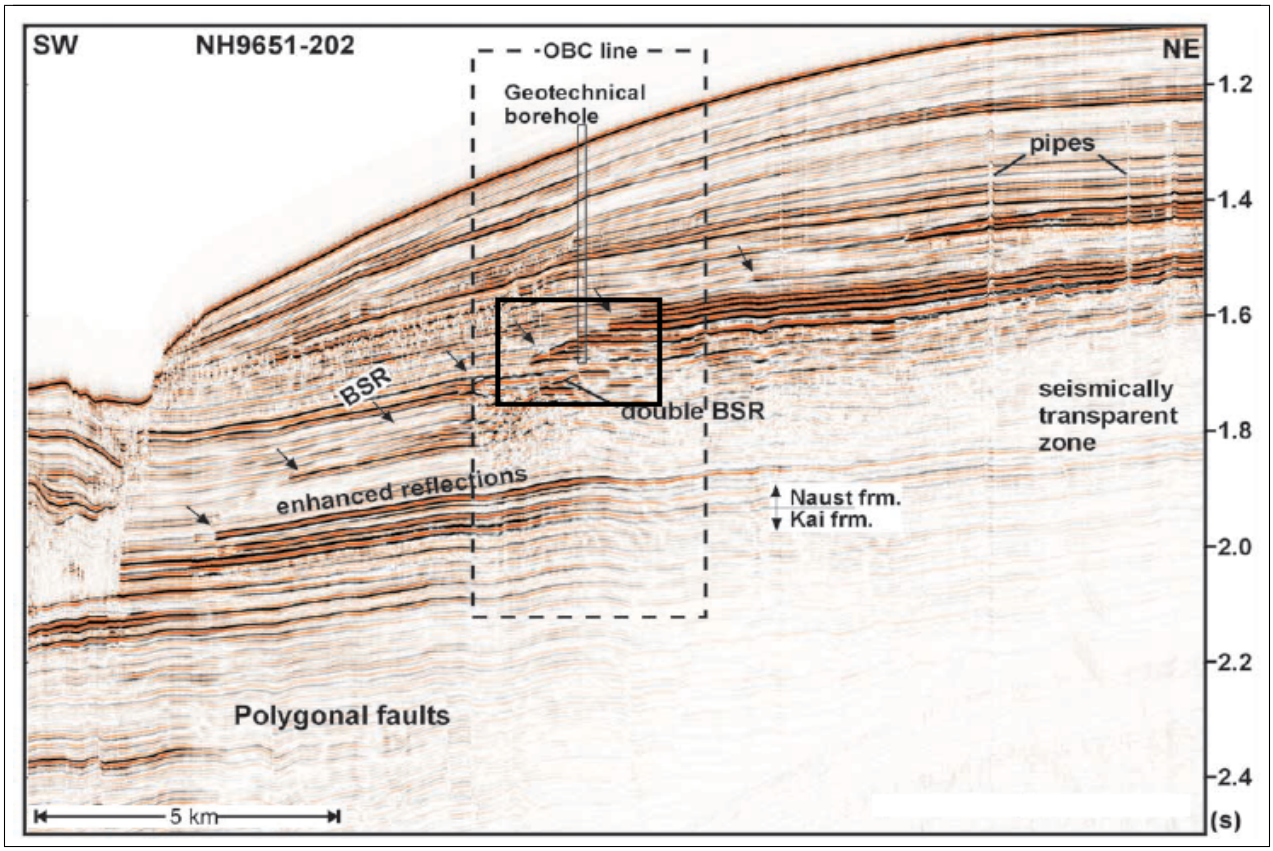

Figure 3.2: Section of the seismic line NH9651-202, observed in Figure 3.1. The Ocean Bottom Cable line (OBC) is located at the sea-floor, and a Geotechnical borehole are drilled 310m down. Black square showing the geologic model target for the seismic modelling. Figure adopted from Bünz and Mienert (2004).

Two large dome structures, Helland-Hansen (HHA) and the Modgunn arch (MA), from the Cenozoic time have influence the deposition in the Vøring basin. A compression phase during the late Brygge deposition, formed the HHA and MA, creating a mid-Miocene unconformity cutting the Kai sediments (Figure 3.3, c). After the last episode of rifting (55 Ma), resulting in continental break up, extensive magmatic activity followed the Vøring basin. The geologic development of the basin started with transgression of the sea due to subsidence of the margin. This resulted in shallow marine conditions, and exposure of large areas. The Brygge formation (a) and b) in Figure 3.3) was deposited from early Eocene to early Miocene (55-18 Ma), and are dominated by siliceous oozes in the Vøring and Møre basins (Chand et al., 2011)). Siliceous oozes are mainly dominated by silicates (Bridge and Demicco, 2008).

On top of the mid-Miocene unconformity, fine-grained sediments was deposited in the Kai formation (14-4 Ma). The Kai formation on-laps the structural high, consisting of fine-grained hemipelagic oozes and clays (Bunz et al., 2003; Chand et al., 2011). The Kai formation is of special importance to the gas hydrate system, because polygonal faults are supposed to control fluid flow on a regional scale, and might be the source of gas. The polygonal fault system in the Kai formation was created due to a sediment contraction, and subsequent fluid expulsion (Bunz et al., 2003). In addition to the Kai formation, the overlying Naust formation, is especially important, because this is where the BSR occur (Figure 3.3, d)). The Naust sediments was deposited about 2.8 Ma, and are characterized by large changes in lithology. The sediments was deposited in the Plio/Pleistocene, and are associated with the glacial/inter-glacial cycles with debris flow deposits, and hemipelagic sediments.

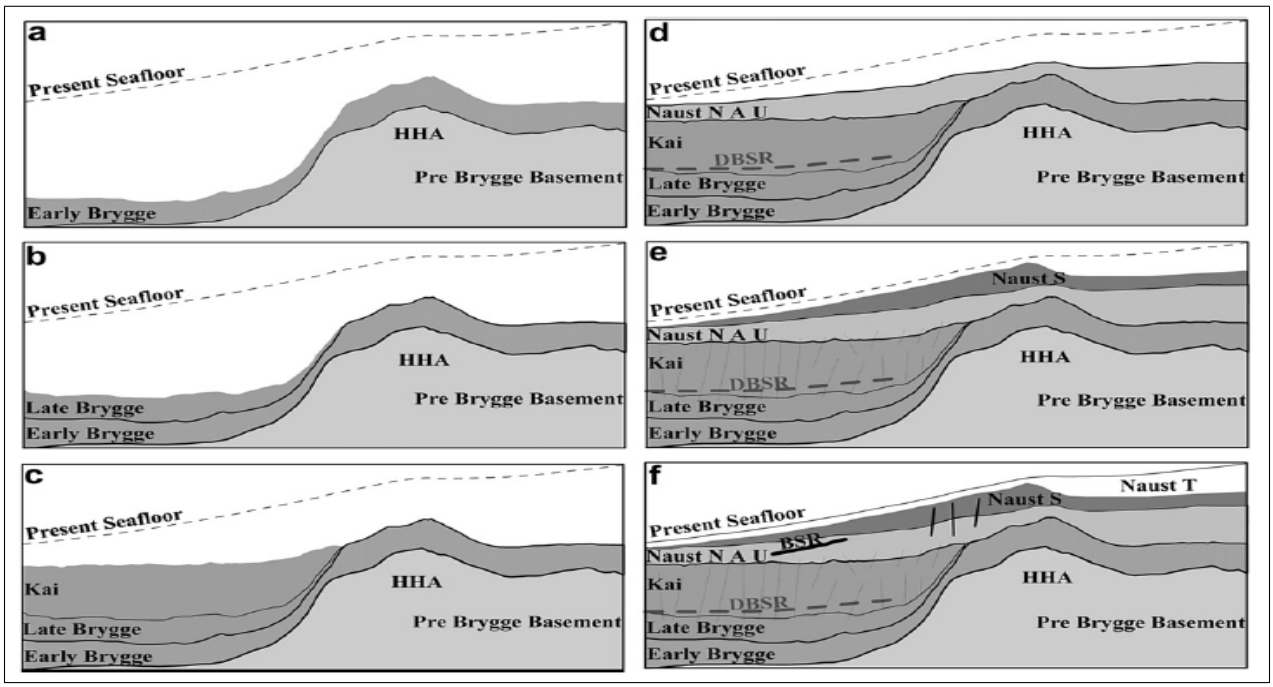

Figure 3.3: Sketch adopted from Chand et al. (2011), showing the deposition history of the Vøring basin. a), b), c), d), e), and f) display deposition and the effect on fluid flow. HHA is the Helland-Hansen arch, and DBSR is the diagnetic BSR.

A geotechnical borehole (Figure 3.4) was drilled by Norsk Hydro, in the same area where the multichannel seismic 2D line NH9651-202 (Figure 3.2) was acquired. The geotechnical borehole penetrated 310 m down, and into the gas hydrate reservoir. Soil samples was

gathered, but no gas hydrate was found in the cores due to technical limitations. The soil samples revealed five different minerals: mica, clay, quartz, feldspar and calcite. The mineral constituents are used in the rock physics modelling for the gas hydrate and free gas layer (Bünz and Mienert, 2004). Table 3.1 shows the elastic properties for the mineral constituents and their volumetric fraction in the sediments.

Table 3.1: values obtained in Bünz and Mienert (2004), for bulk modulus (K), shear modulus (μ), density (ρ), and fraction of mineral constituents for the free gas layer(V_{Gas}), and hydrate layer ($V_{hydrate}$).

Constituents	V_{Gas} [%]	$V_{hydrate}$ [%]	K [GPa]	μ [GPa]	ρ [g/cm^3]
Quartz	10	10	37	45	2.65
Clay	20	25	20.9	6.85	2.58
Mica	35	35	61	41	2.80
Calcite	15	15	77	32	2.71
Feldspar	20	15	34.5	15	2.62

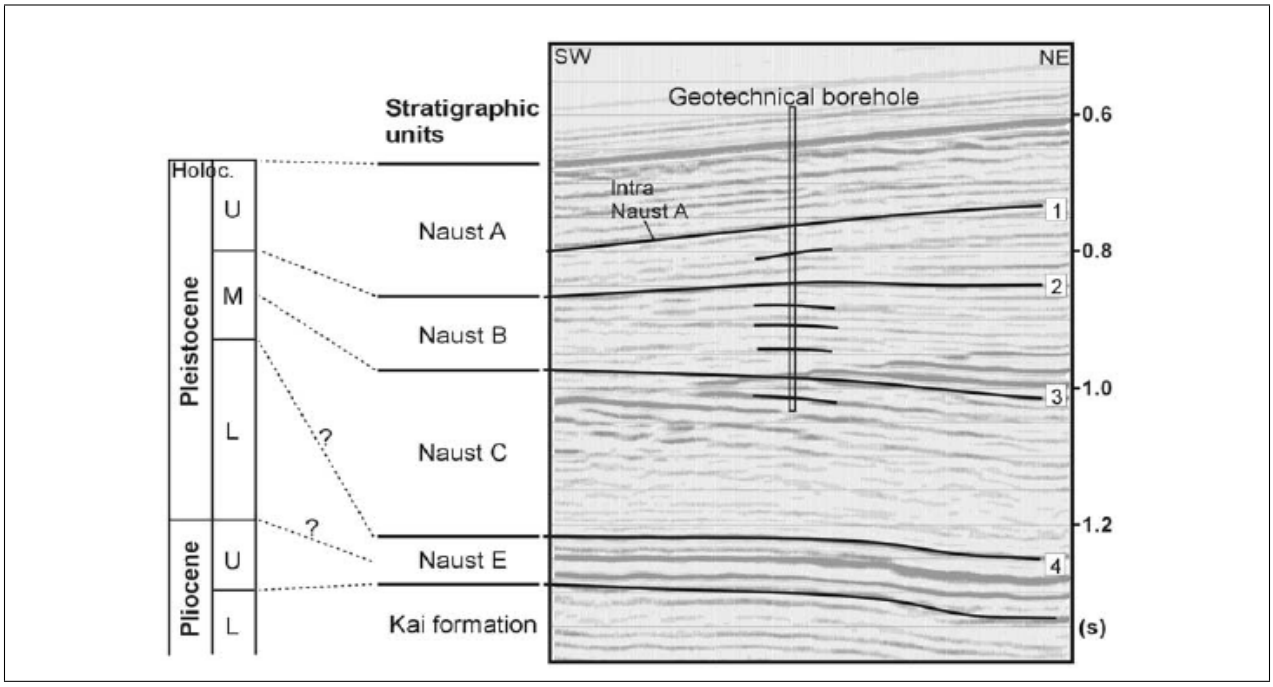

Figure 3.4: Showing the Geotechnical borehole area indicated in figure 3.2. The time axis do not correspond to the time axis used earlier, because of time-stretching. Showing different layers (reflectors) within the Naust formation, corresponding to geologic time scale. U, M, L means Upper, Mid, and Lower. Picture adopted from Bünz and Mienert (2004).

3.2 Rock physics

Subsurface reservoirs are complex systems consisting of several constituents (fluids, pores, grains), that are subjected to mechanical and chemical compaction. To understand and explain these complex reservoirs, simplified rock physics methods have been compared to real seismic data, giving reasonable results. Rock physics models give information about the physical behavior of rocks through acoustic, electric, dielectric, thermal, magnetic, and mechanical methods (Guéguen and Palciauskas, 1994). Acoustic, or better called seismic methods are utilized in this study.

3.2.1 Gas hydrate system

The seismic modelling is based on the gas hydrate reservoir system outside the Norwegian continental shelf. The gas hydrate system considered, have been extensively investigated, and information about geology, porosity, gas hydrate distribution and proposed saturation is obtained from (Andreassen et al., 2003; Bünz and Mienert, 2004; Bünz et al., 2005). Evidence point to a very low gas hydrate saturation at the Storegga gas hydrate system, and gas hydrates cementing grains have been ruled out. However, the previous gas hydrate system at this area might have had a larger hydrate saturation prior to the slide event. In any case, the reservoir will be considered as the geological model in this thesis.

It has been suggested by Andreassen et al. (2003) and Bünz et al. (2005), that the reason why the P-P reflections show an elevated BSR is because of the underlying free gas layer, and not the gas hydrate layer. Andreassen et al. (2003) did a OBC survey over the same area that Mienert et al. (2005) investigated, and collected converted P-S waves. It was believed that the gas hydrates would increase the general shear strength, consequently increasing the S velocity. However, no evidence of an elevated S-velocity in the gas hydrate zone was found. Andreassen et al. (2003) concluded that the gas hydrate concentration at the Storegga slide was too low (around 1.5 %) to show as an anomaly on the converted P-S velocity specter.

The low gas hydrate saturation suggested in the survey area, results in little or no evidence of gas hydrates cementing the grain contacts. A better model for explaining the gas hydrate system, will be to treat the gas hydrates as part of the grains, or as inclusions away from grain contact (Bünz et al., 2005). However, gas hydrates are believed to trap the underlying free gas in some areas, that would suggest cementing to some degree, closing off pore pathways and reducing permeability.

3.2.2 Effective Medium Theory

All rocks are heterogeneous, whether it is a strong or weak heterogeneity. Heterogeneous properties are complex and difficult to determine, so different scales to view the rocks as a homogeneous medium are introduced. Three scales are utilized (micro, mini, and macro) for viewing the medium (Figure 3.5). The micro-scale shows the grains and pore void constituents, the mini-scale shows a larger volume of grains and pore voids, while the macro-scale shows the rock sample that is studied (Figure 3.5). A rock that is heterogeneous at a micro-scale might appear homogeneous on the mini scale, and will for the most cases be homogeneous on the macro-scale. However, when the heterogeneity is very strong, it can be observable on the macro-scale. When this happens, the Effective Medium Theories (EMT) cannot be used, and other more complex theories are utilized (Guéguen and Palciauskas, 1994).

EMT is a term for averaging functions that are trying to get as close to the truth as possible (Choy, 2015). EMT provides an estimation of the true effective physical properties (Gelius and Johansen, 2010). It would be impossible to calculate the exact elastic properties of a rock system, which is why different approaches or effective medium methods are used. Effective rock properties are found by using effective medium models. A rock may contain several mineral constituents. Dependent on the orientation of the composite, if it is soft or stiff mixing, Reuss Equation 3.2 or Voigt Equation 3.3 can be used, respectively for finding K and μ[1].

[1]In most articles explaining rock physics, the shear modulus μ is written as G. In this thesis the shear modulus will however be written as μ

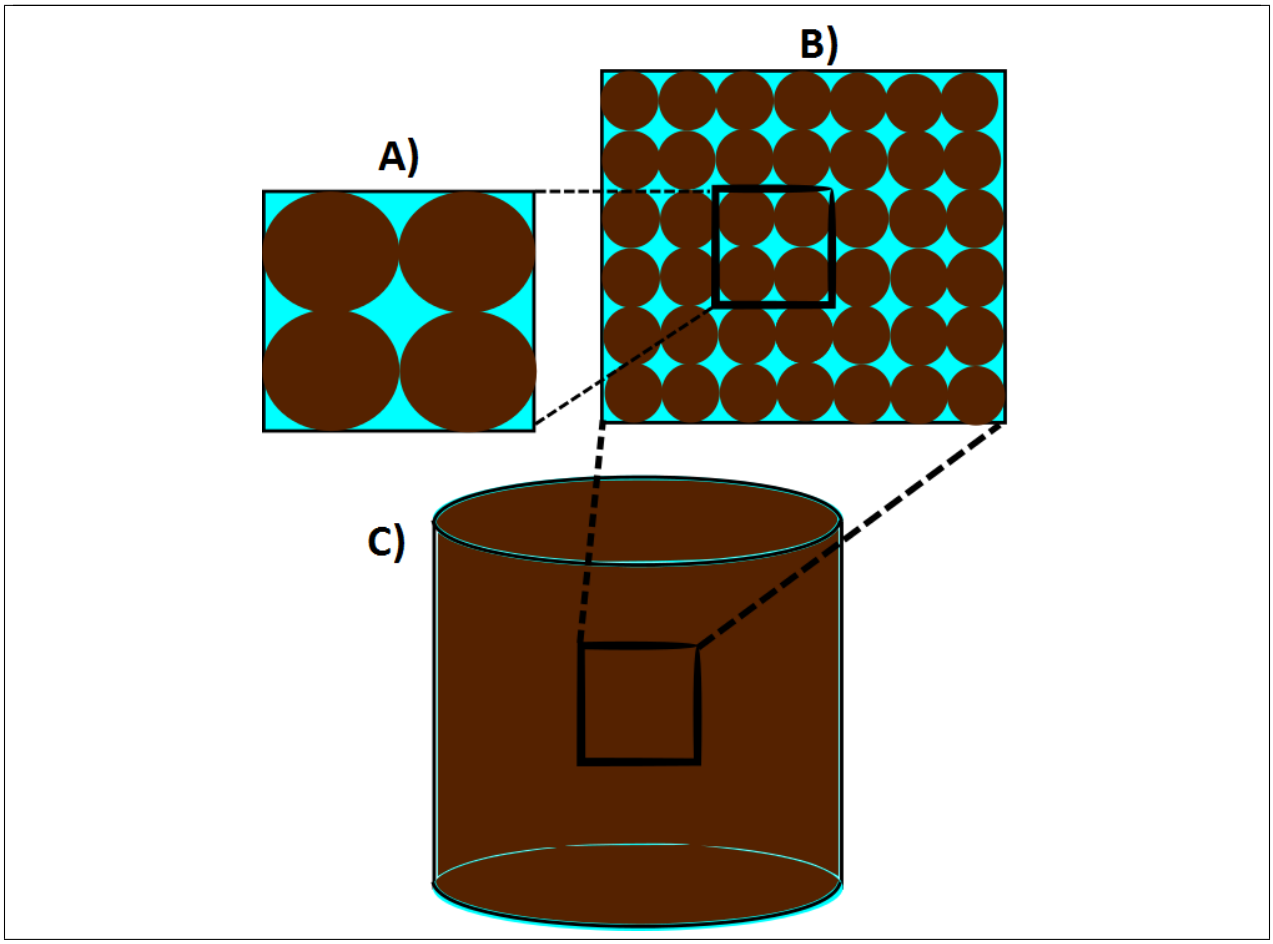

Figure 3.5: 3 scales corresponding to A) micro, B) mini, and C) macro. Easy sketch made in inkscape. Brown color is grains, while light blue is considered pore voids.

$$K^R = (\frac{V_1}{K_1} + \frac{V_2}{K_2})^{-1} \tag{3.2}$$

$$K^V = V_1 K_1 + V_2 K_2 \tag{3.3}$$

$$K^H = \frac{1}{2}(K^R + K^V) \tag{3.4}$$

The bulk modulus is denoted K with subscripts defining Reuss (R), Voigt (V), and Hill (H). The volume fraction of the constituents (1,2) is denoted V. Reuss average is used for soft composite mixing while Voigt average is used for stiff mixing. When different fluids are mixed in the pore voids, Reuss average is used, by applying the saturation of the fluids as the volume fraction. The mean value of Reuss and Voigt is called the Hill average model (Equation 3.4). The mixing of two composites depend on both the stress

direction and the layer direction (soft or stiff). The effective medium density however, do not depend on the mixing conditions. The effective medium density is found by:

$$\rho^* = \sum_{j=1}^{M} V_j \rho_j \tag{3.5}$$

where ρ^* is the effective density, calculated by the sum of the densities (ρ_j) and volume fractions (V_j) of the different constituents j (Gelius and Johansen, 2010). When density, bulk and shear modulus for the effective medium is known, the velocity for P (V_p) and S (V_s) waves can be calculated by using Equations 3.6 and 3.7.

$$V_p = \sqrt{\frac{K + \frac{4}{3}\mu}{\rho}} \tag{3.6}$$

$$V_s = \sqrt{\frac{\mu}{\rho}} \tag{3.7}$$

where K is the effective bulk modulus, μ the effective shear modulus, and ρ the effective density for the sediment. For sediment layers with different properties, the amount of energy reflected back or transmitted at the interface is given by the acoustic impedance Z. Acoustic impedance for a sediment depends on density and velocity contributions,

$$Z = \rho V_p \tag{3.8}$$

where the acoustic impedance (Z) is the product of the P-velocity (V_p) and density (ρ) for the respective layer. The interface between two layers with different acoustic impedance, creates a reflection coefficient (R) outlined in Equation 3.9. Incident waves on the boundary will be reflected with an intensity equal to the reflection coefficient. If the acoustic impedance contrast between the two layers is large, more energy is reflected back, and the interface become visible on seismic. The reflection coefficient varies from 1 to -1. If the acoustic impedance (Z_1) for layer 1 is lower than layer 2 (Z_2) below, the reflection coefficient becomes positive. A negative reflection coefficient can be observed for the reversed case (Mavko et al., 2009). The reflection coefficient (R) is given as:

$$R = \frac{Z_2 - Z_1}{Z_2 + Z_1} \tag{3.9}$$

Equation 3.9 is only valid for horizontally stratigraphic layers with a normal incidence

angle, which is almost never the case in nature. For complex stratigraphic layers, the reflection coefficients are calculated from the complicated Zoeppritz equation, dependent on different incidence angles (Gelius and Johansen, 2010).

3.2.3 Free gas layer

Calculations are also performed for sediments containing free gas in this study. Using Hertz-Mindlin theory together with the Gassmann formula. Dry rock properties are considered the properties of rocks with no pore fluid present. To estimate the dry rock elastic properties, Hertz-mindlin theory (H-M) also known as contact theory is used. When the grains have been stabilized in contact with each other, H-M theory assume that they do not reorganize with further hydrostatic loading (Gelius and Johansen, 2010). Considering a random pack of identical spherical grains, the elastic bulk and shear modulus of the dry frame follows the H-M Equation 3.10,

$$K_{HM} = \Big[\frac{n^2(1-\phi_c)^2\mu^2}{18\pi^2(1-\nu)^2}P\Big]^{1/3} \tag{3.10}$$

$$\mu_{HM} = \frac{5-4\nu}{5(2-\nu)}\Big[\frac{3n^2(1-\phi_c)^2\mu^2}{2\pi^2(1-\nu)^2}P\Big]^{1/3} \tag{3.11}$$

where n is the average number of contact points for each grain, called the coordination number. The confining pressure (P) is given in Equation 3.12, ν is the poisson's ratio (Equation 3.13), g is the gravitational constant, D is depth below seafloor, and ρ is the bulk density of the solids (s) and fluids (f) respectively (Gelius and Johansen, 2010).

$$P = (\rho_s - \rho_f)gD \tag{3.12}$$

$$\nu = \frac{3K-2\mu}{2(3K+\mu)} \tag{3.13}$$

Free gas act to decrease the bulk modulus (compressibility) of the sediments greatly with only small amounts. To model the free gas layer, Hertz-Mindlin theory together with Gassmann's (Equation 3.14) formula are used in the same manner as described by Ecker et al. (1998). Gassmann's formula predicts the influence of a pore fluid on the effective elastic properties of a porous rock. The formula assumes that all pores are connected, all grains have the same elastic properties, and that the pore fluid fully saturates the pore

voids in a homogeneous distribution (Gelius and Johansen, 2010). Gassmann's formula also assume no fluid effect on the shear modulus for the saturated rock, so that the saturated shear modulus is the same as for the dry rock (Equation 3.15).

$$K_{sat} = K_{solid}\frac{\phi K_{dry} - \frac{(1+\phi)K_{fluid}K_{dry}}{K_{Solid}} + K_{fluid}}{(1-\phi)K_{fluid} + \phi K_{solid} - \frac{K_{fluid}K_{dry}}{K_{solid}}} \tag{3.14}$$

$$\mu_{sat} = \mu_{dry} \tag{3.15}$$

The bulk modulus (K) for the saturated rock, fluid, dry rock, and solid is defined as $K_{sat}, K_{fluid}, K_{dry}$, and K_{solid} respectively. The shear modulus (μ) for the saturated rock (μ_{sat}) is equal to that of the dry rock (μ_{dry}). Gas hydrates are as mentioned formed from water and gas. To model the gas/water saturated sediments beneath the gas hydrate saturated sediments, Reuss (Equation 3.2) formula is used to mix the two fluids.

3.2.4 Gas hydrate model

Seismic velocities are high for sediments containing gas hydrates. Even soft cement at the grain contact of the sediments, increases the stiffness (Ecker et al., 1998). Gas hydrates may occur as fluid inclusions in the pore space, grain coating, part of the solid frame or as a cement at grain contacts (Figure 3.6). Ecker et al. (1998) and Helgerud et al. (1999) both considered hydrate as inclusions without any effect on the stiffness of the grains (Figure 3.6, B). Hydrate and water are mixed with Reuss Equation 3.2, and the effective elastic moduli of the saturated rock can be calculated by using Hertz-mindlin (Equation 3.10, 3.11) theory and Gassmann's formula (Equation 3.14). Gassmann's formula do not account for the shear modulus of the gas hydrate inclusions, and this model can therefore never model high gas hydrate saturations (Sain et al., 2010). However, at low hydrate concentrations, gas hydrate inclusions are suspended in surrounding water (Tohidi et al., 2001), and the rock physics model proposed can be used as an approximate solution.

For modelling gas hydrates as load-bearing cement at grain contacts, the Contact Cement Theory (CCT) of Dvorkin et al. (1991) is used. CCT is used when the cement concentration is small (10-15%). The cement can exist in two ways at the grain contacts. 1) cement

coating enveloping the grains (Figure 3.6), or 2) cement only at the grain contact points (Figure 3.6). The bulk (K) and shear modulus (μ) of the hydrate cemented dry rock is calculated using Equations 3.16 and 3.17,

$$K_{CCT} = \frac{n(1-\phi_0)}{6} M_H S_n \tag{3.16}$$

$$\mu_{CCT} = \frac{1}{5} K_{CCT} + \frac{3n(1-\phi_0)}{20} \mu_H S_\tau \tag{3.17}$$

where ϕ_0 is the initial porosity without any cement present. Values of ϕ_0 and coordination number n, are typically around 40% porosity and 9 grain contact points, for a sandstone (Mavko et al., 2009; Dvorkin and Nur, 1996). Reduced porosity will make the grain-pack denser, consequently resulting in an increase in grain contact points (Johansen et al., 2003). S_n and S_τ are parameters that depend on the elastic moduli of the grains, hydrate, and fraction of void space cemented with hydrate. The procedure for calculating S_n and S_τ is given in Appendix B. M_H and μ_H is the compressional and shear modulus of hydrate respectively and is given as,

$$M_H = K_H + \frac{4}{3}\mu_H \tag{3.18}$$

K_H and μ_H is the bulk and shear modulus of pure gas hydrate.

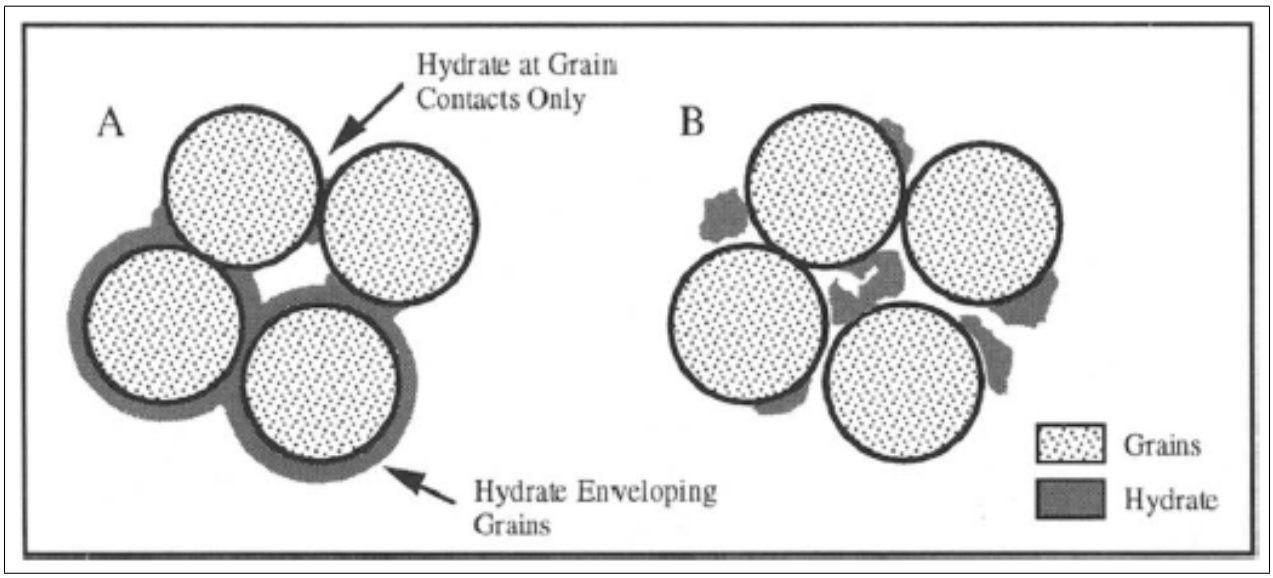

Figure 3.6: Two ways of hydrates to occur in the pore space. A) Cement contact model and B) no-contact model (patchy saturation). *Source: (Ecker et al., 1998)*

For larger hydrate saturations (>15%), an EMT technique called the Self Consistent Approach (SCA) is used to model the hydrate as pore-filling material. The SCA method can model high concentration of inclusions, by assuming that the background host matrix is equal to the effective medium. The background matrix is free to change until no scattering of waves occur, thus achieving a homogeneous matrix (Mavko et al., 2009). The method is self-consistent, meaning that the interactions between inclusions is approximated by letting the background matrix be equal to the not-yet-known effective medium. The SCA method also depend on the critical porosity, as supposed to Differential Effective Medium (DEM) theory (Gelius and Johansen, 2010). This means that the shear stiffness is zero above the critical porosity, allowing for mixing of water and gas hydrate at a critical saturation.

The SC approach together with CCT have been proposed by Dvorkin et al. (1999), and Johansen et al. (2003) to follow the illustrated method in Figure 3.7. Johansen et al. (2003) modeled frozen and partially frozen water in sediments using the CCT/SCA method of Dvorkin et al. (1999). Assuming that 15% gas hydrate is cementing the grains, and consequently reducing the porosity, the system is moved from point A to point B in Figure 3.7 by the use of contact cement theory.

The next step is to move from point B to point C in Figure 3.7, which is when all of the pore voids have been filled with gas hydrates. The existing three phase system containing voids, grains and hydrate cement, are treated as a two phase system with voids in a homogeneous medium. For spherical inclusions, the self-consistent method (SCA) can be used to calculate the bulk and shear modulus of the two-phase homogeneous material. By assuming that the elastic moduli calculated by CCT for a small gas hydrate fraction ($S_{ch} = 0.15$), is a two-phase system of dry rock (grains and cemented hydrate) and dry pore voids:

$$K_{EMT}(\phi) = K_{CCT}(S_{ch}), \quad \mu_{EMT}(\phi) = \mu_{CCT}(S_{ch}) \tag{3.19}$$

The bulk and shear modulus calculated using CCT with a small amount of gas hydrate saturation (S_{ch}), are set equal to the bulk and shear modulus of the SCA (EMT) method, as stated in Equation 3.19. The porosity consists of dry voids in the cemented grain pack,

where the porosity is reduced due to the fact that cementing hydrate occupy the pore voids as grain material ($\phi = \phi_0(1 - S_{ch})$).

The effective elastic medium with a yet unknown host medium (K_s) is given as a three phased equation with the host material, gas hydrate inclusions and dry voids,

$$(1-\phi)[K_s - K_{EMT}(\phi_h, \phi_d)]P_s + (1-\phi)[K_h - K_{EMT}(\phi_h, \phi_d)]P_h - \phi K_{EMT}(\phi_h, \phi_d)P_0 = 0 \tag{3.20}$$

$$(1-\phi)[\mu_s - \mu_{EMT}(\phi_h, \phi_d)]Q_s + (1-\phi)[\mu_h - \mu_{EMT}(\phi_h, \phi_d)]Q_h - \phi \mu_{EMT}(\phi_h, \phi_d)Q_0 = 0 \tag{3.21}$$

In Equations 3.20 and 3.21, P and Q are equations given in Dvorkin et al. (1999) for the given medium (s = host, h = hydrate, 0 = dry voids). Definitions of P and Q are given in Appendix B. In order to solve the equation for the effective moduli, an iteration procedure have to be used. The self consistent approximation uses the yet unknown elastic properties of the effective medium as the background matrix. For the initial case, there are no gas hydrates, only dry voids. Following the assumptions in Equation 3.19, the hydrate part of Equations 3.20 and 3.21 vanishes, and the expression can be written as,

$$\frac{1}{K_{CCT} + \frac{4}{3}\mu_{CCT}} = \frac{1-\phi}{K_s + \frac{4}{3}\mu_{CCT}} + \frac{\phi}{\frac{4}{3}\mu_{CCT}} \tag{3.22}$$

$$\frac{1}{\mu_{CCT} + Z} = \frac{1-\phi}{\mu_s + Z} + \frac{\phi}{\mu_{CCT}} \tag{3.23}$$

$$Z = \frac{\mu_{CCT}(9K_{CCT} + 8\mu_{CCT})}{6(K_{CCT} + 2\mu_{CCT})} \tag{3.24}$$

Solving these equations for the bulk and shear modulus of the host material (K_s, μ_s), explicit solutions can be obtained (Dvorkin et al., 1999).

Further, the self consistent approximation is used by gradually increasing the hydrate saturation until all of the pore voids are filled with gas hydrates (Figure 3.7, B-C). Gas hydrate saturations above the cementing hydrate saturation are believed to be pore-filling, hence the hydrate will not act as a part of the frame (Dvorkin et al., 1999). When the 100% hydrate saturated rock reach point C in Figure 3.7, dry voids are introduced into the hydrate saturated pore voids to reach point D. When solving Equations 3.20 and 3.21 for the three phased situation, the porosity ($\phi = \phi_h + \phi_d$) becomes a sum of the dry void ($\phi_d = \phi_0(1 - Sh)$) and hydrate ($\phi_d = \phi(Sh - Sch)$) porosity.

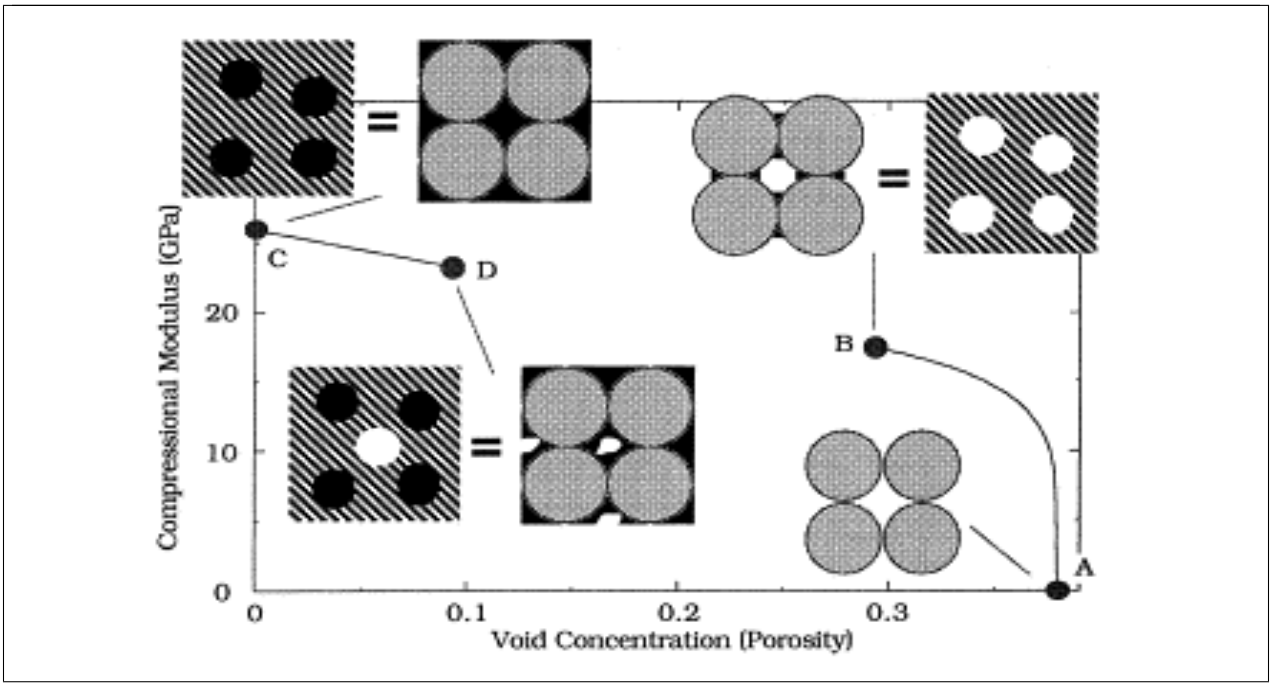

Figure 3.7: Method showing how the elastic moduli of the hydrate cemented sediments was calculated. A) is the uncemented sphere pack, with dry pore voids. B) is the case when a small concentration of hydrates are cementing the grain to grain contact (CCT calculation). C) Showing completely hydrate cemented pore space. D) Pore voids are added to the 100% cemented case. *Illustration adopted from Dvorkin et al. (1999).*

Johansen et al. (2003) studied voids saturated with partially frozen water, by using SCA to calculate the bulk and shear modulus of the water transition to ice (Equations 3.25 and 3.26). This transition can also be used for hydrate and water, because hydrate formation from a water/gas mixture is not completely different from that of water to ice.

$$S_h[K_h - K_p(S_w, S_h)]P_h + S_w[K_w - K_p(S_w, S_h)]P_w = 0 \tag{3.25}$$

$$S_h[\mu_h - \mu_p(S_w, S_h)]P_h + S_w[\mu_w - \mu_p(S_w, S_h)]P_w = 0 \tag{3.26}$$

K_p and μ_p is the elastic properties for the mixture, and S is the saturation of the constituents (hydrate (h) and water (w)).

Because gas hydrates have shear strength, in contrast to water, the transition where the fluid mixture gains shear strength will be the offset for solid hydrate to form. Johansen et al. (2003) introduced the water/ice mixture into sediment pore voids, by exchanging

K_p with K_h in Equations 3.16 and 3.17 for when the mixture behaves as a solid ($\mu_p > 0$). When $\mu_p = 0$ and the mixture behaves as a fluid, the saturated effective medium moduli is calculated by substituting Kp with K_{fluid} in Gassmann's formula (Equation 3.14). When the mixture of gas hydrate and water reach the critical concentration for where the mixture becomes a solid, the cementing of grains will be initiated. The cementing will continue until the fraction of hydrates become significantly large (Sh > Sch). Further, the gas hydrate saturation increases, until all of the pore void is fully saturated. The CCT model predicts that the cementing of grains can occur in two different manners, as 1) cement at grain contact, and 2) cement coating enveloping grains (Dvorkin et al., 1991). These two models will have a great effect on the elastic properties of the effective medium, and will be displayed in the results chapter of this thesis.

3.3 Seismic modelling

The seismic modelling is based on NORSAR-2D, NORSAR-3D, and SeisRoX. Going forward NORSAR-2D, NORSAR-3D, and SeisRoX modelling tools, are referred to as 2D, 3D model-builder and 2D convolution modelling respectively. This section will introduce the theory behind the seismic modelling procedure performed in this study. In order to understand the principle behind the seismic modelling results, some basic theory about seismic acquisition and propagating waves have to be included.

3.3.1 Brief seismic theory

A marine survey is composed of a seismic vessel towing a source (air-gun), and one or several streamers with receivers. The air-gun shoots compressed air with high frequency below the water surface, and P-waves propagate through the water-column into the subsurface of the earth (Gelius and Johansen, 2010). The interface between two layers is called a reflector, because the contrast in acoustic impedance will reflect some of the energy back to the receivers. The shot interval depends on each survey, but a shot distance of about 25-50 m is usual (Ashcroft, 2011). In Figure 3.8, case a) display a

source generating a normal incidence wave (0°angle range), with a 90°reflection. In reality subsurface layers are complex, incoming source waves are angle dependent, and offsets exist. An offset is the distance between a receiver and source, and exists as near, mid and far offset. The reflection angle and travel-times are smaller for near offsets and larger for far offsets. Offsets also plays an important role when talking about AVO (Amplitude Variations vs Offset), which is widely used in oil/gas exploration, and also gas hydrates in some cases.

After the seismic acquisition have been carried out, the reflectivity is convolved with a wavelet, to form a trace (one vertical line in Figure 3.8). The traces are then processed in order to obtain the seismic image in Figure 3.8 b). In other words, the goal of the seismic interpreter is to make a model as close to reality as possible (Ashcroft, 2011).

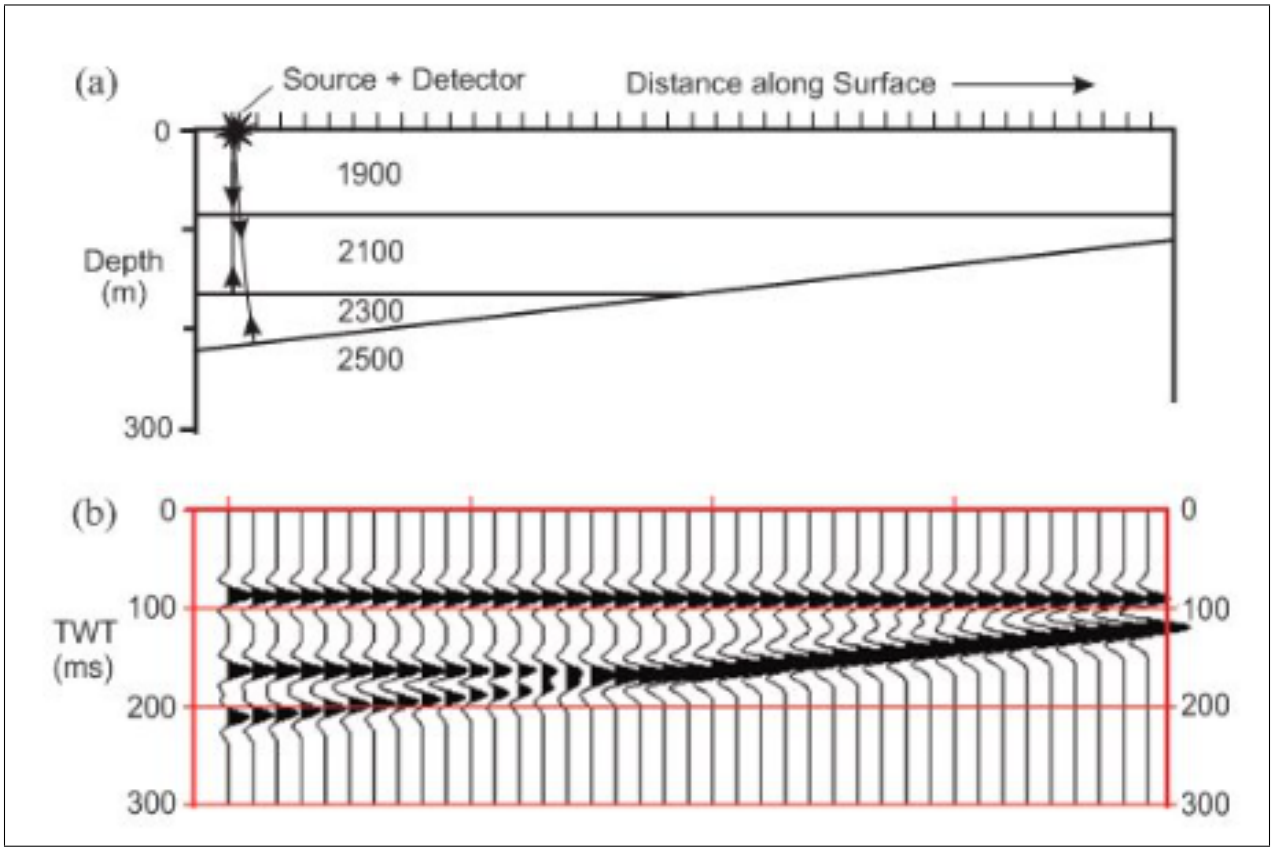

Figure 3.8: a) is showing seismic energy propagating down, and reflected up from different layers with different velocities. General P-wave velocity values are displayed for each layer. b) shows a seismic section of traces for each shot, after the reflectivity have been convolved with a seismic pulse. Figure adopted from Ashcroft (2011).

3.3.2 Seismic wave propagation

As the source signal moves away from the shot-point, it can be though of as a spherical wavefront. The wavefront becomes larger as it propagates downwards, and is called geometrical spreading. Because some energy will vanish in the form of heat due to internal friction in rocks, the energy becomes weaker with depth, called attenuation. The first step in processing is often to account for geometrical spreading by enhancing the reflection strength. The higher frequency content of the wavefront will have a greater attenuation than the lower frequency content, due to a higher internal friction in the rocks (Ashcroft, 2011).

Seismic wave energy propagating through the earth is described through the concept of ray paths and wavefronts in seismic. Huygen's principle (Figure 3.9) states that secondary sources at a certain position sends out energy to create a new wavefront at a propagated position. A ray-path is a trace of the wavefront at one specific point at the wavefront (Figure 3.10). The ray-path is always at right angles to the wavefront. In Figure 3.10, different types of waves are defined. The direct wave (D), is the first arrival wave which travels directly from the source to the receivers. The head wave (R_h), is a phenomena that occurs when the velocity contrast between layers is large, and the energy is refracted along an interface. Refracted waves R_f are energy transmitted through an interface (Gelius and Johansen, 2010). Ray-path theory is often used in seismic modelling, to illustrate seismic travel paths and derive equations that relate travel-time to distance (Ashcroft, 2011).

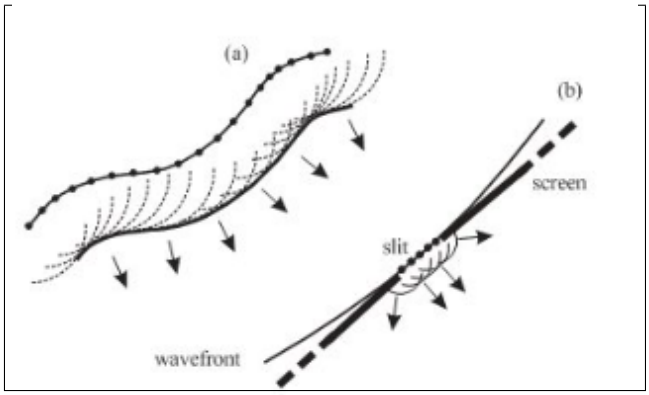

Figure 3.9: a) Huygens principle, where secondary sources send out energy that creates a new wavefront. b) Diffraction point, where secondary sources at the narrow edge of the reflector sends out diffracted energy. Figure adopted from Ashcroft (2011).

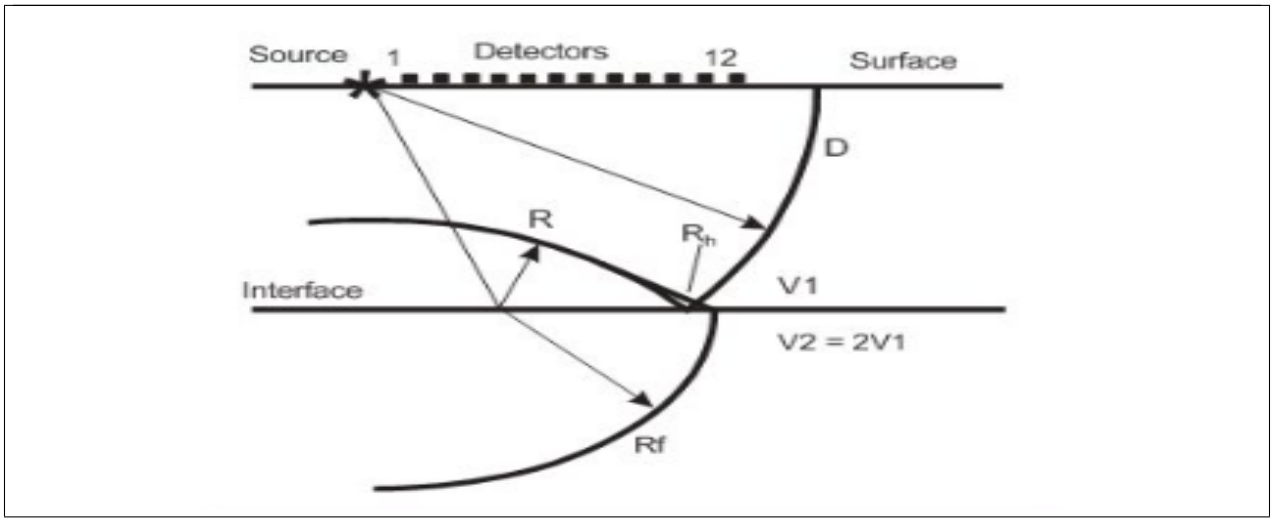

Figure 3.10: Ray-paths(R) from a source are reflected with its wavefront (thick lines). D is the direct wave, R_h is the head wave, and R_f is the refracted wave. Figure adopted from Ashcroft (2011).

3.3.3 Ray-based PSDM convolution

The seismic modelling used in this study is a ray-based 2D convolution modelling designed to simulate prestack depth-migrated (PSDM) seismic sections (Lecomte et al., 2003, Lecomte, 2008; NORSAR SeisRoX software, SimPLI patent). It classifies the reservoir model into the geological, elastic and reflectivity domain, also accounting for the wave propagation down and up from the reservoir model (Norsar, 2016). The standard seismic modelling tool for a fast and easy-to-use method in oil industry, has been the 1D convolution method in the time domain. This method calculates reflectivity from horizontally layered interfaces, and convolves them with a time pulse (Lecomte et al., 2015). In the 1D convolution case, no survey geometry, illumination, or lateral resolution effects are taken into account.

2D convolution have been based on a methodology called Simulated Prestack Local Imaging (SimPLI). SimPLI combines the reflection properties of the reservoir model with illumination and resolution information for a background model and survey. This is performed in order to quickly simulate the pre-stack depth migrated (PSDM) seismic response (Lecomte et al., 2003; Lecomte, 2008). Prestack depth migration (PSDM) is the ultimate processing performed on seismic data in order to produce proper depth images

of the subsurface. PSDM is very sensitive to the velocity model chosen. Data is not stacked first from flattened CMP gathers, further (poststack-time or -depth) migrated, but is instead directly depth migrated, thus being more naturally stacked at the actual depth locations of the reflectors. The recorded seismic energy will thus undergo a summation operation, which still increases the signal-to-noise ratio (as in conventional stacking), while being mapped back to proper depth in the subsurface. The PSDM technique is today the processing technique that gives the best imaging of the subsurface (Gelius and Johansen, 2010).

The SimPLI convolution is performed in the 2D or 3D prestack-depth domain with a convolution operator called a Point-Spread Function. A PSF is defined as the PSDM response of a point scatterer. Because Huygens principle postulates that a reflector can be seen as a superposition of point scatterers, the migrated seismic response of a reflector can be seen as the superposition of PSFs. It is thus important to model PSFs in order to understand seismic reflection images (Lecomte et al., 2015). An important parameter in the SimPLI method, is the reflectivity. The reflectivity is calculated from the input geological model, and is then filtered out by the PSDM filter to simulate PSDM images. The reflectivity can be calculated using different approaches, but the Zoeppritz equation gives the closest values to real reflectivity (Gelius and Johansen, 2010).

An important parameter for the reflectivity calculations is the incident angle. The incident angle can be chosen as an angle range, where reflectivity cubes are created for each incident angle. An easier option, is the average angle method. An average incident angle is estimated from the available illumination vectors and the input reflectivity is calculated according to that average angle. The latter method is used when the main goal is to study the structural image, rather than the illumination and resolution as function of incident-angle ranges (as in AVO/AVA studies) (Lecomte et al., 2016).

2D convolution modelling requires a background velocity model, a target model and a selected imaging zone in the latter as in Figure 3.11. The background model is a smooth velocity model used to simulate the wave propagation by ray-tracing from the survey to the sub-surface target. It is defined as overburden layers with elastic properties, and

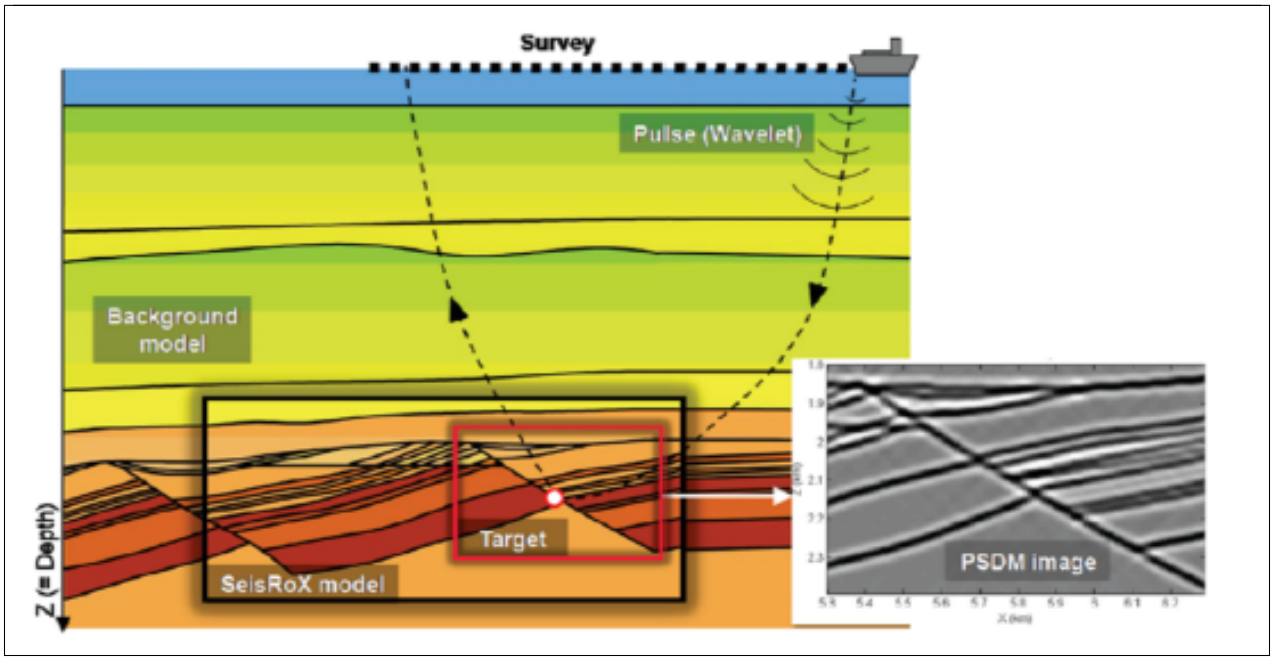

Figure 3.11: SeisRoX multi-scale model, showing the relation between the background model, SeisRoX reservoir model, and the local target. Figure adopted from Norsar (2016).

can be simple or complex. However, the background model needs to be smooth at the interval where the target is. The overburden layers will be used to calculate illumination vectors at illumination points in the target, that form the basis for the PSDM filters. The target model must contain elastic properties in order to estimate the reflectivity. The elastic properties may be either directly assigned or derived via rock physics models from petrophysical/reservoir parameters (porosity, mineral and fluid compositions, etc). Alternatively, one can use simpler reflectivity calculations by using AVO parameters such as intercept (R0) and gradient. If a target is sufficiently small in all directions, a local-target case is defined. For this situation the PSF will not vary significantly in the target, and the same PSF is assigned to the whole zone. For the local-target one PSF in the middle of the target is convolved with the reflectivity cube (Lecomte, 2008). By using a constant PSF, the spatial convolution is allowed to be performed as a multiplication in the wavenumber domain between the PSDM filter and a fast fourier transform of the reflectivity. The inverse of the fast fourier transform of the products will give the desired spatial image, and permits an almost real-time modelling. This method is highly efficient and important when wanting to test various models efficiently (Lecomte et al., 2015).

Ray-tracing on its own, cannot produce complete synthetic seismograms, due to its high-frequency approximation of the wave-equation (Gelius and Johansen, 2010; Lecomte et al., 2016). Thus, the modelling method do not calculate the low-frequency portion of the wave-equation. This implies that seismic attributes related to the wave-equation such as diffraction and interference energy, cannot be obtained (Kaschwich et al., 2011). Diffraction energy can give important information about faults and fractures in sediments, and can be important to investigate for fluid expulsion, gas venting and fluid filled fractures. However, the ray-based 2D convolution method is able to account for diffractions by applying a demigration method (Kaschwich et al., 2011). Demigration is simply put the inverse of migration, where the PSDM migrated image is returned to the initial time section (Kaschwich and Lecomte, 2010). Thus, diffraction energy is added to the ray-based PSDM modelling, although it uses ray-tracing methods.

3.3.4 PSDM filter and PSF

Seismic resolution is defined as to how well the seismic "sees" the subsurface of the earth (Chopra et al., 2006). As a seismic interpreter, a crucial goal is to enhance the frequency bandwidth, in order to improve seismic resolution. The seismic resolution might be the most important aspect of seismic, because it governs which stratigraphic structures and artifacts the seismic is able to reveal (Chopra et al., 2006).

As stated earlier, the background model is used to create illumination vectors at a target illumination point P. For each source-receiver pair (S-R) of a selected survey, slowness vectors at point P, can be produced from the source to the illumination point (p_S), and receiver to the illumination point (p_R) (Figure 3.12). The slowness vectors are used to calculate the illumination vector ($I_{SR} = p_R - p_S$), and all possible illumination vectors at the target point are collected. By adding a wavelet (Figure 3.12,b) to the illumination vectors, a PSDM-filter is generated in the wavenumber domain (KX, KZ). An inverse fast fourier transform is thus applied to the filter to get the PSF (Lecomte et al., 2015). The PSDM filter indicate what the potential resolution and illumination of the reflector, depending on frequency bandwidth of the wavelet, and the amount of energy (volume) occupied by the filter in the wavenumber domain. The resolution thus depend on a

combination of the illumination vector coverage, frequency band, incident angle and velocity at point P (dependent on the slowness vector). A larger incident angle or velocity will result in a smaller volume coverage in the PSDM filter, while good resolution and illumination is associated with a large filter volume coverage (Lecomte, 2006).

In seismic, resolution often is divided into vertical and horizontal resolution. Resolution can be directly gathered from the PSDM filters and PSF. The PSDM filter is the coverage made by the scattering wave-numbers in the wave-number domain (KX,KZ in Figure 3.12). The scattering wavenumber vector k_{SR} is defined as the product of frequency ν and

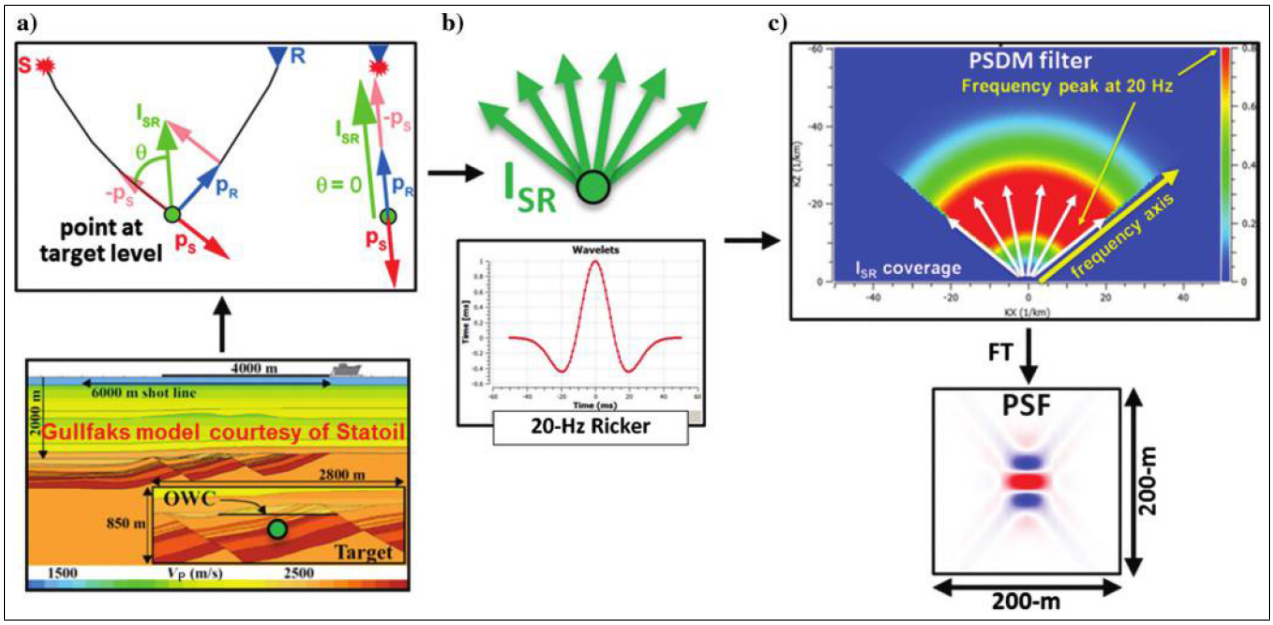

Figure 3.12: a) Velocity model and illumination (I_{SR}) vector for a shot-receiver (S-R) pair at the target, b) (I_{SR}) for the survey combined with a Ricker wavelet, to generate c) the PSDM filter and the PSF. Figure adopted from Lecomte et al. (2015).

illumination vector I_{SR}: $k_{SR} = \nu * I_{SR}$ (Lecomte, 2008). The length of the wave-number is proportional to the frequency, and inversely proportional to the local velocity at the image point. So for larger frequency bands, the coverage in the wave-number domain increase, and the resolution becomes sharper (Lecomte, 2006). An estimation of the horizontal and vertical resolution can be found from the wave-number coverage in the wave number domain, giving the horizontal resolution :$\frac{2\pi}{\Delta K_X}$ and the vertical resolution: $\frac{2\pi}{\Delta K_Z}$ (Lecomte, 2008; Gelius and Johansen, 2010). Subsequently, the PSF can also be used to find the resolution. This can easily be done by only measuring the difference in length of the PSF

for horizontal resolution, or in height for vertical resolution.

3.3.5 PSDM simulators

Different Workflows exist in the 2D convolution modelling, which include Analytic PSDM filter, Local-target PSDM Simulator, and Full-field PSDM Simulator. The local target PSDM Simulator has been briefly discussed earlier, and makes use of the ray-based 2D convolution approach. By defining a survey, background model and target model, a small local-target can be defined. The simulator is quick and efficient when calculating the prestack depth migrated seismic response, due to the fact that the PSF is constant for the entire reflectivity cube. The in-line width for this simulator can be up to 1-2 km, while the thickness should only be a few hundred meters (Norsar, 2016).

The full-field PSDM Simulator is used in order to cover a large area, for example the entire reservoir model. When the coverage area is large, the assumption that the PSF is constant over the entire area is invalid. Instead, a grid is defined to calculate the PSF at different areas selected by the user. However, the full-field simulator will not be utilized in the study because a full reservoir is not needed.

The Analytic PSDM filter has no survey nor background model, and no illumination vectors are calculated. An analytic PSDM filter is a direct design of the volume occupied in the wavenumber domain. It is defined by an average velocity, incident angle and the maximum dip of illuminated reflectors (Lecomte et al., 2016). For all simulators, the sampling intervals are important to define. The default value in the 2D convolution is a sampling of 10 m horizontally and 5 m vertically. However, a too coarse sampling might distort the PSDM filters, and also damage the input reflectivity if the input target model is detailed and does require a high level of details. The sampling should be chosen according to sampling of real data, but also according to the input geological model (Lecomte et al., 2016).

Chapter 4

Data and Method

In this chapter the rock physics and seismic modelling method will be outlined, and values used in the modelling procedures will be explained. Rock physics modelling methods have been outlined in the previous chapter, hence this chapter is not explaining the methods in detail.

For the seismic modelling, values obtained from the rock physics models are used. Models created in MATLAB will be presented in the results chapter. The impact and effect of gas hydrate distribution and saturation on the BSR is the main part of the investigation. The study will be divided into three cases:

- **Case 1**: Simple horizontally layered model, where wiggle-traces are investigated in the seismic.
- **Case 2**: More complex stratigraphy, with a cross-cutting BSR over intertwined free gas/brine saturated layers.
- **Case 3**: Similar model as the gas hydrate system at the southern Vøring plateau. Comparison with the real seismic data is performed in the seismic.

4.1 Rock physics modelling

The rock physics modelling is performed in MATLAB. Scripts already verified was provided through a MATLAB-package by Erling Jensen and Åsmund Drottning in Rock Physics Technologies (RPT). Some of the scripts have been modified extensively, in order to fit equations to the purpose of this study. Through modelling, elastic properties for three gas hydrate distributions have been calculated. 1) hydrate cementing at grain contact, 2) hydrate cement coating, enveloping grains, and 3) hydrate as inclusions away from grain-contact. Model 1) and 2) are calculated using the CCT/SCA approach described by Johansen et al. (2003) and Dvorkin et al. (1999), while model 3) is calculated by the use of Gassmann's formula for lower gas hydrate saturations.

The gas hydrate reservoir at the southern Vøring plateau is reported by Bünz and Mienert (2004) to occur at 270 m below the sea-floor, with approximately 950 m of sea-water above. To calculate density, P and S-velocity for gas hydrate saturated sediments, elastic properties from the survey area are used. The bulk and shear modulus for the grains were calculated using the Hill average Equation 3.4, and the density was calculated using the Voigt Equation 3.3. Properties used are listed in Table 3.1. The gas reservoir was reported 300 m below the sea-floor with a slightly different mineral composition than the gas hydrate layer (Bünz and Mienert, 2004). The elastic properties for sediments containing gas and water, was calculated using the Hertz-Mindlin theory (Equations 3.10 and 3.11) and Gassmann's formula (Equation 3.14).

Additional parameters used in the MATLAB modelling are given in Table 4.1. The critical porosity and coordination number relation is discussed by Dvorkin and Nur (2002) for sandstones. The critical porosity for sandstones and for most sedimentary rocks are proposed to be 40%. The number of grain contact points increase with compaction and decreasing porosity. In this study a critical porosity of 40% and coordination number of 8.2 are used, as proposed by Johansen et al. (2003).
In the results section, models for V_p, V_s and ρ are shown for the gas hydrate and free gas bearing sediments. For the gas hydrate layer, two cases are considered. 1) Gas hydrate pore-filling dry pore voids until 100% saturation, and 2) water/gas hydrate mixture filling

Table 4.1: Parameters used in the Rock physics modelling.

Parameters	Values	Reference
Gas Hydrate (S1), bulk modulus	7.7 [GPa]	(Waite et al., 2000)
Gas Hydrate (S1), shear modulus	3.2 [GPa]	(Waite et al., 2000)
Gas Hydrate (S1), density	910 $[kg/m^3]$	(Waite et al., 2000)
Gas Hydrate (S2), bulk modulus	5.6 [GPa]	(Yun et al., 2005)
Gas Hydrate (S2), shear modulus	2.4 [GPa]	(Yun et al., 2005)
Water, bulk modulus	2.4 [GPa]	(Johansen et al., 2003)
Water, density	1030 $[kg/m^3]$	(Chand et al., 2006)
Methane gas, bulk modulus	0.1 [GPa]	(Helgerud et al., 1999)
Methane gas, density	230 $[kg/m^3]$	(Helgerud et al., 1999)
Critical porosity	0.4	(Johansen et al., 2003)
Coordination number	8.2	(Johansen et al., 2003)

dry voids. Both cases are computed for hydrate cement at grain contact (Scheme 1) [1], and hydrate cement coating/enveloping grains (scheme 2) [2]. All rock physics values used in the seismic modelling will be for structure 1 hydrates, but structure 2 hydrates are added to the rock physics plots, in order to observe the difference.

4.2 Geological models

Using the 2D model-builder, geological models for three cases are created. Different procedures creating the geological models are outlined. Models are assigned properties calculated from the rock physics methods, and models displaying V_p, V_s and ρ can be viewed in Appendix A.

4.2.1 Case 1: BSR study

For the first case a simple plane reservoir model is created in the 2D model-builder. In the rock physics modelling of gas hydrate and free gas bearing sediments, the pore voids are

[1] Scheme 1 will refer to gas hydrate cementing at grain contact (Figure 3.6, A)
[2] Scheme 2 will refer to gas hydrate cement coating/enveloping entire grains (Figure 3.6, A)

assumed to be fully saturated with brine and gas hydrate/gas. This is rarely the case in nature, but deemed sufficient in this study. 5 horizontal layers are created in the model builder (Figure 4.1). In Table 4.2, the outline for the 7 models simulated in the seismic modelling are displayed.

Table 4.2: Different models for case 1

Models	Layer 1	Layer 2	Layer 3	Layer 4	Remark
Model 1	100% Brine	25% Gas Hydrate	100% Brine	100% Brine	
Model 2	100% Brine	100% Gas Hydrate	100% Brine	100% Brine	Scheme 1*
Model 3	100% Brine	25% Gas Hydrate	50% Gas/Brine	100% Brine	
Model 4	100% Brine	100% Gas Hydrate	50% Gas/Brine	100% Brine	Scheme 1*
Model 5	100% Brine	0% Gas Hydrate	50% Gas/Brine	100% Brine	No Gas Hydrate
Model 6	100% Brine	100% Gas Hydrate	100% Brine	100% Brine	Scheme 2**
Model 7	100% Brine	100% Gas Hydrate	50% Gas/Brine	100% Brine	Scheme 2**

* Scheme 1: Gas Hydrate cementing at grain contact.
** Scheme 2: Gas Hydrate cement coating entire grains.

Table 4.3: Parameters used for modelling case 1

Layer	ϕ [%]	C_0	V_p [km/s]	V_s [km/s]	ρ [g/cm^3]	Depth [km]	Remark
Water			1.50	0.00	1.03	0.95	Sea water
Layer 1	45	7.5	2.02	0.88	1.93	0.20	100% Brine saturated
Layer 2	40	8.2	*	*	*	0.05	Gas Hydrate layer
Layer 3.1	40	8.2	1.5	0.98	1.86	0.10	50% Gas/50% Brine
Layer 3.2	40	8.2	1.65	0.93	1.98	0.10	10% Gas 90% Brine
Layer 3.3	40	8.2	2.09	0.92	2.01	0.10	100% Brine saturated
Layer 4	36	9.0	2.19	1.00	2.08	0.50	100% Brine saturated

* Properties for gas hydrate layers changes with the saturation. Table 5.1.

In Figure 4.1, each block is assigned a color. Block 1 is the sea-water column, stretching 950 m in vertical direction. Layer 1 corresponds to block 2, and is the sea-floor sediments saturated with brine. Layer 2 corresponds to block 3, and is the gas hydrate reservoir. Layer 3 corresponds to block 4, and is the gas/brine saturated sediments. Finally layer 4 corresponds to block 5, and is deeper brine saturated sediments. Layers 1-4 are calculated using the rock physics methods previously described. Parameters and elastic properties used and calculated from the modelling are listed in Table 4.3. The model created in

the 2D model-builder, have been made completely horizontal. The horizons have been picked, before creating the assigned blocks between interfaces. Velocity and density values assigned to each block are constant in the respective layer.

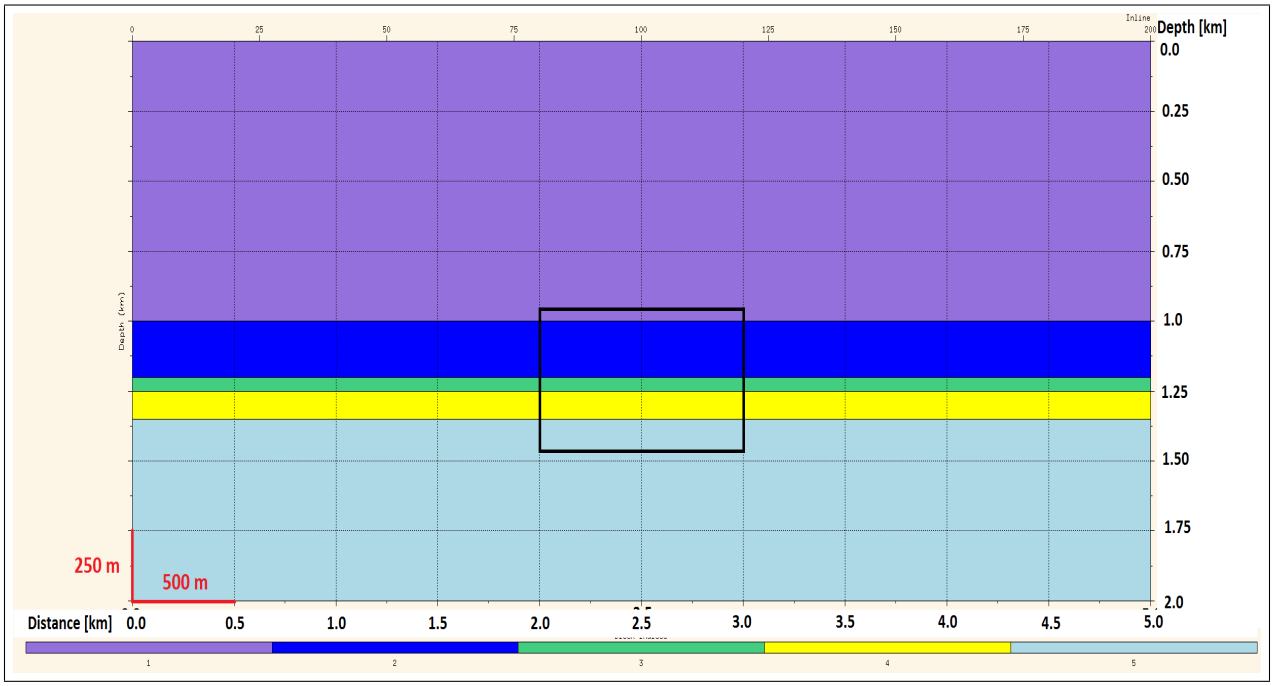

Figure 4.1: Geological model from the 2D model-builder for case 1. Blocks 1-5 corresponds to layers with different acoustic properties. Black square is confining the area where the wiggle trace will be extracted from.

The modelling of gas hydrate-bearing sediments with the CCT/SCA modelling method, are performed for different saturations and distribution schemes. The gas hydrate parameters used in the seismic modelling will be listed in the results section, and not in Table 4.3. Case 1 is similar to what Ecker et al. (1998) did, simulating hydrate as inclusions, and contact cement filling material. The results were in this case found using the Thomson-Haskell reflectivity method, and the synthetic data was compared to real seismic data from the Blake Outer Ridge. Synthetic CMP gathers was plotted for 25% and 75% gas hydrate saturation for the different distributions (Ecker et al., 1998). The elastic properties for the different layers in this model are similar to those obtained from Ecker et al. (1998), but different distribution schemes and rock physics approaches are used in this study.

4.2.2 Case 2: Gas hydrate saturation study

For case 2, a more complex reservoir model is created. The purpose of the study is to observe the effect between gas hydrate and free gas/brine saturation on the BSR. The reservoir model is made relatively similar to the observed BSR at the southern Vøring plateau (Black square in Figure 3.2). Free gas layers have been observed at this cite to be trapped by the BSR (Bünz and Mienert, 2004). However, the observed BSR is believed to occur mainly due to the free gas layers, and not the gas hydrates (Bünz et al., 2005), (Andreassen et al., 2003). The velocities and densities from the study area, are much lower than the values obtained for fully water saturated sediments in this study, as expected (Andreassen et al., 2003). Because Bünz et al. (2005) and Andreassen et al. (2003) are in agreement that the gas hydrate saturation at the study area, is too low to cement grains, the values for all sediment layers used in this case are calculated using rock physics methods in order to get a more realistic response.

Table 4.4: Different models for case 2

Gas Hydrate layer		
Models	**Gas Hydrate saturation**	**Remark**
Model 8	25% Gas Hydrate	Hydrates deposited away from grain contact
Model 9	75% Gas Hydrate	Hydrates cementing at grain contact
Model 10	75% Gas Hydrate	Hydrate cement coating grains
Model 11	100% Gas Hydrate	Hydrates cementing at grain contact
Model 12	100% Gas Hydrate	Hydrate cement coating grains
Other layers		
Layer	**Saturation**	**Remark**
Gas layers	10% gas 90% brine	Same properties as layer 3.2 (Table 4.3)
Top Brine layer	100% brine	Same properties as Layer 1 (Table 4.3)
Bottom Brine layer	100% brine	Same properties as layer 4 (Table 4.3)

The gas layers in Figure 4.2, are approximately 10 m in vertical direction, while the gas hydrate layer is approximately 50-100 m in vertical direction. The different compositions for the different models are given in Table 4.4. Velocity and density parameters for the gas hydrate layers are given in the results section (Table 5.1). In Figure 4.2, the layers to the right of the BSR are brine and gas saturated sediments overlying each other. Properties used for the brine saturated sediments in this area are given for layer 3.3 in Table 4.3.

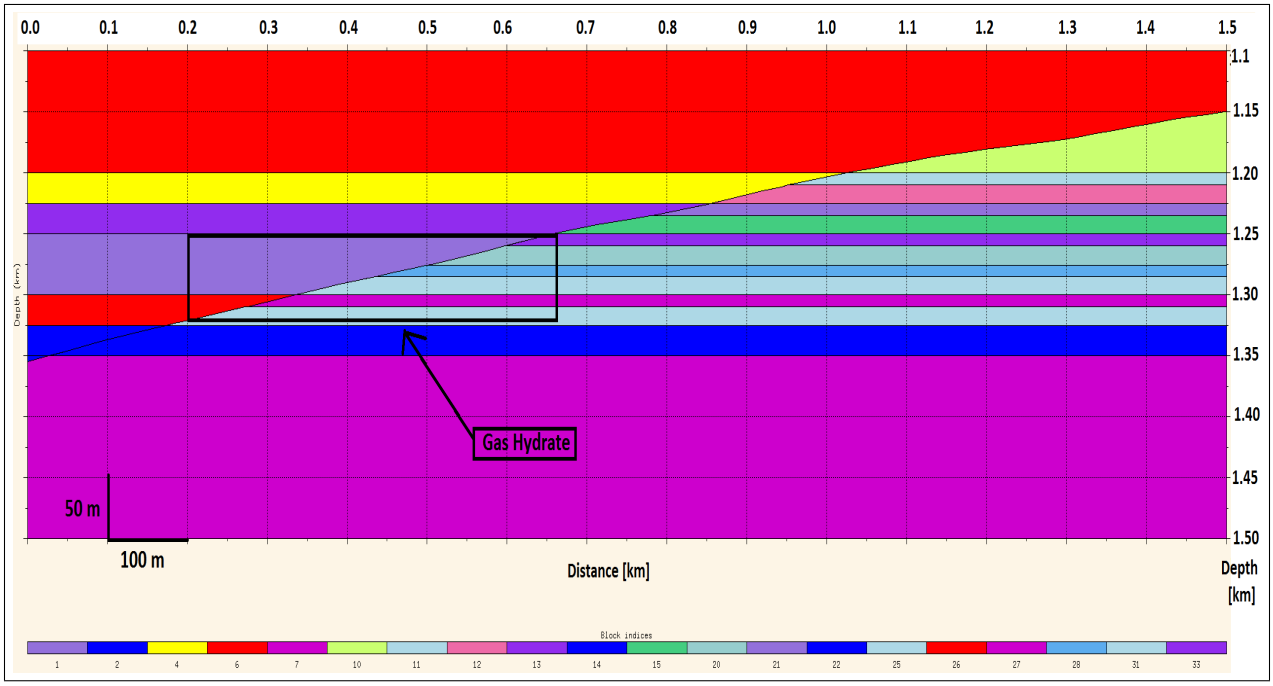

Figure 4.2: Geological model from 2D model-builder for case 2. The BSR is cross-cutting stratigraphic layers, as observed in the figure. The small layers to the right of the BSR, is free gas and brine bearing sediments. The layers confined in the black square to the left, is where the gas hydrate reservoir is located.

For case 2, V_p, V_s and ρ properties for the gas hydrate saturated sediments are assigned to their respective layers by using the sampled function tool in the model-builder. Property samples are selected, and a fitted line is assigned between each point, in order to create a smooth function. A closer sampling will give a smoother line, and consequently a better fit. The sampled function can be done in horizontal or vertical direction, and will not have an interface assigned to the varying properties. A horizontal sampled function is selected in this case, where the saturation of gas hydrates will be at its highest inside the black square to the left of the BSR in Figure 4.2. However, there will be an interface above the gas hydrate layer which will give a strong reflection. The reflection associated with the top of the hydrate zone will be unrealistic, because the gas hydrate saturation will decrease away from the BGHZ, and rather result in an amplitude blanking zone above (Lee and Dillon, 2001; Yang et al., 2014).

4.2.3 Case 3: Comparison with real seismic data

For case 3, a geological model is created in order to investigate the gas hydrate system observed at the southern Vøring plateau. The previous cases (1 and 2) have used relatively simple stratigraphic horizons, and elastic properties only obtained from rock physics modelling. For this case, properties for V_p, V_s and ρ are found from the articles (Bünz et al., 2005), and (Andreassen et al., 2003), while the gas hydrate reservoir properties are found from the rock physics modelling using CCT/SCA theory.

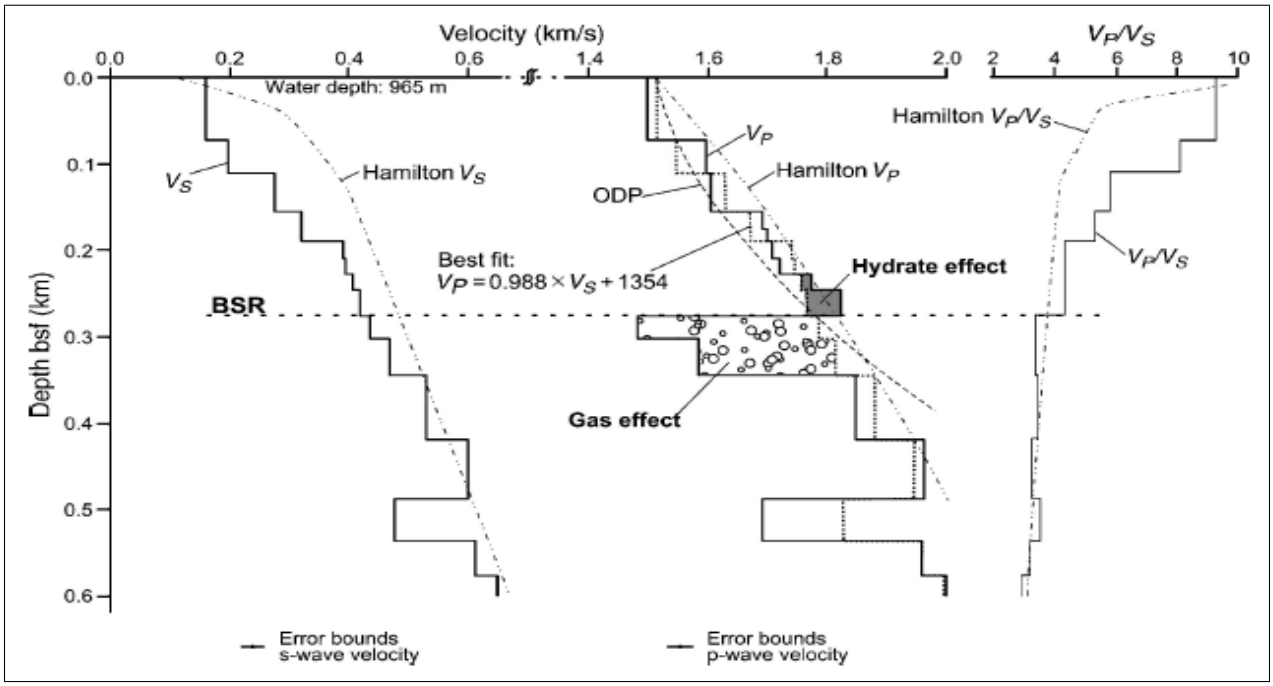

Figure 4.3: V_p, V_s, and Vp/Vs curves from the OBS (solid lines) adopted from Bünz et al. (2005). The values are compared with Hamilton models and the best fit curve, described with equation (3.1), in order to observe the effect of gas and gas hydrates.

Bünz et al. (2005) created a velocity chart for the survey area, given in Figure 4.3. The best fit curve, given by the lithology Equation 3.1, shows no effect for the gas hydrate or free gas present. It is used in order to see the effect related to gas hydrates and free gas. The geological model in case 3 is confined to a depth of 1.1-1.3 km, and a horizontal length of 2.75 km. The values obtained from Figure 4.3, and Andreassen et al. (2003), are given in Table 4.5. The gas hydrate and free gas layers are assigned values from the rock physics

modelling. Since stratigraphic layers are slightly dipping, it is difficult to assign precise values to each layer depending on depth, but the variation will not be significant in any case, and the values in Table 4.5 are appropriate parameters.

Table 4.5: V_p, V_s and ρ for different depths in case 3.

Layer	V_p [km/s]	V_s [km/s]	ρ [g/cm^3]	Depth [km]
Layer 1	1.68 $^{(a)}$	0.28 $^{(a)}$	1.70 $^{(b)}$	1.15
Layer 2	1.70 $^{(a)}$	0.30 $^{(a)}$	1.72 $^{(b)}$	1.17
Layer 3	1.71 $^{(a)}$	0.35 $^{(a)}$	1.73 $^{(b)}$	1.19
Layer 4	1.72 $^{(a)}$	0.39 $^{(a)}$	1.74 $^{(b)}$	1.20
Layer 5	1.73 $^{(a)}$	0.41 $^{(a)}$	1.75 $^{(b)}$	1.21
Layer 6	1.74 $^{(a)}$	0.42 $^{(a)}$	1.76 $^{(b)}$	1.22
Layer 7	1.75 $^{(a)}$	0.43 $^{(a)}$	1.77 $^{(b)}$	1.24
Layer 8	1.76 $^{(a)}$	0.44 $^{(a)}$	1.78 $^{(b)}$	1.26
Layer 9	1.77 $^{(a)}$	0.45 $^{(a)}$	1.79 $^{(b)}$	1.27
Layer 10	1.79 $^{(a)}$	0.47 $^{(a)}$	1.80 $^{(b)}$	1.28
Layer 11	1.82 $^{(a)}$	0.50 $^{(a)}$	1.82 $^{(b)}$	1.31

$^{(a)}$ Based on values from Figure 4.3 (Bünz et al., 2005).
$^{(b)}$ Based on values from Andreassen et al. (2003).

The geological model for case 3, is found by picking horizons over a real seismic section in the model-builder digitizer tool. The seismic section have been taken from the black square in Figure 3.2. The horizons picked can be observed in Figure 4.4a. The horizons are imported into the model builder, and used in order to create the interfaces in the model. The geological model in Figure 4.4b, have a more complex geology than case 1 and case 2 as observed. The gas hydrate layer is created as a thin reservoir cross-cutting the sedimentary layers. The gas hydrate layer is divided into several small blocks, that are assigned properties. The BSR can in this case be observed in Figure 4.4a as the green line cross-cutting the almost horizontal layers.

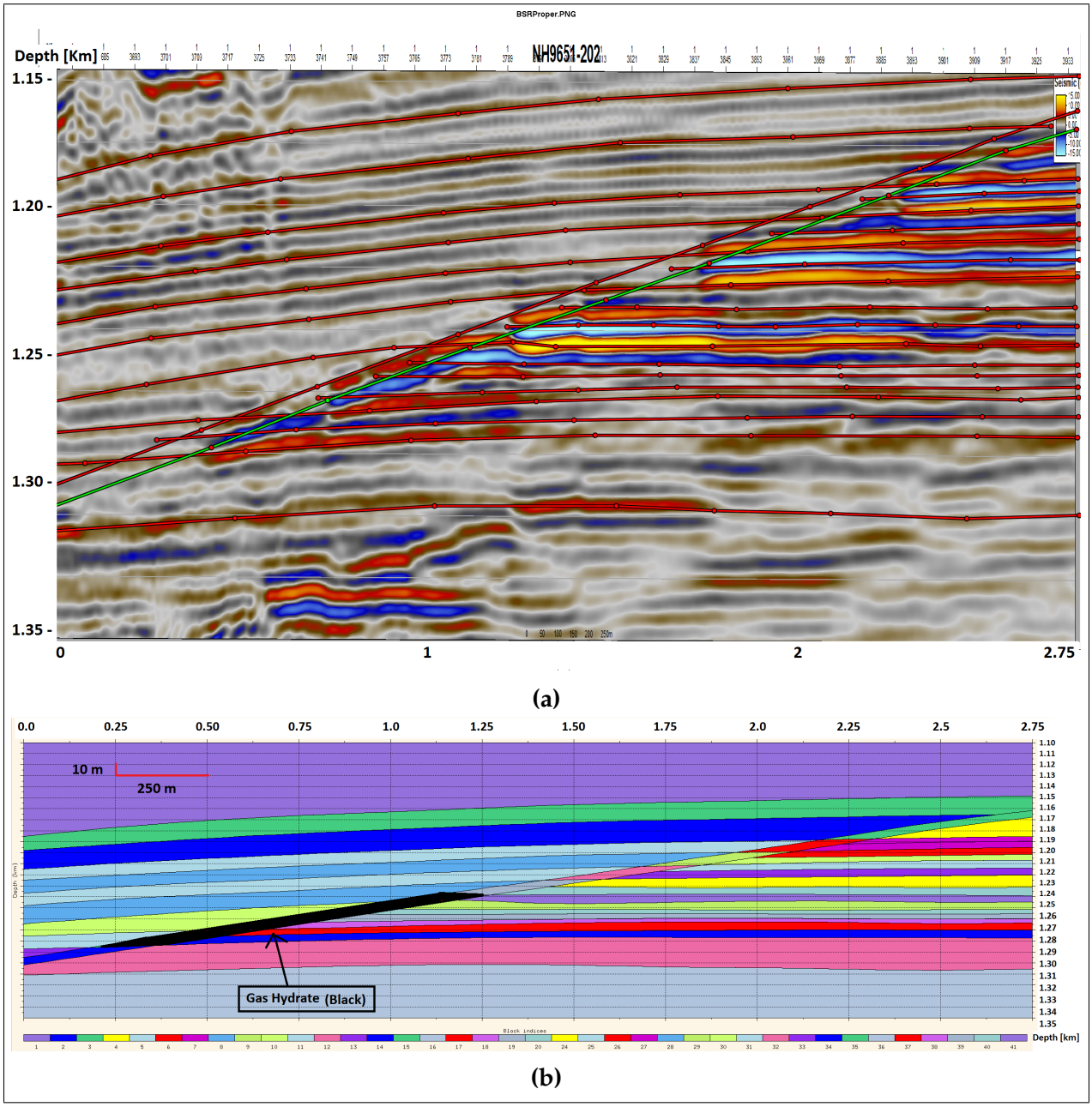

Figure 4.4: Showing the geological model for case 3. a) is the digitizer function, where interfaces are drawn on top of real seismic from NH9651-202 (Figure 3.2). The green line is the BSR. b) is the geological model after the digitizer horizons are imported into the 2D model-builder.

4.3 2D Convolution modelling

After creating models in the 2D model-builder, they are exported as a SMIF-file. In order to use the models in the 2D convolution, they have to be in 3 dimensions. By using the 3D model-builder, a 2.5D model can be created. The 2.5D model is only an extension of the 2D model, and will have a uniform structure and properties in the extended 3D space. For a more realistic modelling strategy, the models should be in 3D, to account for dipping structures, illumination issues, and survey acquisition direction, but this is beyond the scope of this study.

The 2D convolution approach for the same three cases from the previous section will be outlined. In this case study, analytical and local-target PSDM simulators will be utilized. For case 1, an analytic PSDM simulator is sufficient, while for case 2 and 3 the local-target PSDM simulator is used in order to define a marine survey and background model. Models for case 2 and 3, showing the survey, target, background model etc. are given in Appendix A.

4.3.1 Case 1: BSR study

In case 1, the Analytic PSDM simulator is utilized. This simulator is easy and effective, and no background model nor survey is needed. The PSDM filter is designed directly, using an average velocity instead of the background model. Some important parameters have to be defined. The first step is to select a target area, for where the PSDM filter and reflectivity is calculated. In the working box target, the sampling interval is defined. Sampling should be similar to real seismic data, but the simulator also depend on the input geological model. So for case 1, a sampling of 3 m in both horizontal and vertical direction is chosen. The average velocity over the target of interest is especially important to define, because this parameter have strong constraints on the overall resolution of the image. Higher velocities will give poor resolution, so the velocity should be chosen as an appropriate value (Lecomte, 2008). The parameters chosen for the analytic simulator in case 1, are listed in Table 4.6.

Different types of analytic PSDM filters exist, depending on the purpose of the study. For this study, the max reflector dip PSDM filter is sufficient. The max reflector dip is an option for defining the steepest reflector dip, that is to be illuminated (Lecomte et al., 2016). Since no illumination vectors are computed in the analytic simulator, the chosen PSDM filter will define the area that is to be illuminated. For a max reflector dip of 45°, the PSDM filter will consist of a vertical cone with a half opening of 45°.

Table 4.6: Analytic PSDM Simulator parameters

Parameters	Values
Sampling (Y, Z) [m]	(3, 3)
Average velocity [km/s]	2.00
Reflector dip range [deg]	0-45
Wavelet [Hz]	40
Angle range, incident angle [deg]	0
Gain, clip of amplitude	5, 5

The entire reflectivity grid of the model is directly assigned to the PSF, which depend on the wavelet. Higher frequency gives better resolution, but in reality higher frequencies are attenuated faster than lower frequencies, and the energy decreases with depth (Gelius and Johansen, 2010). For this case study a Ricker wavelet of 40 Hz in Figure 4.5 is chosen. In Figure 4.5, wavelets of 40 and 85 Hz are displayed. Both 40 Hz and 85 Hz wavelets are used for the other cases. When constructing the wavelet, a sample interval of 1 ms is chosen. A too coarse sampling of the wavelet will result in aliasing according to the Nyquist frequency (Gelius and Johansen, 2010). Because this case demonstrates a simple horizontal geometry and uniform elastic properties, the incident angle is believed to be of little importance, and is set to be zero.

4.3.2 Case 2: Gas hydrate saturation study

For case 2, the local-target PSDM simulator is utilized. By defining a background model and a survey configuration, a local-target is defined. The target should be sufficiently small (not more than 2 km in x-direction). The background model is defined as the same model in case 1, where the target is located at the depth of 1.1-1.3 km (Figure 4.6).

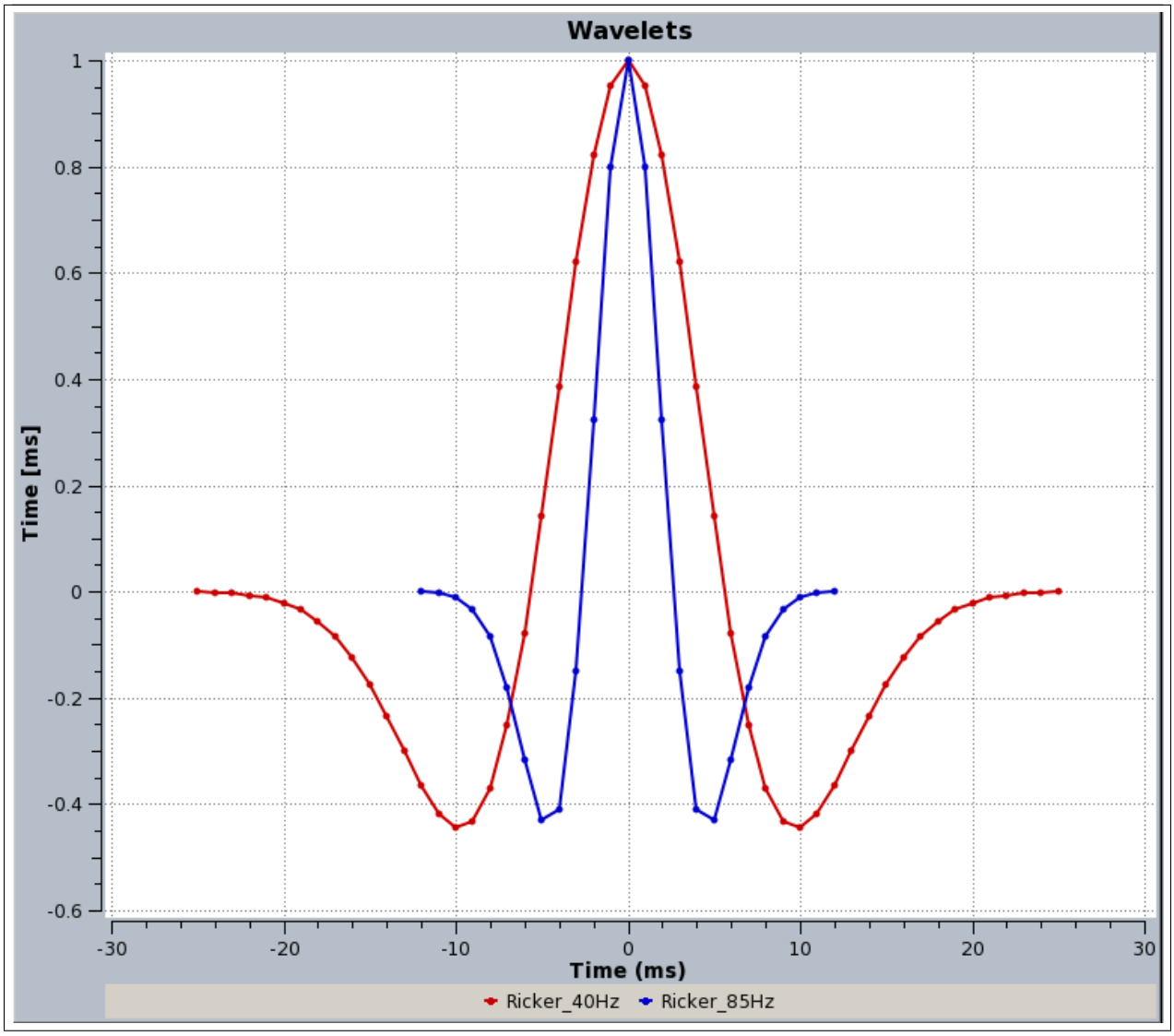

Figure 4.5: Ricker wavelet for a frequency of 40 Hz, and 85 Hz.

In Figure 4.6, the geological model for case 2, is implemented as a local-target reservoir in the model for case 1. However, the background model should be smooth in the local-target area, because large velocity changes in the target will affect the resolution. So, the background model will have uniform properties through the target area. The background model is essential in computing rays from source to receiver, subsequently affecting the illumination vectors and the resolution (Lecomte, 2006).

The survey, target and model can be viewed in Appendix A, to see the location relative

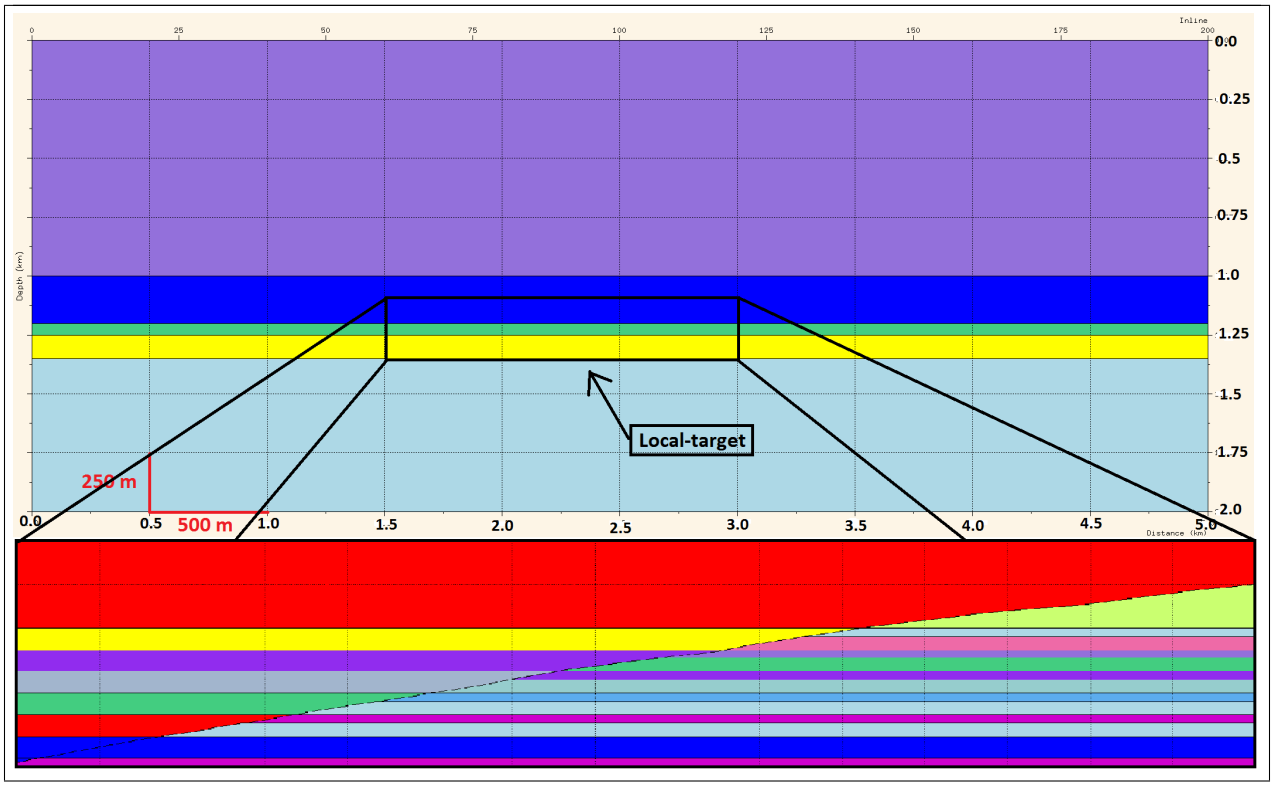

Figure 4.6: Background model for case 2. Showing the location for the local-target model

Table 4.7: Seismic survey parameters for case 2.

Shot Configuration		**Streamer/Receiver Configuration**	
Center (x,y)	(1.00, 0.20)	Absolute depth [km]	0.0000
Depth [km]	0.000	Minimum Offset [km]	0.1000
Rotation [deg]	0.000	Nr of Streamers	2
Nr. Shot lines	1	Streamer length [km]	1.2000
Shot line length [km]	3.000	Streamer spacing [km]	0.1000
Shot line spacing [km]	0.300	Receiver spacing [km]	0.0125
Shot spacing [km]	0.025	Receivers per Streamer	161
Nr. total Shots	121	Total nr of Receiver	322

to each other. In Table 4.7, the survey configuration for the shot and receivers is listed. Because the model in case 2 is in 2.5 dimensions, only 1 shot line is defined, stretching 3 km in length with shots for every 25 m. The survey is chosen as a marine survey, meaning that the shots and receivers are moved every 25 m. 2 streamers with a length of 1.2 km and 100 m spacing are selected. On each streamer, 161 receivers are located with a spacing of 12.5 m. The survey parameters are chosen from a standard marine survey configuration, similar to the 2D multichannel line configuration from Bünz and Mienert (2004).

In the local-target PSDM simulator, a working box also called the local PSDM target is chosen as done in case 1. The sampling is 3m in both vertical and lateral direction. A wavelet of 40 Hz frequency (Figure 4.5) is chosen for this case, corresponding well with the chosen sampling intervals.

4.3.3 Case 3: Comparison with real seismic data

For case 3, both analytic and local-target PSDM simulators are used. The analytic PSDM filter is used in order to see the full seismic model, while the local-target focus at the BSR proper area. Here, the BSR proper is where a continuous reflection at the BGHZ occurs, which coincide with the area displayed by arrows in Figure 4.7. The aim for case 3 is to create a model similar to the observed gas hydrate section in Figure 4.7. As suggested by Bünz et al. (2005), the termination of enhanced reflections due to underlying free gas, probably implies that gas hydrates act as a trap or a seal. However, the gas hydrate saturation is not great enough to show a clear BSR at these areas. (Bünz et al., 2005).

The real seismic data was obtained by Norsk Hydro, using a 2D multichannel seismic line (NH9651-202) for the acquisition. A 1.2 km streamer with 96 channels was used, where adjacent traces were summed, giving a total of 48 channels per shot. The Common Depth Point (CDP) spacing was set to 12.5 m. The seismic line was towed in a SW-NE direction, with a main frequency of 85 Hz (Bünz and Mienert, 2004). The survey for the local-target PSDM simulator is the same as in case 2 (Table 4.7), corresponding to the known survey parameters for the seismic line NH9651-202. However, the shot-line length is changed from 3 km to 5 km.

The background model is created using velocity and density information from Bünz and Mienert (2004) and Andreassen et al. (2003). Defining the background model, can be performed in 1 or 3 dimensions. The 1D background model calculate the ray-path using an Eikonal-solver, while the 3D model use ray-tracing. The 3D background model is created by defining a grid-layer cake model, where the properties can be chosen to vary

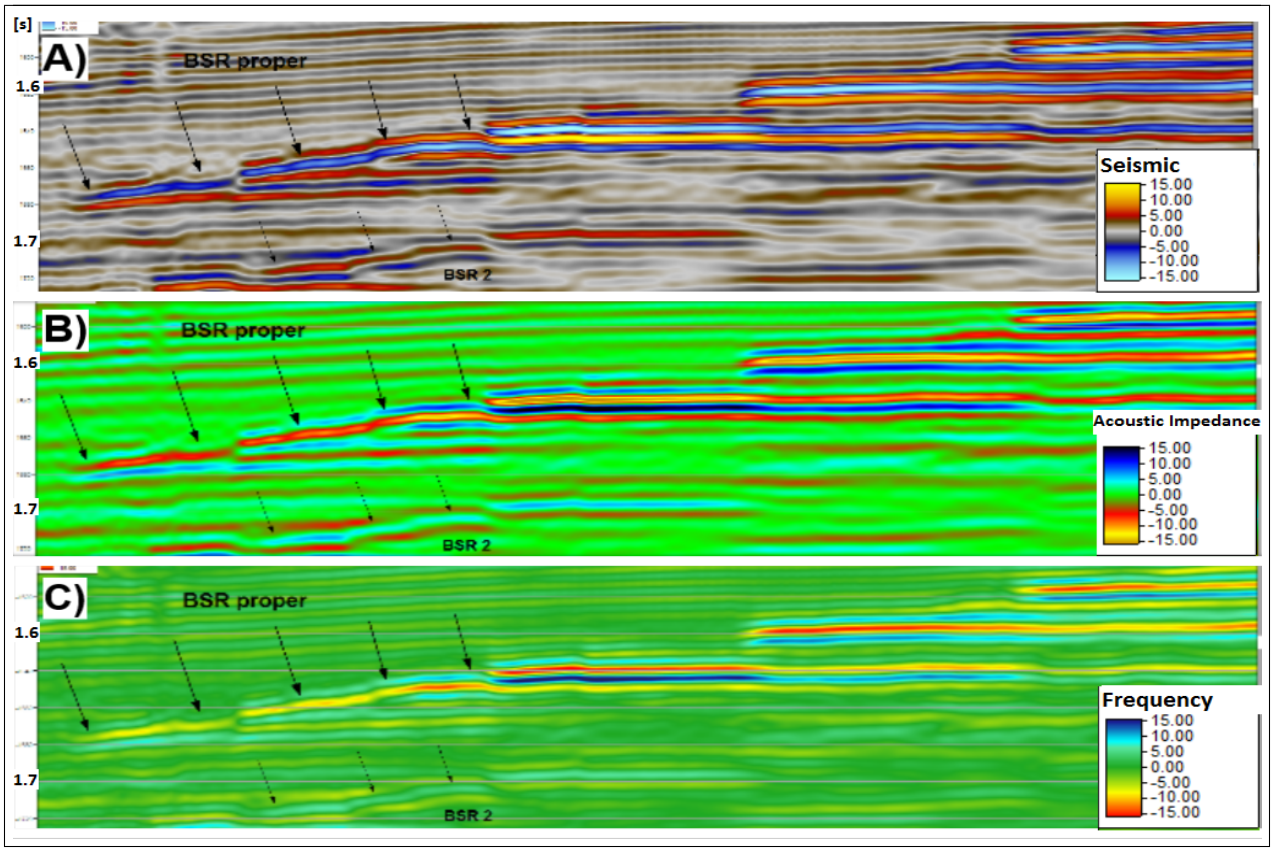

Figure 4.7: Seismic sections from Figure 3.2, black square. Displaying different coloring options to show the BSR proper easier. BSR 2 is believed not to occur because of gas hydrates. A) Regular seismic, showing the BSR as in Figure 3.2. B) Acoustic impedance color with reversed coloring for the positive/negative. C) Instantaneous frequency color, showing the BSR clearer than the other plots. Seismic images obtained from Petrel

between layers. A grid layer cake model is created as a background model in case 3, with parameters shown in Table 4.8.

Table 4.8: Parameters for background model, case 3.

Layer	V_p [km/s]	V_s [Km/s]	$\rho[g/cm^3]$	Depth [km]
Sea water	1.50	0.00	1.03	0.00
Sea floor*	1.50	0.18	1.58	0.95
Top Hydrate	1.70	0.30	1.70	1.15
Bottom Hydrate	1.82	0.50	1.82	1.35
Base line	2.00	0.65	2.00	1.50

* Parameters vary with depth down to the next layer.

The working box assigned to the local-target is chosen to be 0.6-2.1 km in length from the original geological model (Figure 4.4b). Because the main frequency in the real seismic data is 85 Hz, this wavelet is used in case 3 as well. In addition, a wavelet of 40 Hz is used (Figure 4.5), in order to highlight the difference in resolution for layers smaller than 10 m in thickness. Sediments containing gas in this area have been reported to have thicknesses down to 2 m (Bünz et al., 2005).

The Shot-line length in case 3 is chosen to be 5 km, instead of 3 km in case 2. An increase in shot-line length will give a wider incident angle range. If only the higher incident-angle range is used, the volume coverage in the PSDM filter would decrease, resulting in poorer resolution (Lecomte, 2006). However, in this case the angle-range covers all possible illumination vectors, posing no resolution issues for the increased shot-line length.

The sampling interval will have a great impact on the seismic resolution. The geological model for case 3, have multiple dipping horizons and more complex interfaces. In order to create smooth reflectors, a sampling of 1 m in horizontal and vertical direction have been chosen. This sampling interval is very small, compared to real seismic sampling, but higher sampling will distort the seismic image, making it difficult to interpret. The small sampling interval is chosen due to the illumination effect on the input geological model.

For the analytic PSDM simulator, most of the parameters used in the local-target simulator are the same. The PSDM filter chosen, is the max reflector dip at 45°. The average background velocity is 1.75 km/s, and corresponds well with the parameters in the target. The incident angle range covers angles from 0-30 °. For both simulators a frequency of 40 Hz and 85 Hz is chosen, to investigate tuning thickness issues associated with thin gas and gas hydrate saturated layers. Gas hydrate saturation is chosen in order to match the reported saturation (5-20%) at this area (Bünz and Mienert, 2004; Bünz et al., 2005). For the free gas bearing sediments, constant and sampled values for the P-wave velocity are assigned. S-velocity and density are assumed not to change, due to the fact that gas hydrate distribution occurs away from grain contact, and act as an inclusion in the pore-fluids (Bünz et al., 2005).

Chapter 5

Modelling Results

This chapter will display the results for the rock physics and the seismic modelling. The first section will show the results from the rock physics modelling, which is implemented as acoustic properties in the seismic modelling. Whereas the seismic modelling will display three different cases as defined in Chapter 4. Case 1 display the BSR as wiggle traces, Case 2 shows a more sophisticated BSR model, while case 3 compare synthetic with real seismic data. The last section will show the resolution for 40 Hz and 85 Hz wavelets used in the seismic modelling, including the PSDM filter and the PSF.

5.1 Rock physics models

Johansen et al. (2003) proposed a model, where water and ice are mixed by the use of SCA modelling. Water have no shear strength, compared to gas hydrates or ice, which will result in a critical saturation for the mixture. At the critical saturation offset, the fluid mixture will transcend from being a fluid to a solid, and will gain shear strength. When the mixture behaves as a fluid ($\mu < 0$), the saturated sediments can be calculated using Gassmann. When the mixture behaves as a solid ($\mu > 0$), the saturated sediments are calculated by using the previously explained CCT/SCA model. Gas hydrates form from a mixture of gas and water, where gas often is the controlling constituent on hydrate formation (Rempel and Buffett, 1997). Because all of the gas probably will be used in the

gas hydrate formation process, it is sufficient to model the mixture between water and gas hydrates in this study. The mixture reach the critical gas hydrate saturation at 40%, and starts to behave like a solid. The results are similar to those obtained by Yun et al. (2005), and Johansen et al. (2003) for pure ice.

In Figure 5.1 structure 1 hydrate, consists of methane that has its origin from biogenic sources. Structure 2 hydrate consists of propane that origins from thermogenic sources, and are observed to have lower elastic properties than structure 1. The bulk and shear modulus values used in the modelling for structure 2 hydrate, were measured on structure 2 propane hydrate (Waite et al., 2000). By using the gas hydrate/water mixture as the fluid inhabiting the pore voids, P- and S-velocities can be calculated for the saturated sediments (Figures 5.2a and 5.2b).

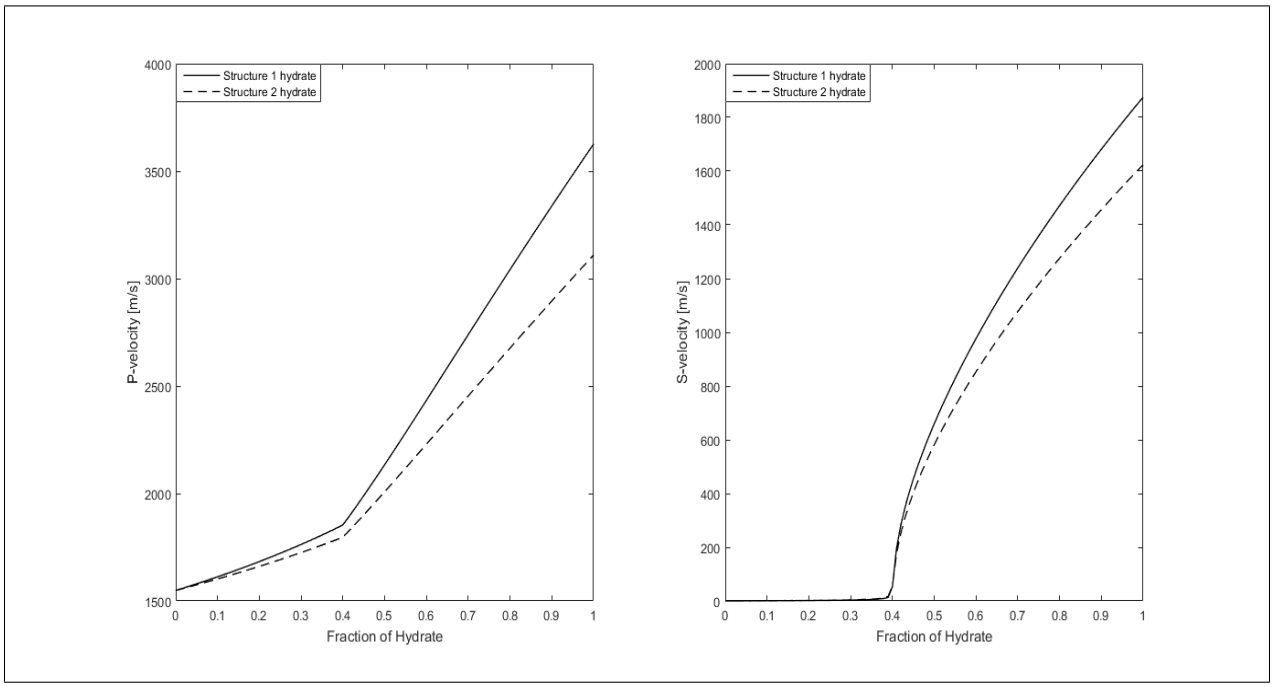

Figure 5.1: P- and S-velocity versus gas hydrate fraction. Water freezing to create structure 1 (solid line) and structure 2 hydrates (stippled line).

What can be observed in Figure 5.2a, is that cementing of grains at grain contact (scheme 1) starts when the gas hydrate concentration reach 40%. The cementing occurs rapidly, causing a steep increase in velocity. Further pore filling of gas hydrate cement, will increase the velocity gradually until 100% saturation, but much less than for the cemented

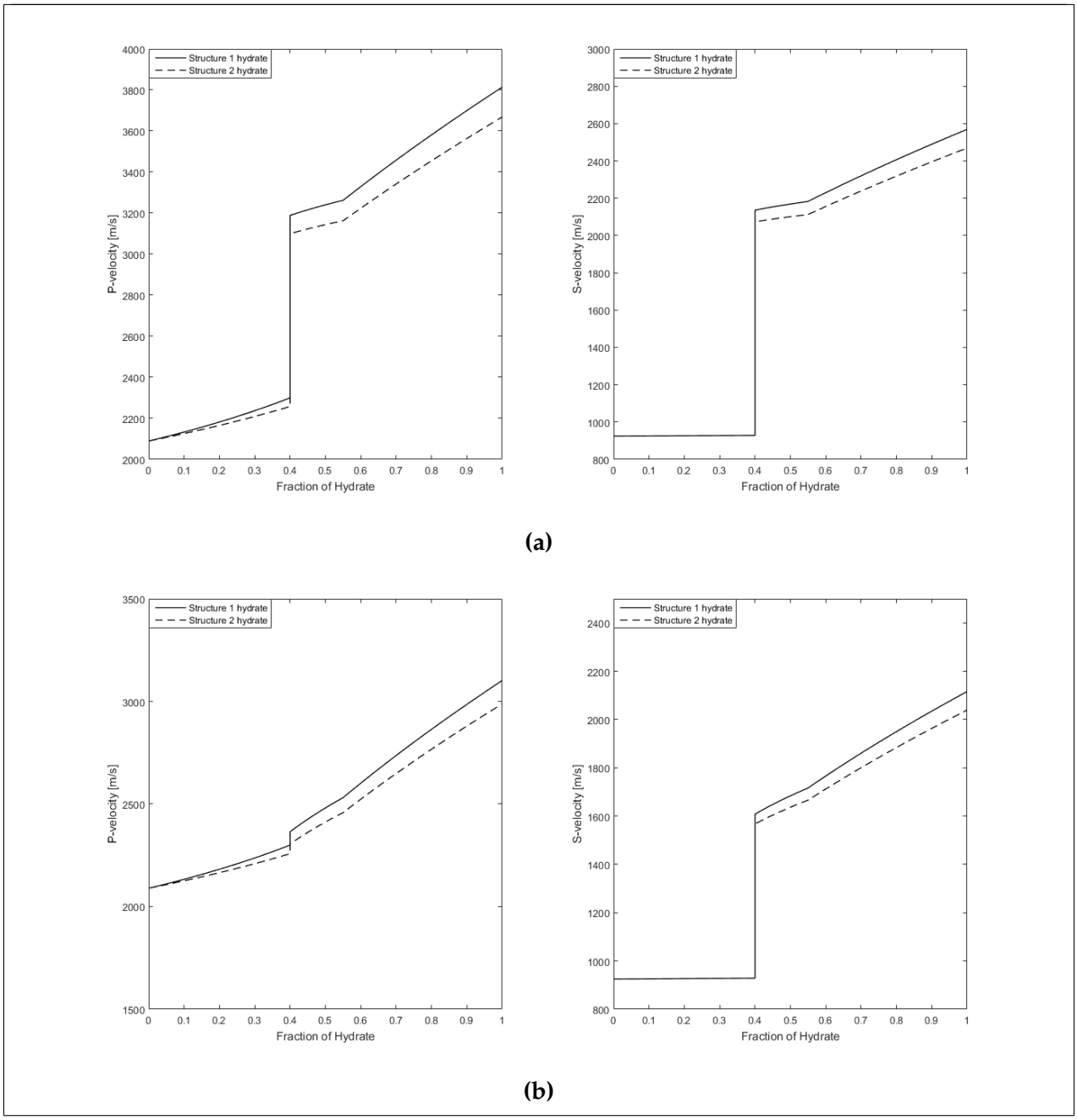

Figure 5.2: Water/hydrate mixture saturated sediments. P- and S velocity versus gas hydrate saturation for a) scheme 1, and b) scheme 2.

hydrate contribution. The S-velocity is constant up to 40% saturation, due to the fact that gas hydrates are assumed to be "floating" as a suspension in the water away from grain contact. Figure 5.2b, shows the case when gas hydrate cement is enveloping the grains (scheme 2). The hydrate cement will have a much lower effect on the sediment stiffness

in this case. The P-velocity is barely affected by the cementing at 40% saturation, but increases gradually with gas hydrate saturation.

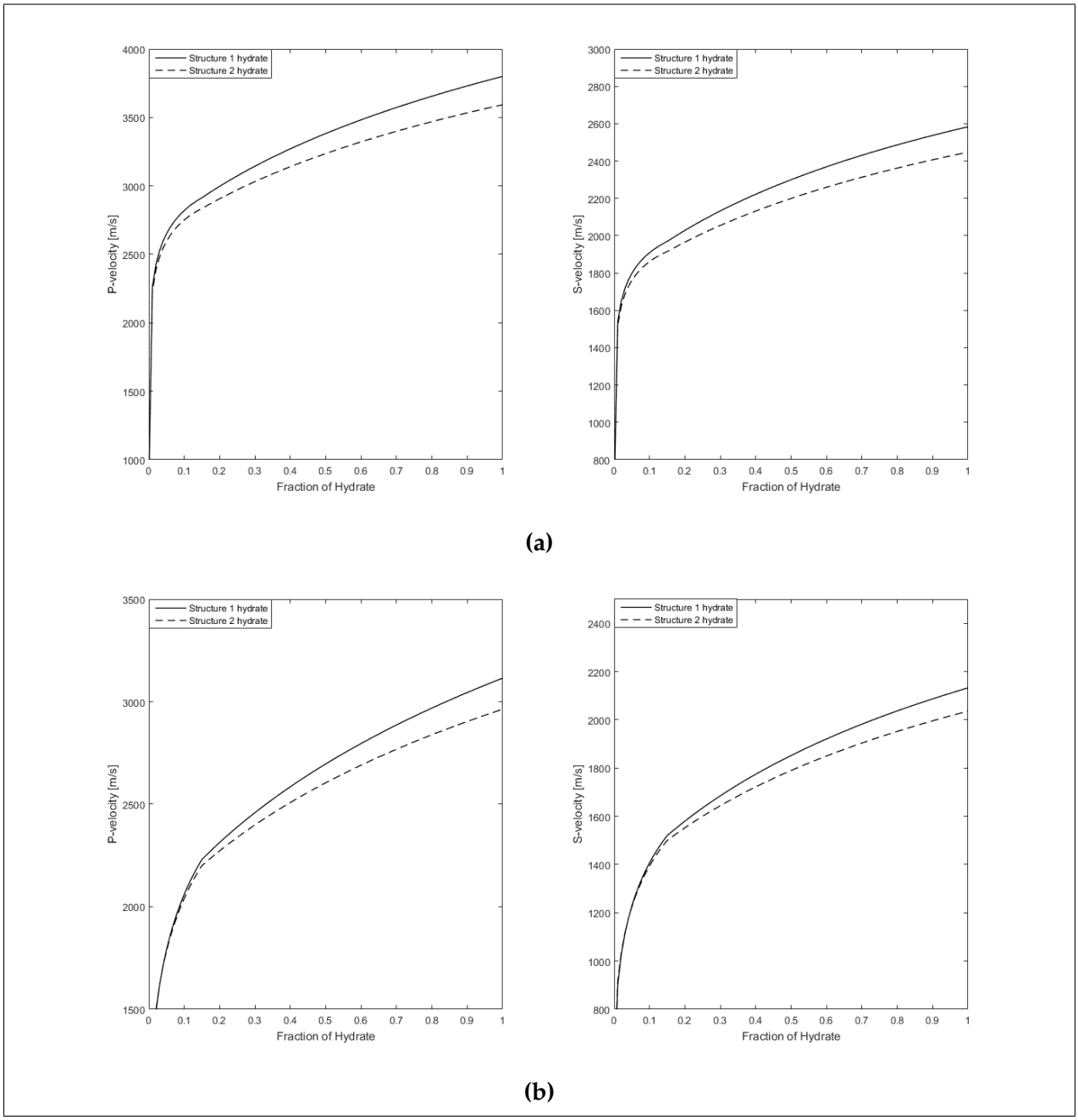

Figure 5.3: Gas hydrate and dry pores. P and S velocity versus gas hydrate saturation for a) scheme 1, and b) scheme 2.

In Figure 5.3a and 5.3b, only the gas hydrate cement effect is investigated filling dry voids. Gas hydrates are gradually included into dry pores using the CCT/SCA method. They are cementing the pores up to 15% saturation, subsequently decreasing the porosity from 40% to 34%. Additional pore-filling of gas hydrate, only results in a gradual increment until 100% saturation. Figure 5.3a shows a steeper velocity increase up to 15% gas hydrate saturation, compared to Figure 5.3b. The cement distribution around the grains will have a great impact on the velocities. Cement deposited between grain-contact points yields a higher stiffness, than cement-coating enveloping the entire grains (Dvorkin et al., 1991).

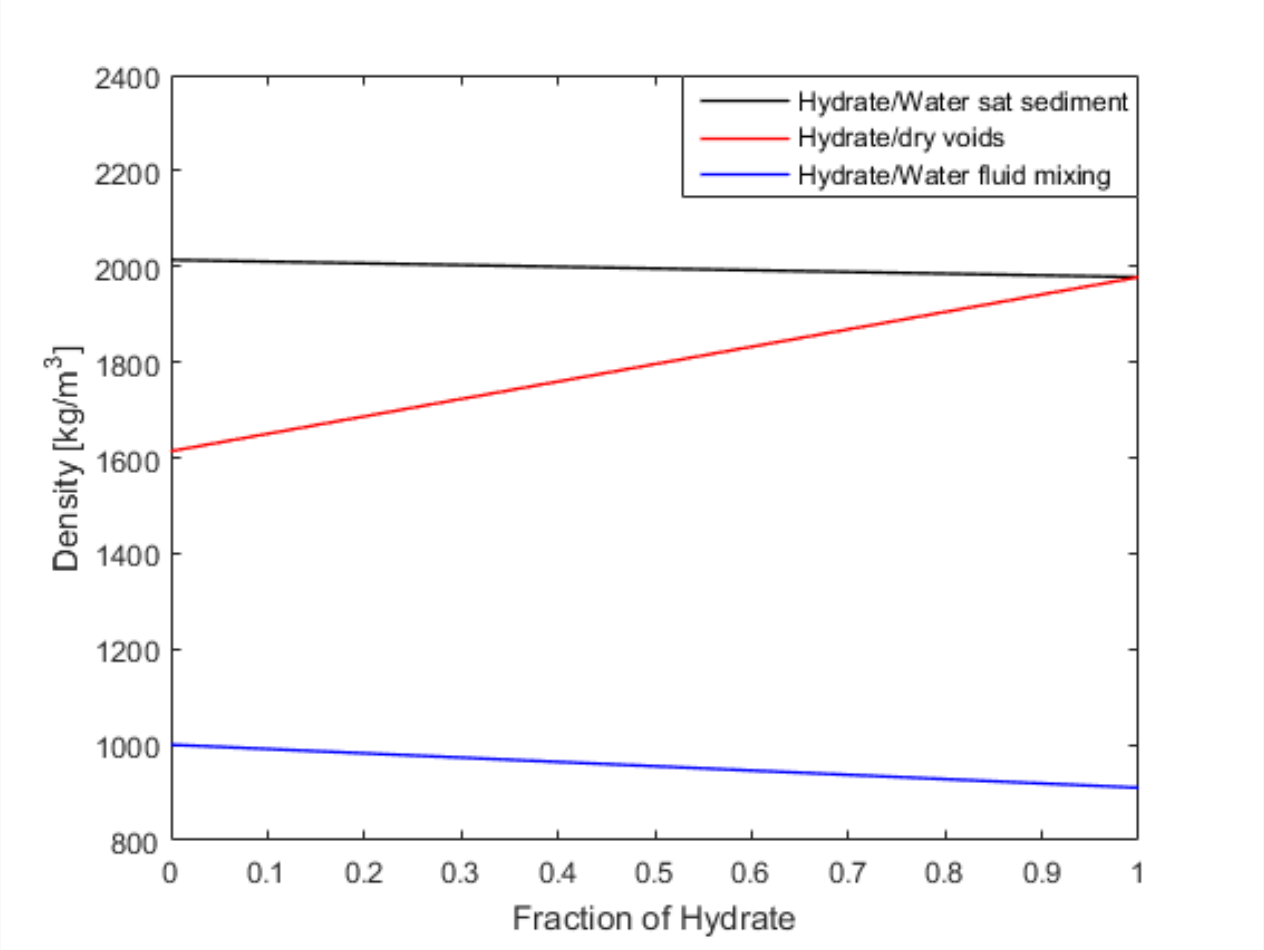

Figure 5.4: Density calculated for water/hydrate mixture (blue), water/hydrate saturated sediments (black), and hydrate/dry voids (red).

Values obtained from the rock physics models, are used in the seismic modelling, assigning properties to sedimentary layers. In addition to P- and S-velocity, density for

the hydrate saturated sediments are needed. In Figure 5.4, density for the different figures are plotted against gas hydrate saturation. Water have a higher density than gas hydrates, which results in a decrease in density for the water/hydrate mixture. For the case where gas hydrates are included into dry pores, the density will increase with saturation.

The BSR is also greatly affected by a underlying free gas layer (Bünz and Mienert, 2004). Free gas saturated sediments are calculated using Hertz-Mindlin and Gassmann's formula. The pore voids are assumed to be 100% saturated with a water/gas mixture calculated using the Reuss average equation. Critical porosity is 40%, and coordination number is chosen to be 8.2 (Dvorkin et al., 1999), (Johansen et al., 2003).

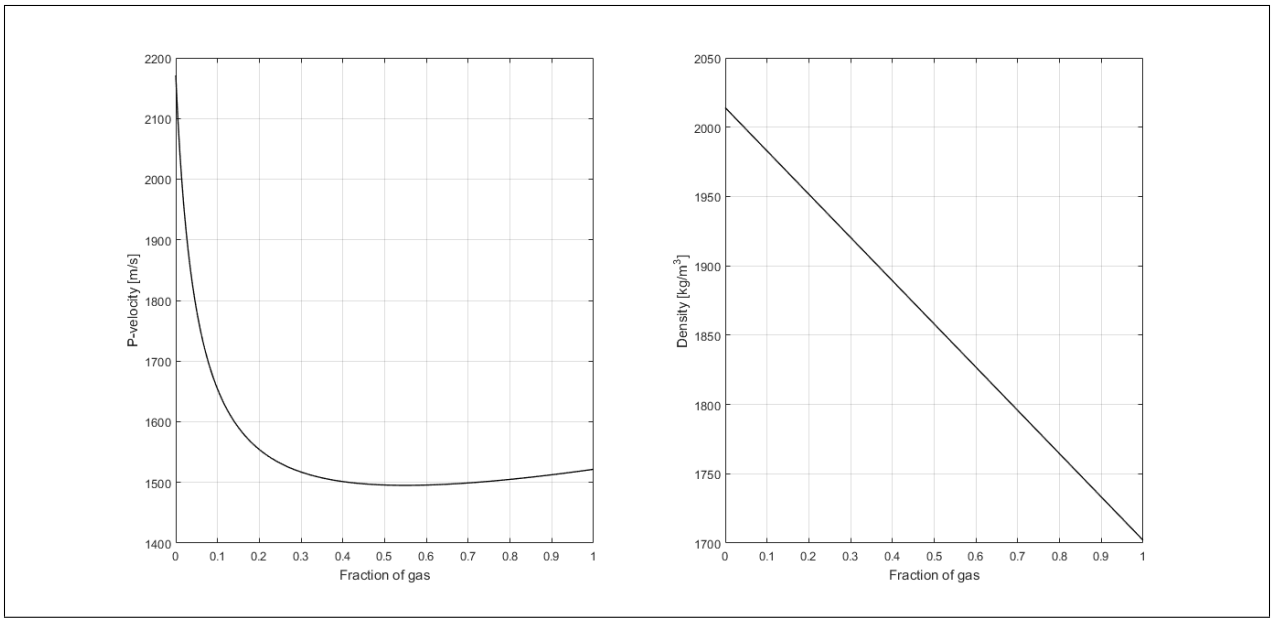

Figure 5.5: P-velocity and density versus gas saturation. Mixture of gas and water in the pore voids.

In Figure 5.5, the P-velocity experience a substantial decrease with only small amounts of gas added to the water. The density is also decreasing with increasing gas saturation. Gas and water are viscous fluids, and are assumed not to affect the shear stiffness of the sediments (Gassmann assumption). The shear modulus is therefore constant, but S-velocity is slightly increasing with gas saturation due to decreasing density.

For the seismic modelling of case 1 and 2, values for the gas and water saturated sediments are obtained from Figure 5.5 and 5.6. Figure 5.6, shows P-, S-velocity and density for three layers with different properties. From Table 4.3, layer 3 and 4 corresponds to layer 2 and 3 in Figure 5.6 respectively. Layer 2 in Figure 5.6 corresponds to the same layer with similar properties as modeled in Figure 5.5. What can be observed in Figure 5.6, is that a decrease in coordination number, and increase in porosity results in a lower P-S velocity and density. Looser sediments closer to the sea-floor should be expected to have a low number of contact points between grains, and a higher porosity (Dvorkin and Nur, 2002).

Values obtained from Figures 5.2a and 5.2b, are used in the seismic modelling and listed in Table 5.1. Hydrate structure 2 is observed in Table 5.1 to have lower velocity values than structure 1, which might be due to the orientation of the structured cages. The composition of gas situated in the cavities and other conditions would affect the bulk and shear modulus measured in laboratories, which makes the result difficult to interpret precisely. However, structure 1 and 2 are believed to have different properties, and the results highlights the potential velocity contrasts that can be encountered for the two cases. What can also be observed is that the P- and S-velocity is much higher for scheme 1 than scheme 2 above the critical saturation of 40%. This result is directly related to the difference in stiffness for the two cases, as discussed by Dvorkin et al. (1999).

Table 5.1: Parameters used for modelling Gas Hydrate distributions

Scheme 1*							
Hydrate Structure 1				**Hydrate Structure 2**			
Saturation	V_p [km/s]	V_s [km/s]	ρ [g/cm^3]	**Saturation**	V_p [km/s]	V_s [km/s]	ρ [g/cm^3]
0 %	2.09	0.92	2.01	**0 %**	2.09	0.92	2.01
25 %	2.21	0.93	2.00	**25 %**	2.19	0.93	2.00
75 %	3.52	2.36	1.99	**75 %**	3.4	2.28	1.99
100%	3.81	2.57	1.98	**100%**	3.67	2.47	1.98
Scheme 2**							
75 %	2.82	1.92	1.99	**75 %**	2.73	1.86	1.99
100%	3.12	2.13	1.98	**100%**	3.00	2.05	1.98

* Table parameters are calculated using gas hydrate scheme 1), hydrate cementing at grain contact.
** Table parameters are calculated using gas hydrate scheme 2), hydrate cement coating grains
*** Hydrate saturations of 0% and 25% are the same for scheme 1 and 2.

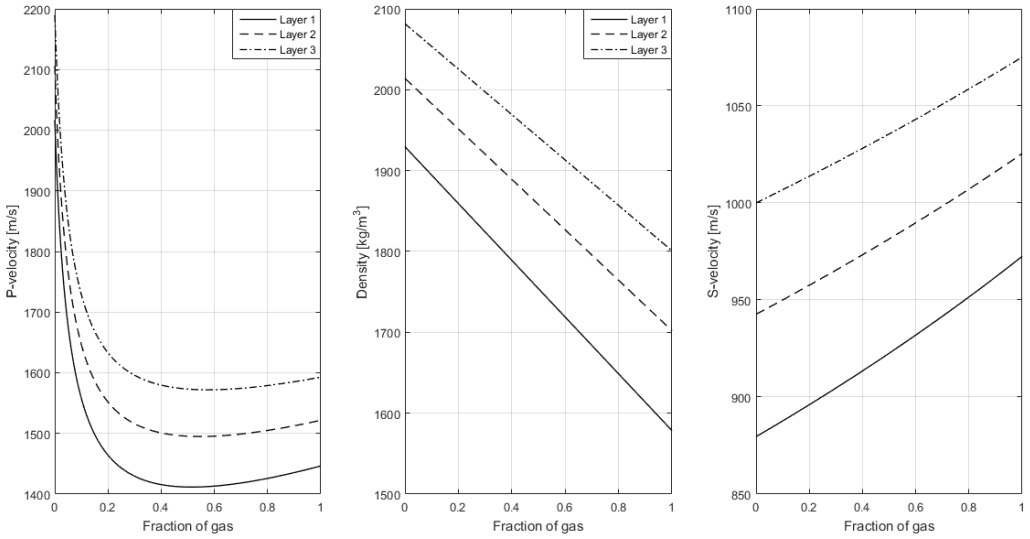

Figure 5.6: Gas/water saturated sediments for layers used in the seismic modelling of case 1 and 2.

5.2 BSR study

For case 1, an analytic PSDM filter is used, in order to display individual traces of the seismic image. Results are obtained for gas hydrate saturated sediments with underlying sediments saturated with either 50% gas/brine, or 100% brine. Gas hydrate saturations are chosen to be 25%, and 100% for scheme 1 and 2.

The bottom simulating reflector (BSR) is defined as the acoustic impedance contrast between gas hydrate saturated sediments, and sediments beneath (Berndt et al., 2004). The BSR have a negative acoustic impedance contrast compared to the sea-floor, and is expected to vary in amplitude strength depending on gas and gas hydrate saturation. When the underlying sediments are saturated with some amount of gas, the bottom of the gas layer will show an elevated positive acoustic impedance contrast (Berndt et al., 2004).

Table 5.2: Figure list case 1

Figure	Gas hydrates	Remark
Figure 5.7a	100% Scheme 1	Underlying brine saturated sediments
Figure 5.7b	100% Scheme 1	Underlying 50% gas/brine saturated sediments
Figure 5.8a	100% Scheme 2	Underlying brine saturated sediments
Figure 5.8b	100% Scheme 2	Underlying 50% gas/brine saturated sediments
Figure 5.9a	25%	Underlying brine saturated sediments
Figure 5.9b	25%	Underlying 50% gas/brine saturated sediments
Figure 5.10a	0%	Underlying 50% gas/brine saturated sediments
Figure 5.10b		Difference model between Figure 5.7b and 5.10a

In Table 5.2, the figure compositions are listed, in order to give a better outline of the results. From the rock physics modelling, the critical hydrate saturation for cementing of grains happens at 40%. 25% gas hydrate saturation will have a much lower acoustic impedance than gas hydrate saturations above 40%. Sediments saturated with gas will have a great impact on the acoustic impedance due to its low velocity, as proposed by Bünz et al. (2005).

The results for case 1 is obtained by using a 40 Hz wavelet in the 2D convolution procedure. In Figure 5.7a, 100% gas hydrate saturated sediments are overlying a 100% brine saturated sediment. When gas hydrate cement is deposited at grain contact, the stiffness of the sediments immediately increases, resulting in a very high P and S velocity. Subsequently, the acoustic impedance will be high for the gas hydrate layer. However, acoustic impedance is the product of both density and P-velocity. The density for the gas hydrate layer is lower than for the brine saturated sediments. It can be observed in Figure 5.7a, that the BSR and the top of hydrate have more or less the same strength in amplitude. In Figure 5.7b, sediments beneath the gas hydrate layer contain 50% gas and 50% brine. The acoustic impedance contrast observed for the BSR in this case is much greater than that of Figure 5.7a. The difference is due to the gas effect, which enhance the negative amplitude of the BSR reflection and creates a visible positive reflector at the base of the gas layer.

In figure 5.8a, 100% gas hydrate saturated sediments are overlying a 100% brine saturated layer. The hydrate cement is enveloping the grains (scheme 2), causing a lower P and

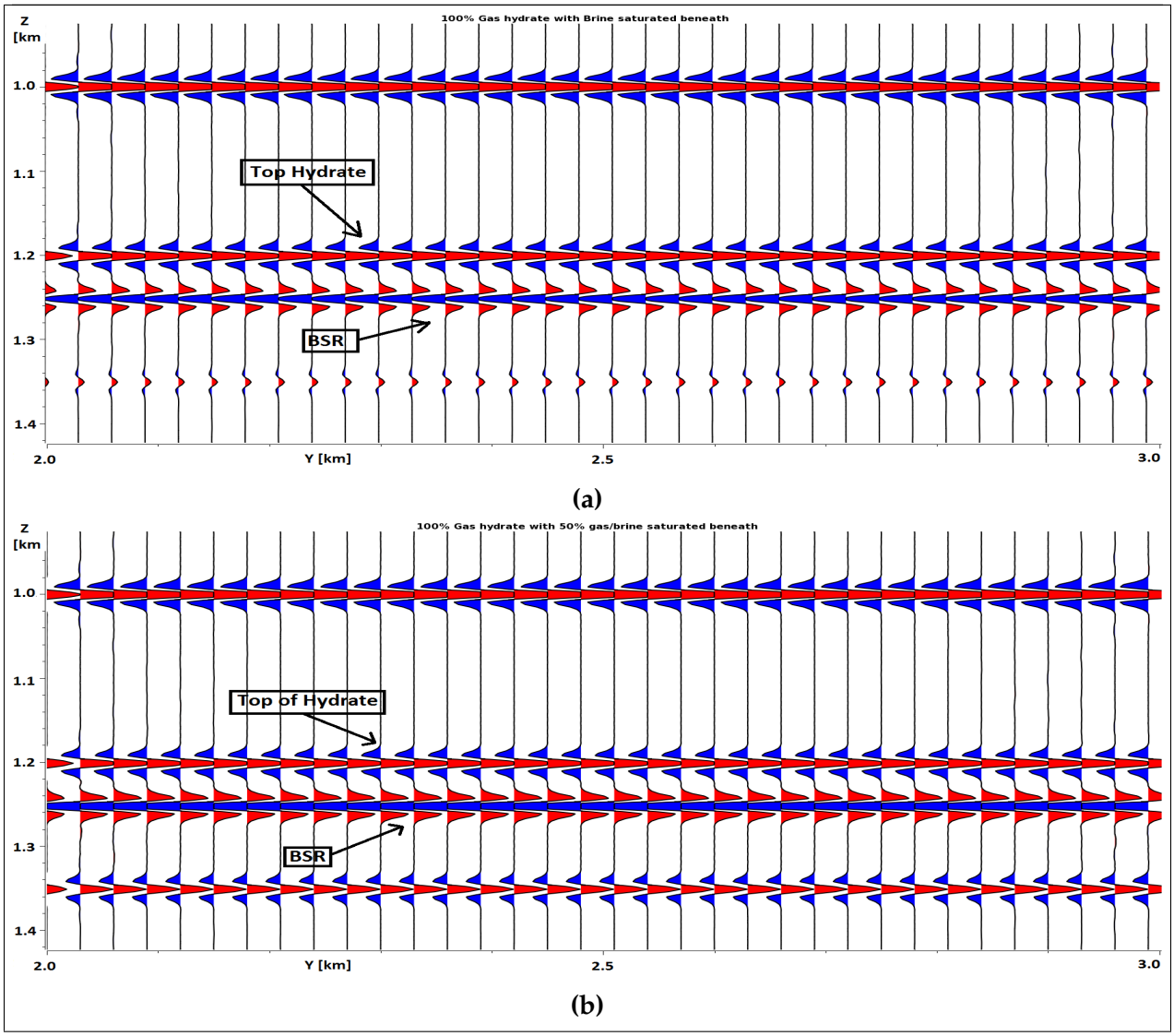

Figure 5.7: Wiggle trace of a) Model 2 and b) Model 4 from Table 4.2. a) Showing seismic traces of 100% Gas hydrate cemented sediments with an underlying brine saturated sediment. b) Showing seismic traces of 100% Gas Hydrate cemented sediments, with 50% gas/brine saturated sediments beneath. Both figures are for gas hydrate cemented at grain-contact (Scheme 1).

S velocity than for scheme 1. The same realization that the low velocity free gas layer enhances the negative amplitude of the BSR, can be observed in Figure 5.8b. The acoustic impedance contrast observed for scheme 2, results in a weaker amplitude, but still enough to create a strong reflection. For the case of non-cemented gas hydrates away from grain contact, the stiffness of the sediments are not affected by the gas hydrate saturation. A small increase in the amplitude is observed for 25% gas hydrate saturation compared to

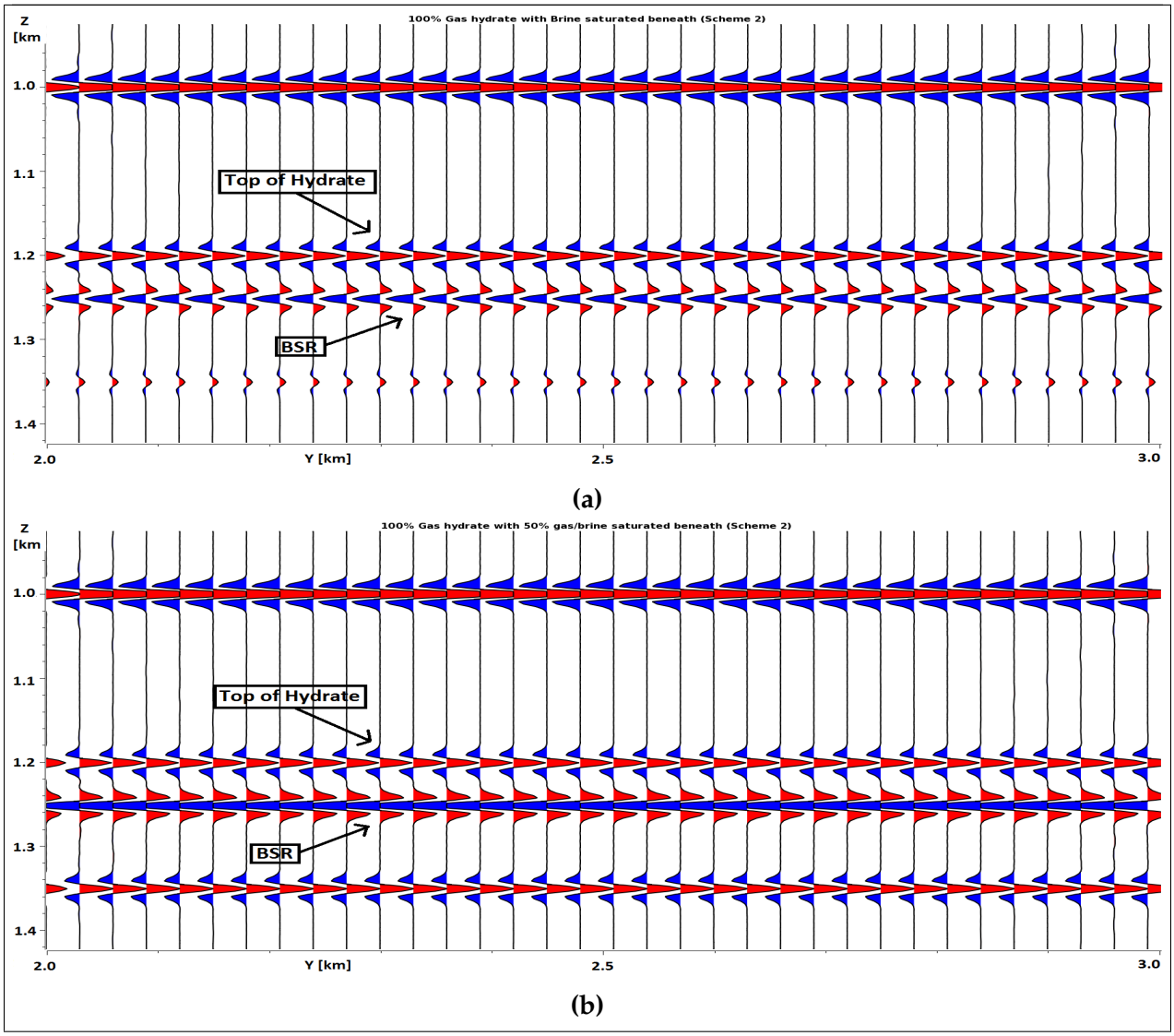

Figure 5.8: Wiggle trace of a) Model 6 and b) Model 7 from Table 4.2. a) Showing seismic traces of 100% gas hydrate cemented sediments with an underlying brine saturated sediment. b) Showing seismic traces of 100% Gas Hydrate cemented sediments, with 50% gas/brine saturated sediments beneath. Both figures are for gas hydrate cement coating the grains (Scheme 2).

pure brine saturated sediments in Figure 5.9a. However, for Figure 5.9b the free gas/brine saturated sediments cause a significant increase in the negative BSR amplitude. For small gas hydrate saturations, free gas effect have a great impact on the seismic reflection (Bünz et al., 2005). Figure 5.10a shows a case with a brine-saturated layer overlying a gas/brine saturated sediment. The BSR reflection is observed to have a sharp negative amplitude, only due to the free gas saturation. Figure 5.10a suggests that even small amounts of

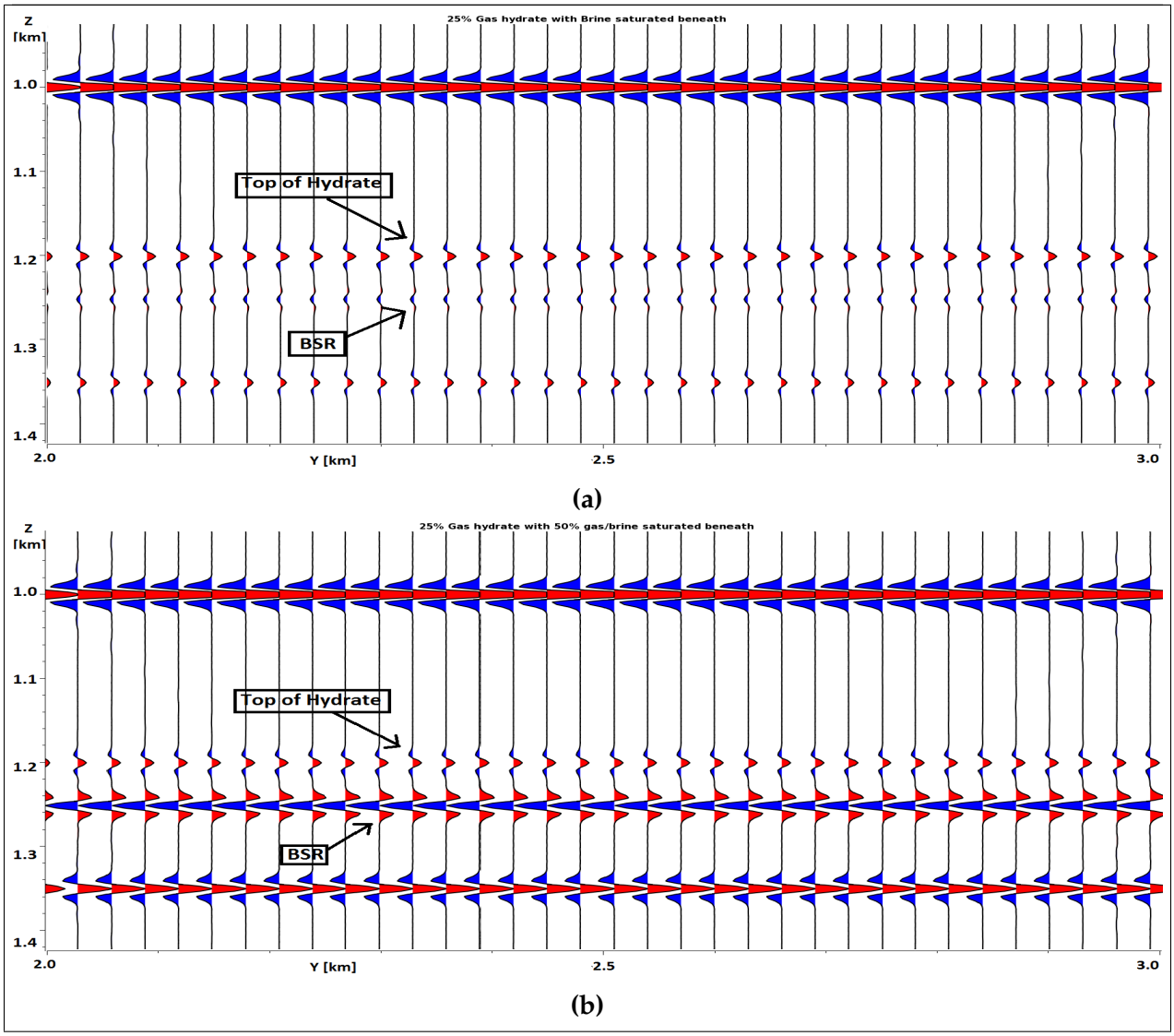

Figure 5.9: Wiggle trace of a) Model 1 and b) Model 3 from Table 4.2. a) Showing seismic traces of 25% gas hydrate saturated sediments with an underlying brine saturated sediment. b) Showing seismic traces of 25% Gas Hydrate saturated sediments, with 50% gas/brine saturated sediments beneath. Both figures are for gas hydrate inclusions away from grain contact.

hydrates suspended in brine, would have little or no effect on the BSR when free gas are present in the layer beneath.

In order to observe the difference between no gas hydrate, and 100% gas hydrate saturated sediments, overlying a 50% gas/brine saturated sediment, a difference map are displayed. The traces in Figure 5.10b correspond to the difference in the top of hydrate and BSR interface, between Figures 5.7b and 5.10a. Even though gas is present beneath the

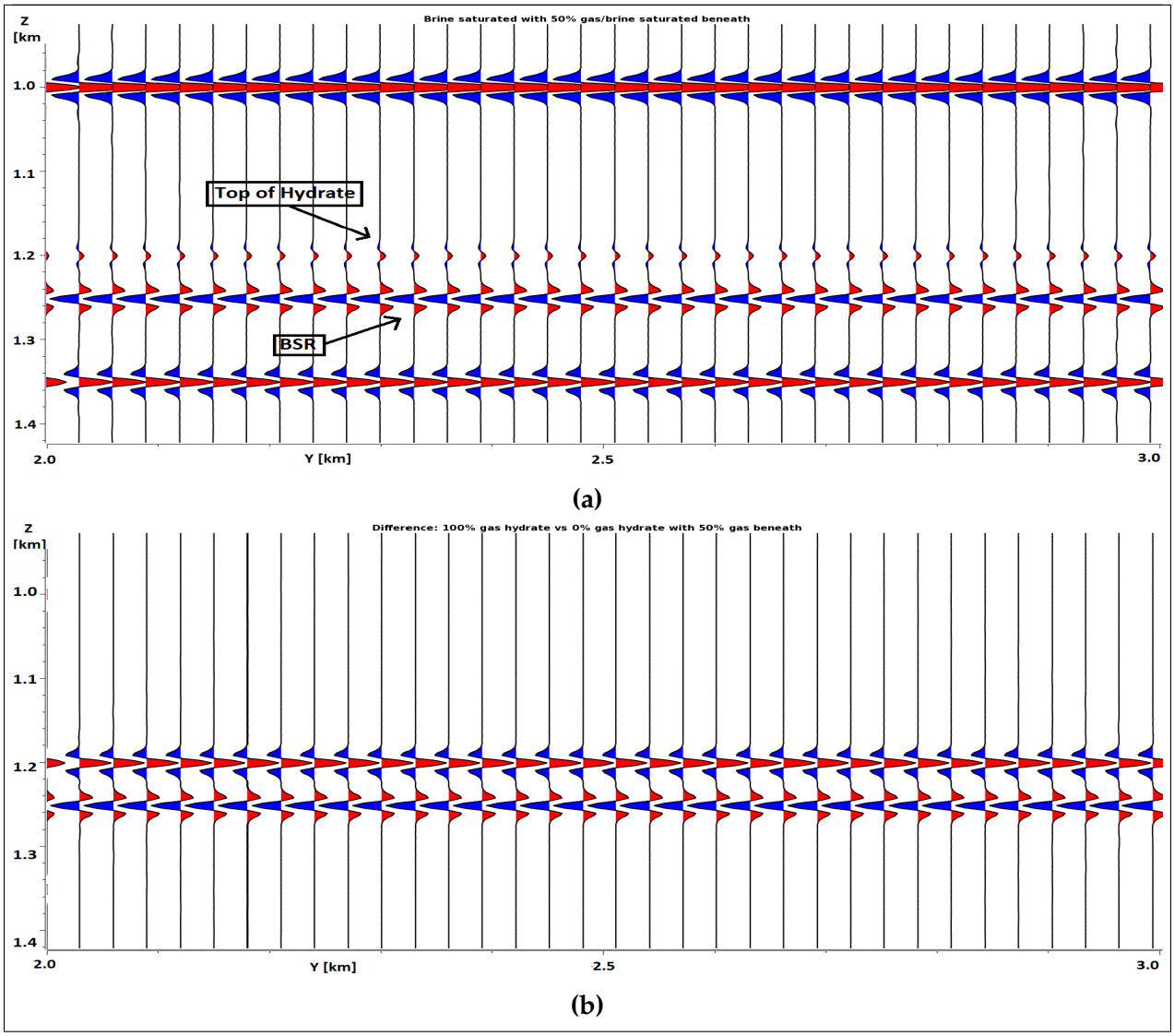

Figure 5.10: Wiggle trace of a) Model 5 ,and b) a difference map between model 4 and 5 from Table 4.2. a) Showing seismic traces of brine saturated sediments with an underlying 50% gas/brine saturated sediment. b) Showing the difference between 0% gas Hydrate, and 100% cemented Gas Hydrate (Scheme 1).

base of the gas hydrate stability zone (BGHZ), the effect of 100% gas hydrate saturating and cementing pore voids, have a clear impact on the top of hydrate and BSR reflection. The results obtained for case 1, are similar to those obtained by Ecker et al. (1998), where AVO responses for the BSR was investigated. Case 1 is not suitable to evaluate AVO, because the incident angle is zero and no source-receiver pairs have been chosen for the analytic PSDM simulator (Gelius and Johansen, 2010).

5.3 Gas hydrate saturation study

For case 2 the aim is to investigate the effect of gas hydrate saturation with an underlying free gas saturated sediment, on the BSR reflection strength. In Table 5.3, the figure compositions for case 2 are listed. The gas layers in the model contain 10% gas and 90% brine, with 100% brine saturated layers in between.

Table 5.3: Figure list case 2

Figure	Gas hydrate saturation	Remark
Figure 5.12	25%	10% gas, 90% water saturated sediments
Figure 5.13	75% Scheme 1	10% gas, 90% water saturated sediments
Figure 5.14	75% Scheme 2	10% gas, 90% water saturated sediments
Figure 5.15	100% Scheme 1	10% gas, 90% water saturated sediments
Figure 5.16	100% Scheme 2	10% gas, 90% water saturated sediments

The BSR is cross-cutting the sediments with an angle, as observed in Figure 5.11. Gas hydrate saturated sediments is confined to a certain area, by using a sampled function tool in the horizontal direction. Sampled functions for V_p, V_s and ρ are created, but only the sampled function for V_p is shown. Sampled functions and property models for V_s and ρ can be found in Appendix A. The sampled function for V_p in Figure 5.11, is similar to the rock physics model in Figure 5.2a. It is assumed here that the BSR marks the base of the gas hydrate stability zone, with gas hydrate present in small concentrations except for the gas hydrate reservoir marked in Figure 5.11. Gas hydrates are assumed to clog the pathways, leaving gas trapped beneath the BSR (Ecker et al., 1998). Assuming a local good deposition environment for gas hydrates and sufficient gas/water influx at the hydrate reservoir (Figure 5.11), conditions for cemented hydrate growth are created. The assigned properties for the different layers are found in Table 5.1.

In Figure 5.12, 25% gas hydrate saturation are found in the reservoir. The layers with 10% gas creates large negative and positive reflections with the brine-saturated sediments in between. The velocity contrast for the gas hydrate saturated sediments are not great enough to create a continuous reflection where gas is not present. The free gas effect on

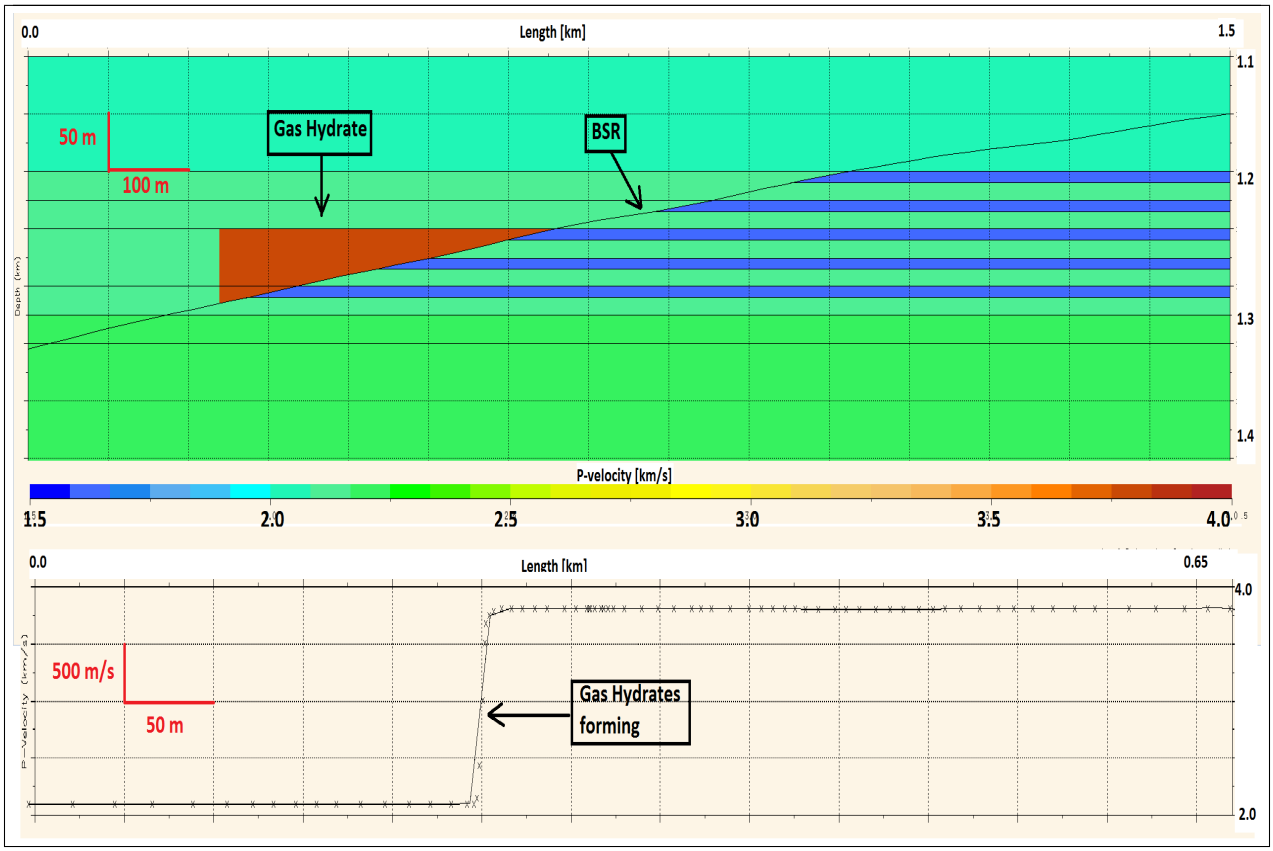

Figure 5.11: P-velocity assigned to the geological model, with the sampled function assigned to the gas hydrate saturated layers. Model is for 100% gas hydrate saturation (scheme 1).

the reflection amplitudes are so large, that the gas hydrate contribution vanishes. What can also be observed, is that the enhanced reflections terminate at the BSR in a similar manner observed at the southern Vøring plateau (Figure 4.7).

In Figure 5.13, 75% gas hydrate is present in the pore space of the reservoir zone. The gas hydrate is cementing at grain contact (scheme 1), creating a high velocity zone where the gas hydrates are present. The negative amplitude (sharp blue) observed at the BSR, arises from the velocity contrast. BSR reflection is continuous, with a sharper negative reflection where the gas hydrate and free gas layer intersects. When the gas hydrate cement is enveloping grains evenly, the stiffness of the sediments are lowered compared to gas hydrate cement at grain contact (Dvorkin et al., 1999). In Figure 5.14, the continuous BSR reflection is not clearly visible anymore, showing some patches with lower negative

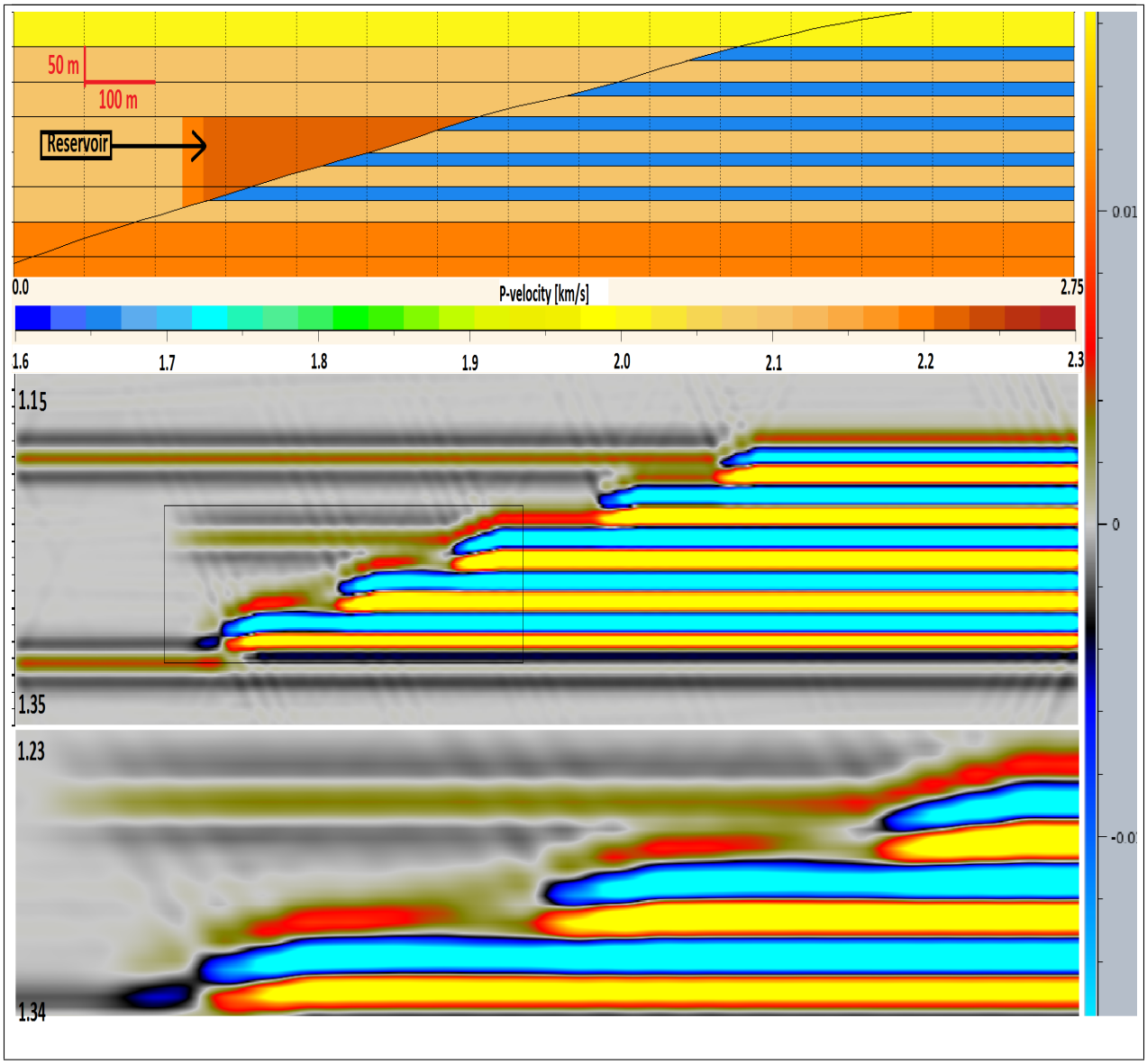

Figure 5.12: Showing the P-velocity model block and reservoir. Bottom two figures show the seismic image obtained for a gas hydrate saturation of 25%. The middle figure is 2.75 km in length, and the bottom figure is a close up from 0.2 to 0.7 km. Scale to the right is for the seismic image reflection strength.

amplitude strength. The P-wave velocity is lower than for scheme 1, and the contrast between the hydrate and brine saturated sediments are not large enough to create a proper reflection. The contrast between the gas hydrate and free gas saturated sediments can be observed to have a brighter reflection than between the brine and gas saturated sediments. In Figure 5.15, the entire pore void is saturated with gas hydrates, with some

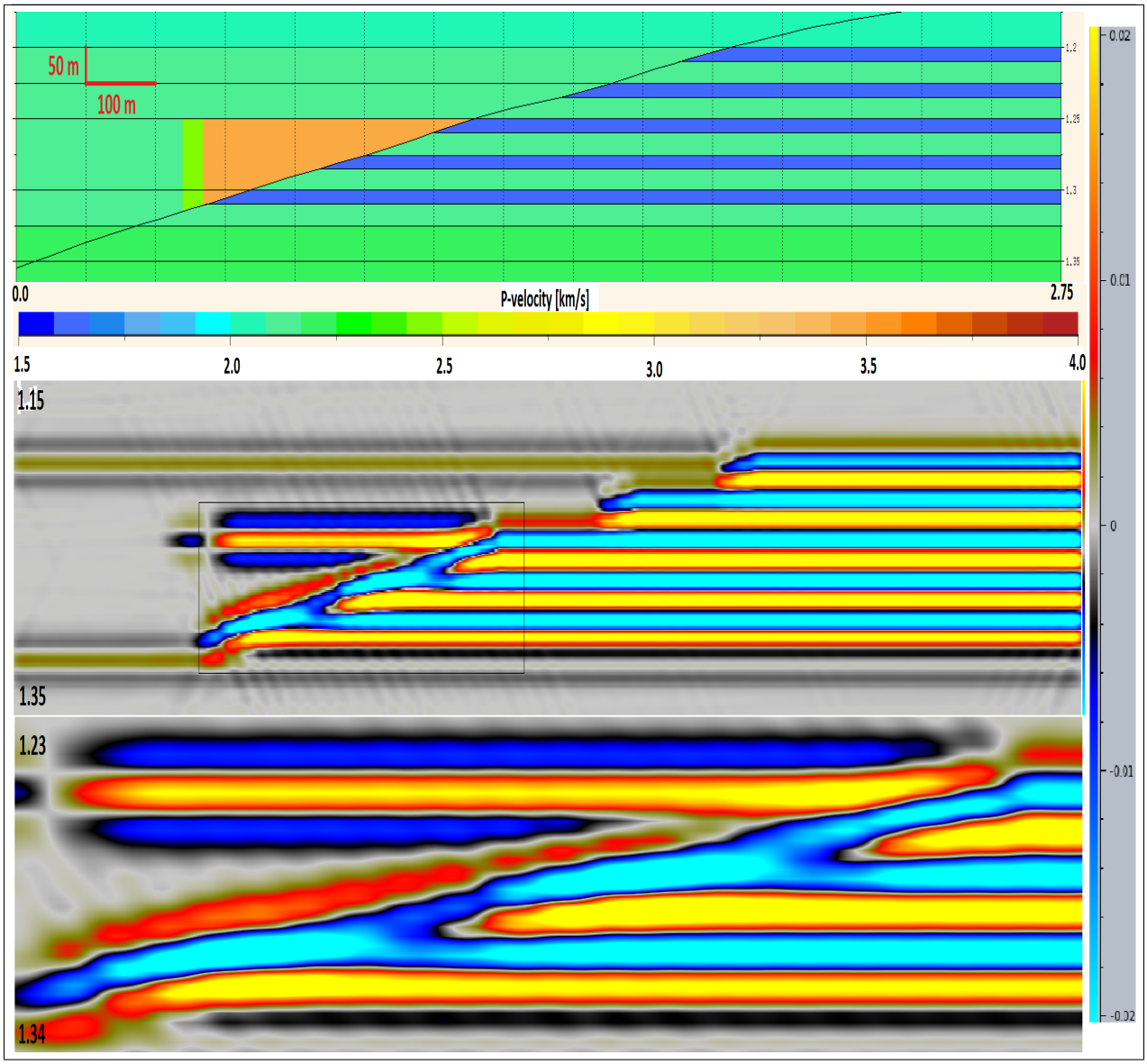

Figure 5.13: Showing the P-velocity block and the reservoir. Bottom two figures show the seismic image obtained for a Gas hydrate saturation of 75%. The figure is composed of gas hydrate cementing at grain contact (Scheme 1). The middle figure is 2.75 km in length, and the bottom figure is a close up from 0.2 to 0.7 km. Scale to the right is for the seismic image reflection strength.

cement at grain contact (scheme 1). The velocity contrast for 100% gas hydrate saturated sediments are very high, creating the observed clear reflection. For scheme 2, the velocity contrast is lower, resulting in a nearly discontinuous BSR reflection observed in Figure 5.16. The reason for the observed low reflections at the gas hydrate and brine saturated sediment interfaces, might be that the 100% brine saturated layers have high density and

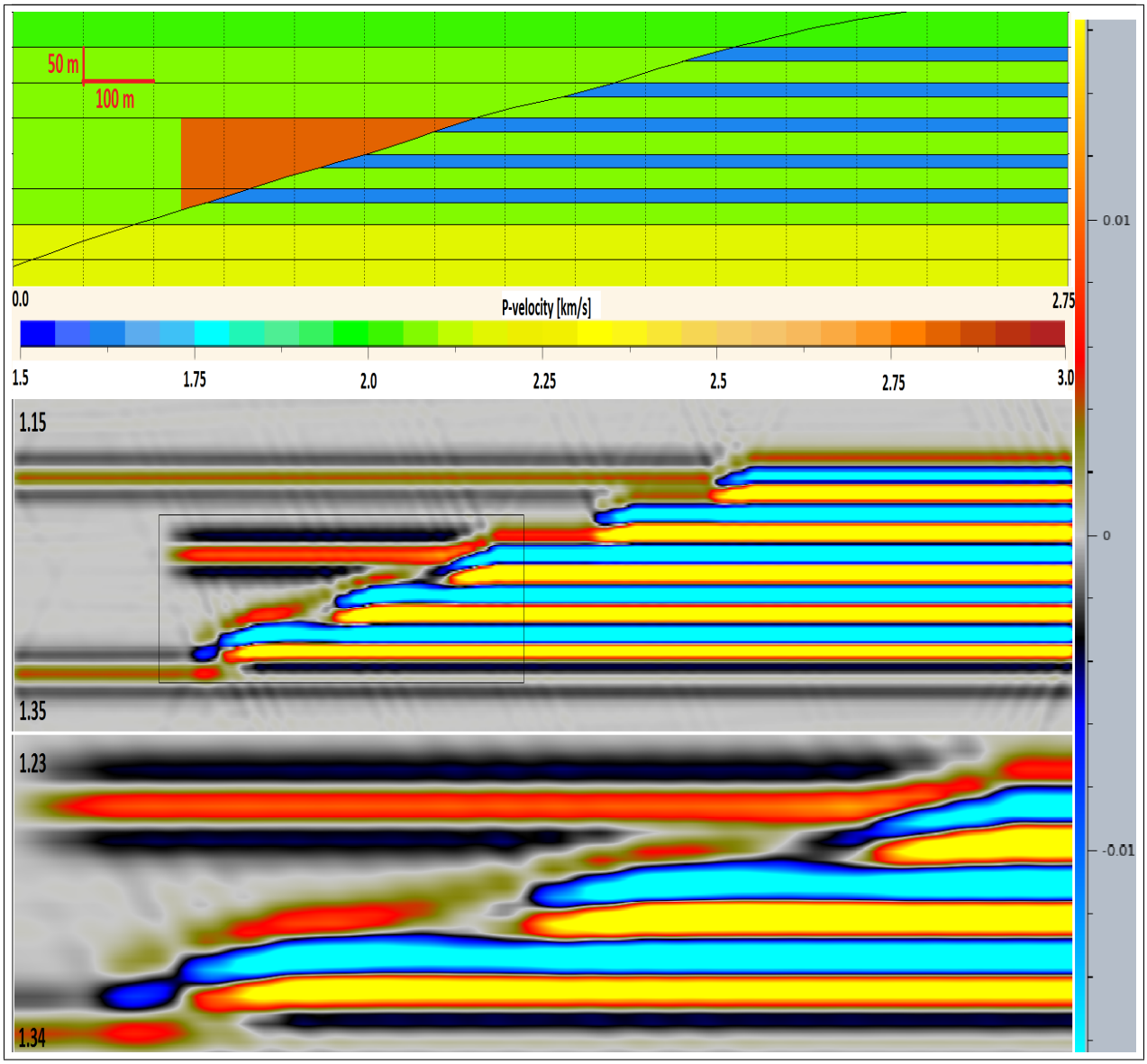

Figure 5.14: Showing the P-velocity model block and reservoir. Bottom two figures show the seismic image obtained for a gas hydrate saturation of 75%. The figure is composed of gas hydrate cement coating the grains (Scheme 2). The middle figure is 2.75 km in length, and the bottom figure is a close up from 0.2 to 0.7 km. Scale to the right is for the seismic image reflection strength.

relatively high velocity, resulting in a relatively large acoustic impedance. The impedance contrast between the gas and brine saturated layers is subsequently high, resulting in sharp positive and negative amplitudes.

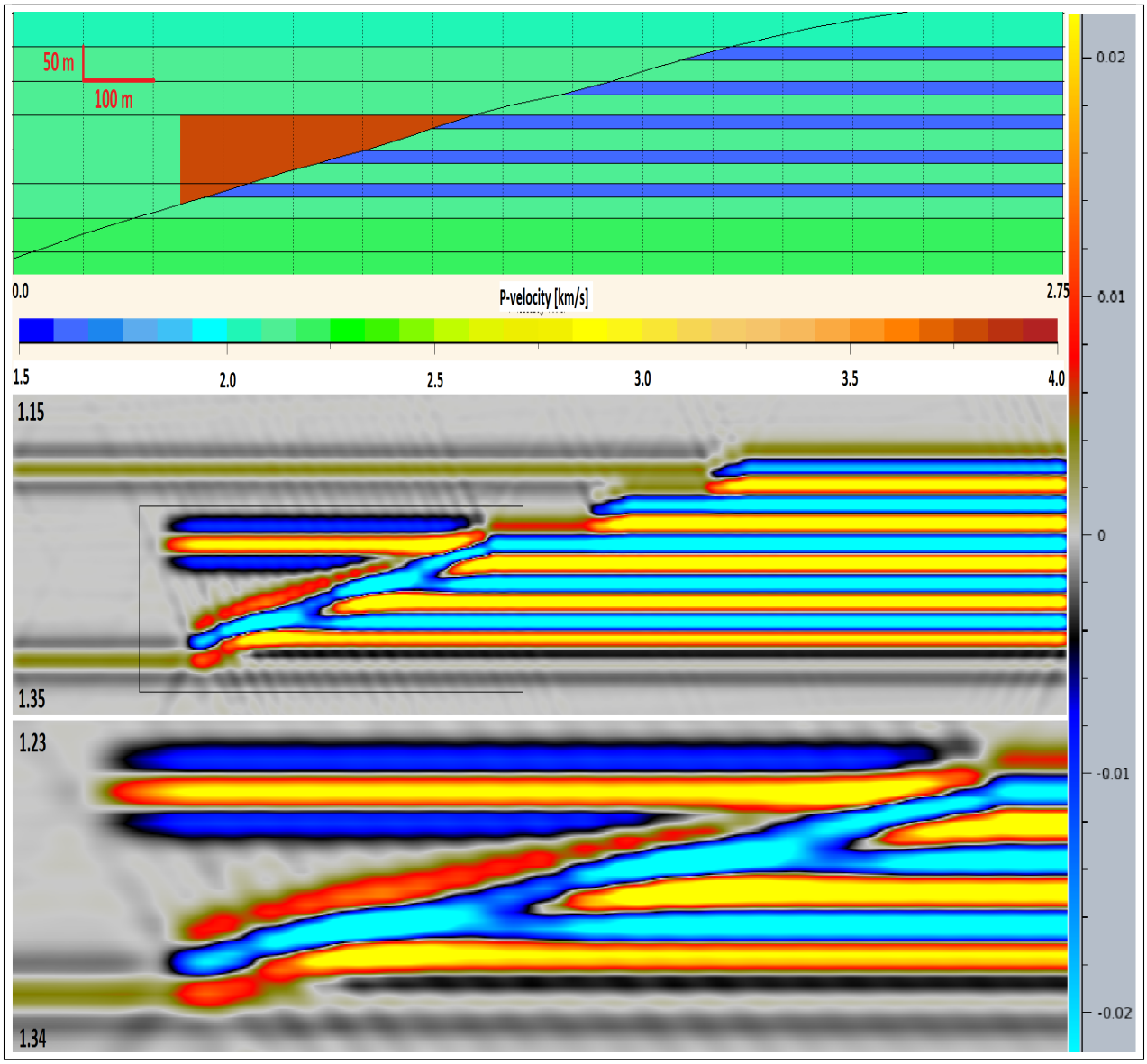

Figure 5.15: Showing the P-velocity model block and reservoir. Bottom two figures show the seismic image obtained for a gas hydrate saturation of 100%. The figure is composed of gas hydrate cementing at grain contact (Scheme 1). The middle figure is 2.75 km in length, and the bottom figure is a close up from 0.2 to 0.7 km. Scale to the right is for the seismic image reflection strength.

Although the entire pore voids have been completely saturated with gas hydrates in Figures 5.15 and 5.16, the difference in acoustic impedance where brine is present beneath, is observable for the two cases. The distribution of gas hydrate cement in between grains, will have a great impact on the BSR reflection.

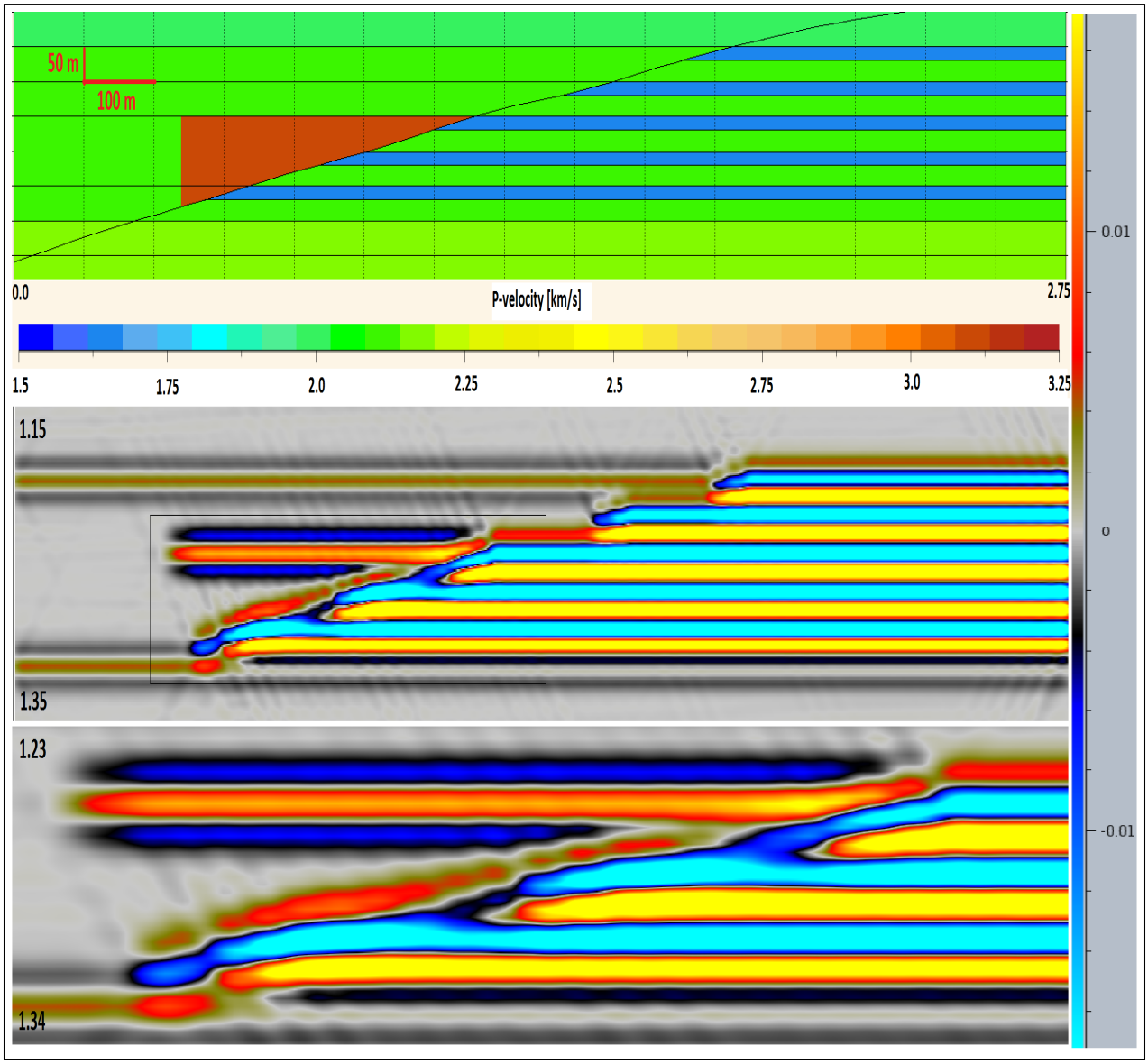

Figure 5.16: Showing the P-velocity model block and reservoir. Bottom two figures show the seismic image obtained for a gas hydrate saturation of 100%. The figure is composed of gas hydrate cement coating the grains (Scheme 2). The middle figure is 2.75 km in length, and the bottom figure is a close up from 0.2 to 0.7 km. Scale to the right is for the seismic image reflection strength.

In all figures, the top of the hydrate layer is observed as a reflector, resulting in a positive reflection with the sediment layer above. For low gas hydrate saturations, the observed reflector will vanish due to noise or other reflectors interfering. However, if the gas hydrate reservoir is sufficient in saturation and height above the BSR, a clear reflector would potentially be observed in real seismic.

Gas hydrates initiate their formation process at the BGHZ, growing in an upward direction. The hydrate formation is determined by the access to free gas and water. Usually, hydrate zones are smaller than 50 m in vertical depth, due to the the fact that already formed hydrate prevent gas and water to penetrate up (Rempel and Buffett, 1997). The gas hydrates may also dissociate at the BSR, due to increased sedimentation and changes in sea level, resulting in free gas trapped below the gas hydrate zone, initiating a recycling process of the gas (Haacke et al., 2007). The figures presented in case 2, have a local hydrate reservoir of 100 m at the max above the BSR. This distribution may be unrealistic in terms of natural in situ gas hydrate distribution. However, the reservoir allows for a study of the gas hydrate effect between free gas and brine saturated sediments.

The local-target PSDM simulator requires a survey and background model. The background model used is 1 dimensional, where an eikonal solver calculates the ray-path. Survey configuration will have an effect on the incident angle, and subsequently the illumination points. The geological model have a fairly simple geometry, and are less affected by illumination problems and the need for a large offset distribution.

Results show for all cases that the free gas layer will create a bright reflection at the BSR. The brine saturated sediments are the controlling factor on the continuous reflection, creating smaller contrasts for lower gas hydrate saturations and different distributions. The frequency might also impose a problem when illuminating the dipping BSR reflector. A 40 Hz wavelet used in this case, can create vertical resolution problems, and a too coarse sampling poses lateral resolution issues. The frequency should however be sufficient in this case, since the thickness of the layers are about 10 m.

5.4 Comparison with real seismic data

For case 3, the aim is to create a synthetic seismic section similar to the real seismic data obtained from the southern Vøring plateau. According to Bünz et al. (2005), gas hydrates at the survey area, are observed as inclusions in the pore voids, without affecting the stiffness of the sediments. For this study, only gas hydrate saturations below 40% are valid for the seismic modelling. Likely, the pore voids are not completely filled with water/gas hydrate, but rather experience a patchy saturation/distribution. By using Hills average Equation 3.4, with the completely saturated case (Equation 3.14) and dry case (Equation 3.10), it is possible to calculate elastic properties for a patchy distribution of fluids (Johansen et al., 2003). Assuming that 75% of all pores are filled with hydrate/water and 25% are dry voids, a P-velocity of 1.90 km/s is calculated. The S-velocity is assumed to be the same as the sediments, because the gas hydrate saturation behaves as a fluid, only affecting the bulk modulus of the sediments (Andreassen et al., 2003; Bünz et al., 2005). The density, is affected by the water and gas hydrate saturation, and will be higher than the surrounding sediments ($\rho = 1.80 g/cm^3$).

As can be observed in Figure 5.17, the P-velocity only varies for the three lower gas hydrate saturated layers (blocks). The gas-saturated layers are assumed to contain 50% gas and 50% brine, while the two lower gas layers varies in gas saturation horizontally. Properties assigned to the gas/brine and gas hydrate bearing sediments are listed in Table 5.4. The P-velocity and density are calculated from 25% gas hydrate saturation with 75% patchy saturation of the pore voids. In addition, it can be observed in Figure 5.17 that one horizontal layer has higher P-velocity (brown color) than surrounding sediments. This is due to a probable local lithology change in this area.

Table 5.4: Properties case 3

Layer	V_p [km/s]	V_s [km/s]	$\rho[g/cm^3]$	Saturation
Gas layer	1.50	*	*	50% gas
Gas Hydrate layer	1.90	*	1.80	25% gas hydrate

* Same property as the surrounding sediments.

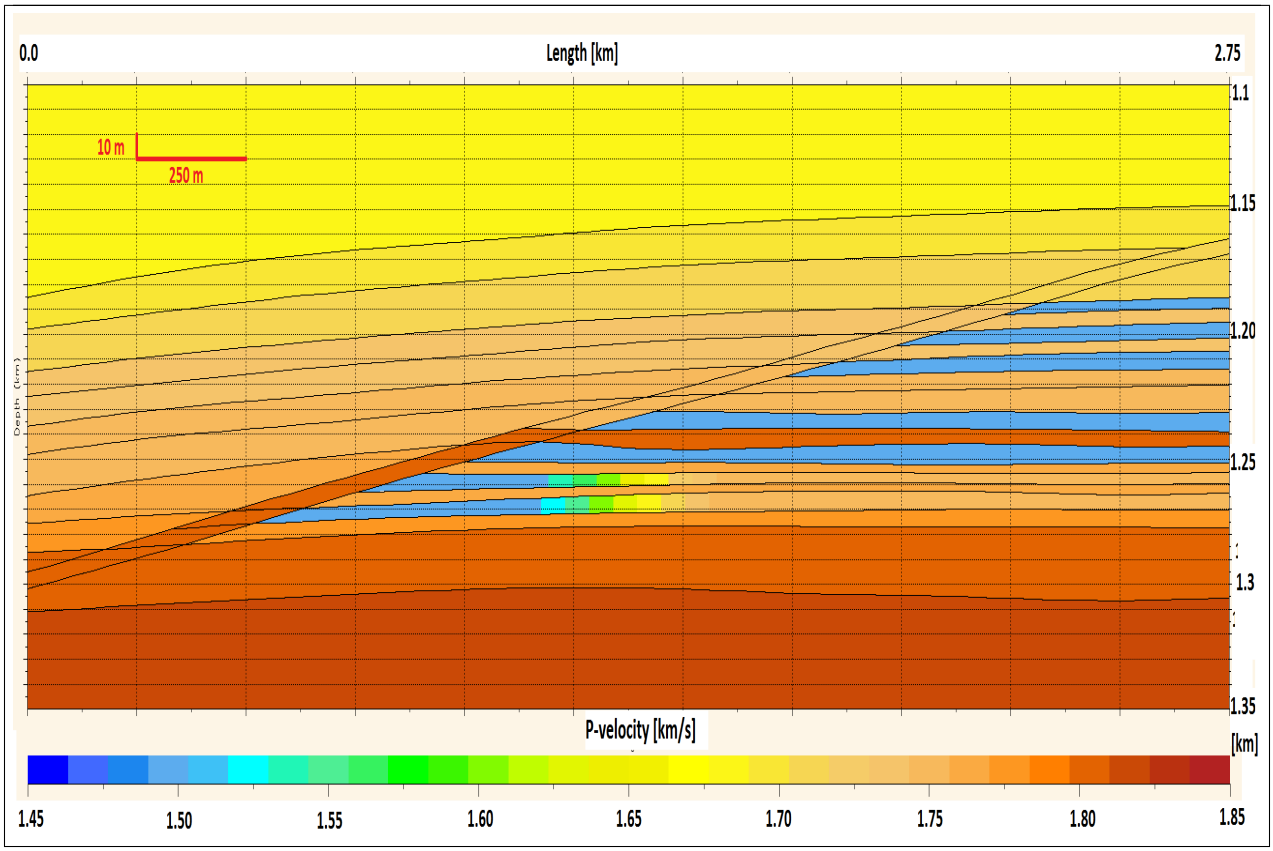

Figure 5.17: Showing the P-velocity in the 2D model-builder. The P-velocity for the gas hydrate layers are 1.90 km/s. Other values are listed in Table 4.5.

An outcrop is taken from Figure 3.2, showing a clear BSR proper in Figure 5.18 as indicated by arrows. What can be observed in the real seismic section, is that a continuous BSR proper is cross-cutting sedimentary layers and trapping free gas beneath. The termination of enhanced reflections in Figure 5.18, is probably due to a small gas hydrate saturation (1-5%) clogging pore throats, resulting in trapped gas beneath for the other parts of the BSR (Bünz et al., 2005).

Seismic modelling is performed by using both the analytical and local-target PSDM simulator. The analytic simulator is showing the entire seismic section, while the local-target simulator is centered in on the BSR proper. Bünz et al. (2005) reported that the gas-bearing sediments in the area was varying between 2-13 m in thickness, which is also the case for Figure 5.17. When dealing with thin sedimentary layers, the vertical resolution is especially important. The limiting vertical resolution is one quarter (1/4) of

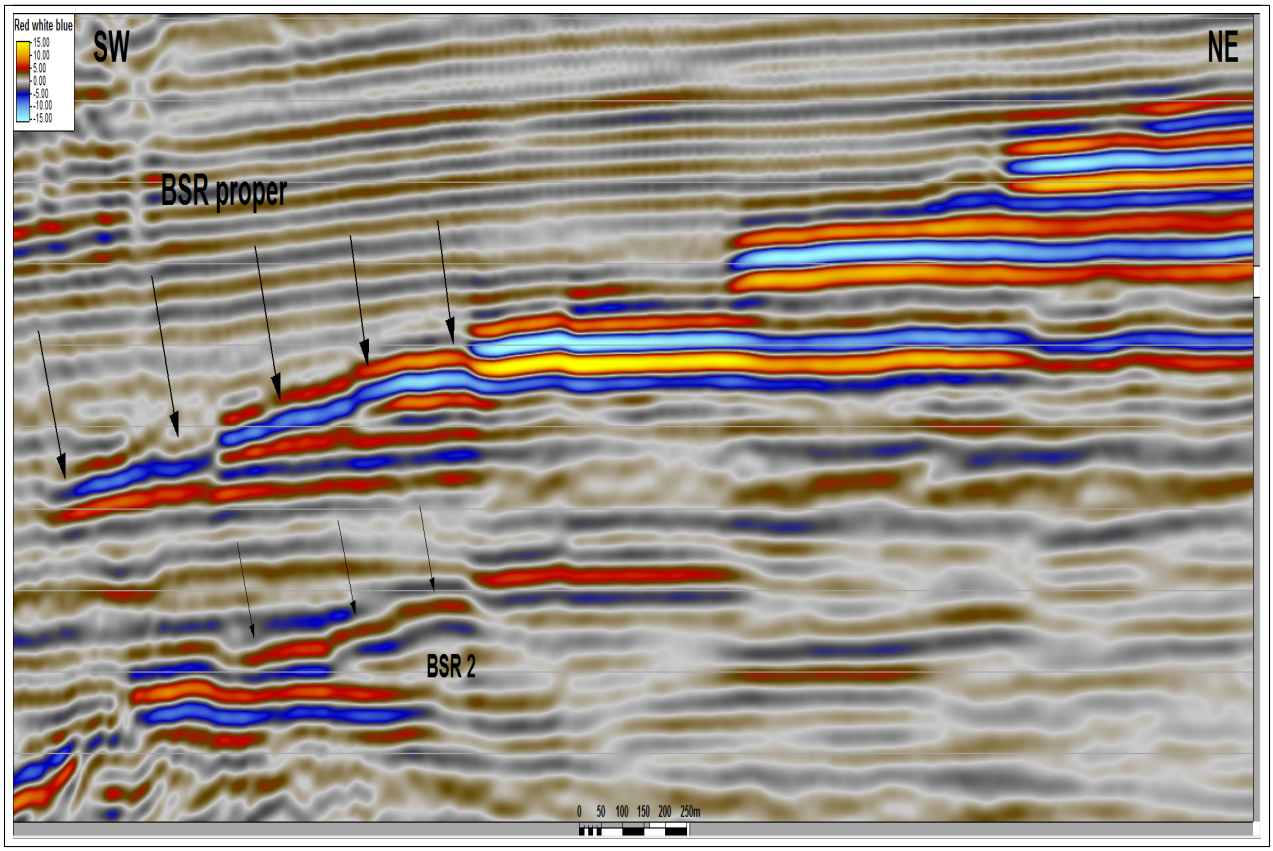

Figure 5.18: Section taken from Figure 3.2.

the dominant wavelength of the wavelet pulse (Gelius and Johansen, 2010).

$$\lambda \cong \frac{V}{f_c} \tag{5.1}$$

The wavelength, λ is given by Equation 5.1. One quarter of a wavelength is called the tuning thickness. In this study two ricker wavelets of 40 and 85 Hz are used in order to observe the difference in vertical resolution. In Table 5.5, it can be observed that the tuning thickness for a 40 Hz wavelet exceeds the minimum thickness of the gas-bearing sediments, which will result in limited visibility of the thin layers.

In Figure 5.19a, a 40 Hz wavelet is implemented into the analytic simulator. The BSR proper is observed as a continuous reflector. The two smaller gas layers have thickness below the tuning thickness, and creates interference, resulting in loss of the reflections. For Figure 5.19b, a 85 Hz wavelet is used, which reveals the smaller layers. In addition

Table 5.5: Tuning thickness for 40 and 85 Hz

Frequency	Velocity [m/s]	Wavelength [m]	Tuning thickness [m]
40 Hz	1750	44	11
85 Hz	1750	20	5

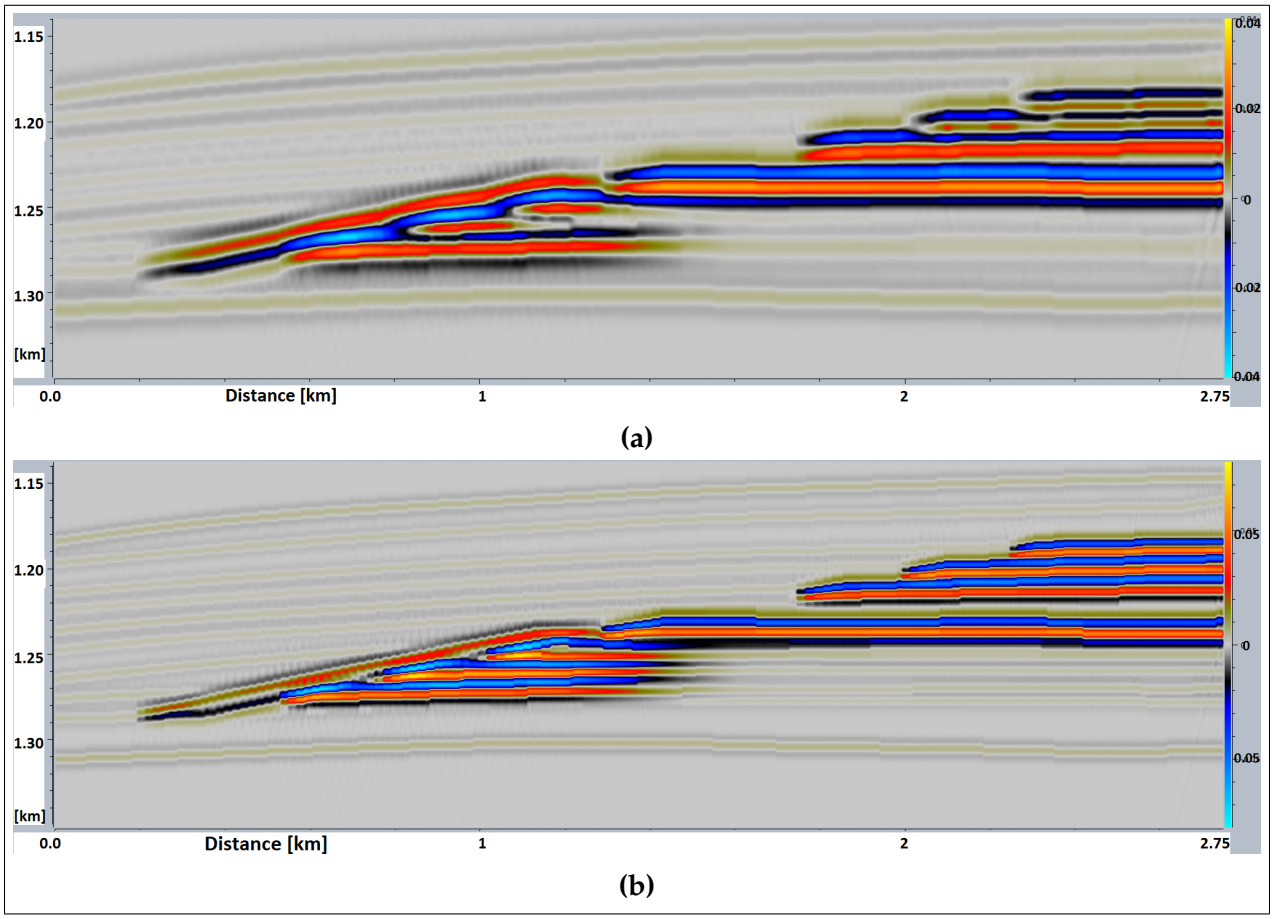

Figure 5.19: Analytic PSDM simulator for a) 40 Hz, and b) 85 Hz wavelet.

the BSR proper is observed as a discontinuous reflector in between the gas-bearing layers. The local-target shows similar results as for the analytic PSDM simulator. In Figures 5.20a and 5.20b a closer look at the BSR proper for 40 Hz and 85 Hz is displayed using the local-target PSDM simulator. The gas hydrate saturated sediments are observed to enhance the reflection at the gas interfaces, but experience a lower reflection at the brine interface. Figure 5.20a shows a similar reflection as observed in the real seismic (Figure 5.18).

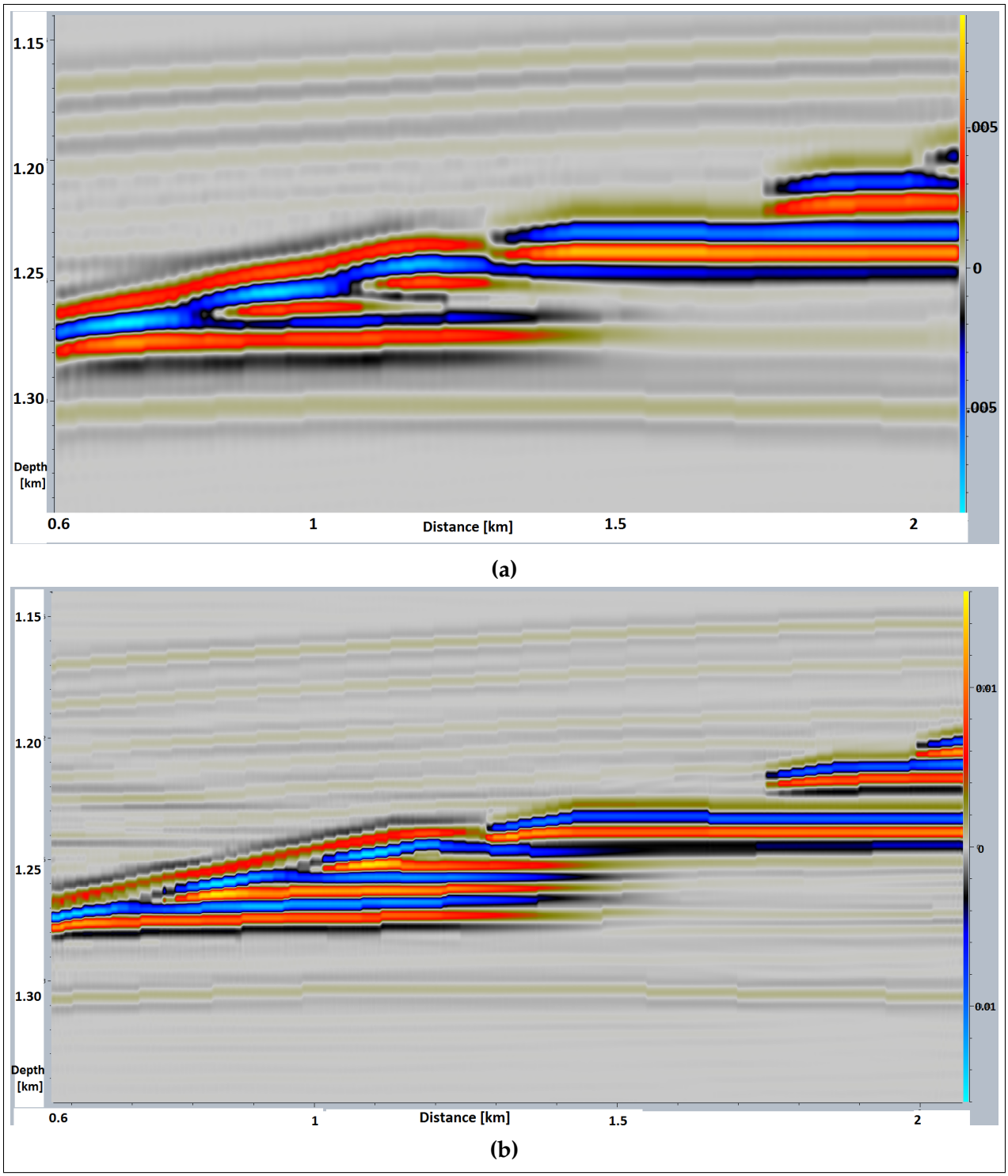

Figure 5.20: Local-target PSDM simulator for a) 40 Hz, and b) 85 Hz wavelet.

The BSR proper reflection is smooth and continuous, due to tuning thickness issues for the 40 Hz wavelet. In Figure 5.20b, the wavelength is smaller, resulting in a better resolution for the thinner layers, allowing the seismic to distinguish between the reflections from the gas and brine saturated sediments.

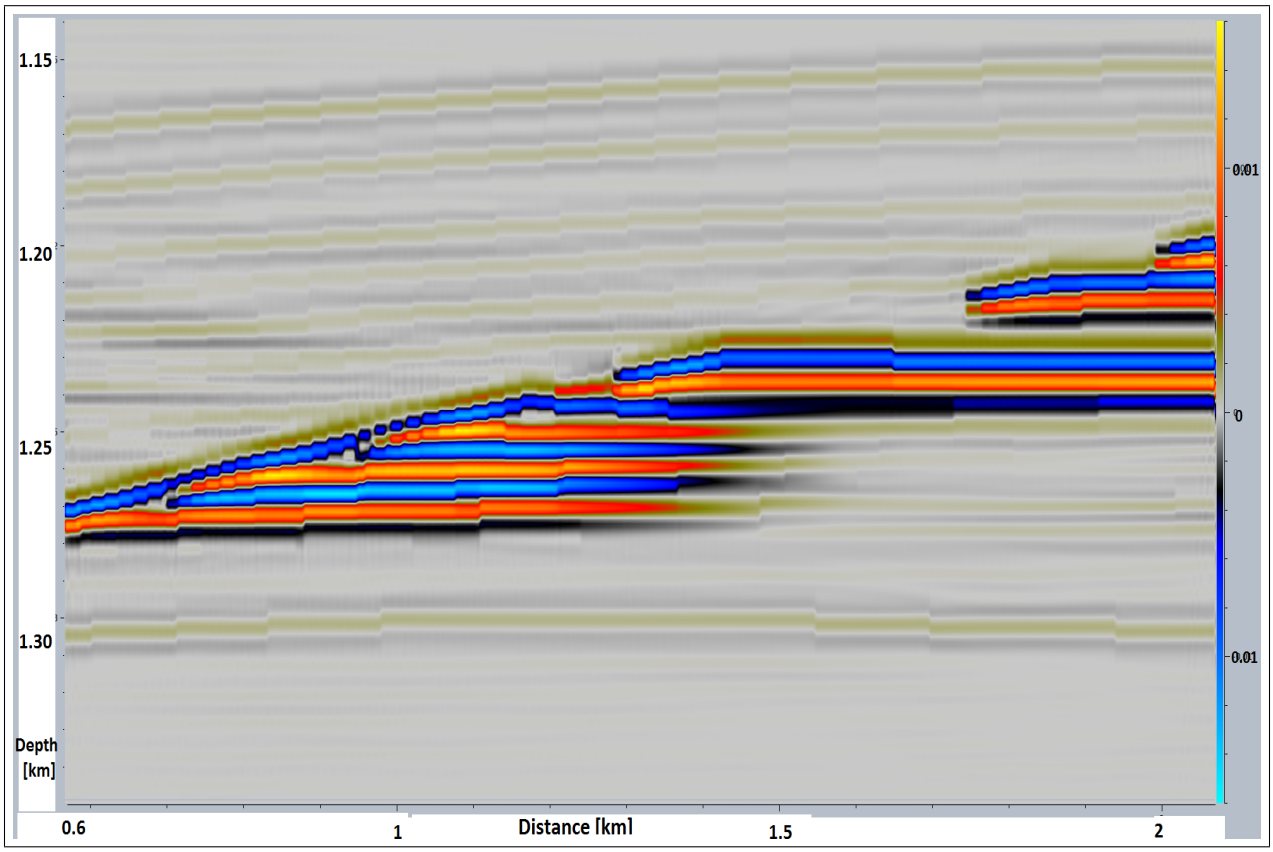

Figure 5.21: No gas hydrate present. Additional free gas have been added to the BSR proper.

Bünz et al. (2005) argued that the main constituent for the observed BSR at the southern Vøring plateau, was the gas saturated sediments. In Figure 5.21, a small gas layer have been added beneath the BSR. No gas hydrates are present in this figure. What can be observed, is that the BSR proper exhibit a continuous negative reflection, even for a 85 Hz wavelet.

For a smaller frequency bandwidth, the BSR can show a continuous reflection even for small gas hydrate concentrations, while higher frequencies are able to distinguish between the reflections. The real seismic data was obtained for a main frequency of 85 Hz (Bünz and Mienert, 2004), which implies that Figure 5.20b should be able to distinguish between the reflections.

5.5 Resolution

In 2D convolution modelling the resolution depends on frequency, sampling interval, incidence angle and the velocity model. As already explained, the vertical resolution is $1/4$ of the wavelength λ. The tuning thickness is of special interest for gas hydrate and gas saturated layers in this study, because of the small thickness of some of the layers. The 2D convolution makes use of a Fourier transform of the target reflectivity grid and background model, in order to obtain the complete spectrum of seismic frequencies in the wavenumber domain. The seismic reflection can only retrieve a band-limited coverage of the frequencies, because zero to low wave-numbers, and high wave-numbers are removed (Lecomte, 2008; Gelius and Johansen, 2010). The band-limited seismic spectrum retrieved, is the PSDM filter. By using an inverse FT on the spectrum, the seismic image is found.

A PSDM filter and PSF for the local-target simulator in case 3, are shown for frequencies of 40 Hz in Figure 5.22a, and for 85 Hz in Figure 5.22b. The sampling in case 3 is 1 m in vertical and horizontal direction. In real seismic, the sampling corresponds to the CMP or CDP binning size, which for the multichannel 2D seismic line (NH9651-202) is 12.5 m. The sampling corresponds to both the sampling distance between individual traces, and the sampling of wave-numbers in the wave-number domain. Therefore, a sampling similar to that of the real seismic will result in loss of reflection energy, hence aliased reflections (Figure 5, Appendix A). Real seismic processing utilize filters removing some frequencies in order to prevent the reflections from aliasing and still have a broad frequency bandwidth. For the study in this thesis, the sampling have been chosen to present the best seismic image for the geologic structures.

In Figure 5.22a, the PSDM filter for a 40 Hz wavelet is shown in the wavenumber domain (Kx, Ky). The PSDM filter hence the PSF strongly depends on the model, survey and seismic source pulse (Gelius and Johansen, 2010). The vertical and horizontal sampling is inverse proportional to the wave-number range. For a sampling of 1 m, the wave-number range will correspond to 1000 1/km, because $1/0.001km = 1000$. As observed in Figure 5.22a, a sampling of 3 m horizontally and vertically would be sufficient to preserve the seismic energy as is done in case 1 and 2 for a 40 Hz wavelet.

In Figure 5.22a, the vertical and horizontal resolution can be obtained from the length and thickness of the PSF. Vertical and horizontal resolution for the 40 Hz and 85 Hz wavelet, are listed in Table 5.6 based on the observed PSF in Figures 5.22a and 5.22b.

Table 5.6: Vertical and horizontal resolution

Frequency	Vertical resolution [m]	Horizontal resolution [m]
40 Hz	10	17
85 Hz	4	8

In Figure 5.22b, the PSDM filter and PSF for a 85 Hz wavelet is displayed. The filter is larger than for the 40 Hz wavelet, due to the increased sampling interval. In order to cover the reflection energy, the sampling have to be as low as 1 m, because a too coarse sampling would exclude some of the energy (as observed in Figure 6, Appendix A). The reason for the wide distribution of reflection energy, is because the shot-line length in this case is 5 km, which will give a wide offset distribution and hence a wide incidence angle range. The PSF is smaller in vertical and horizontal direction, due to the smaller wavelength of the 85 Hz compared to the 40 Hz wavelet.

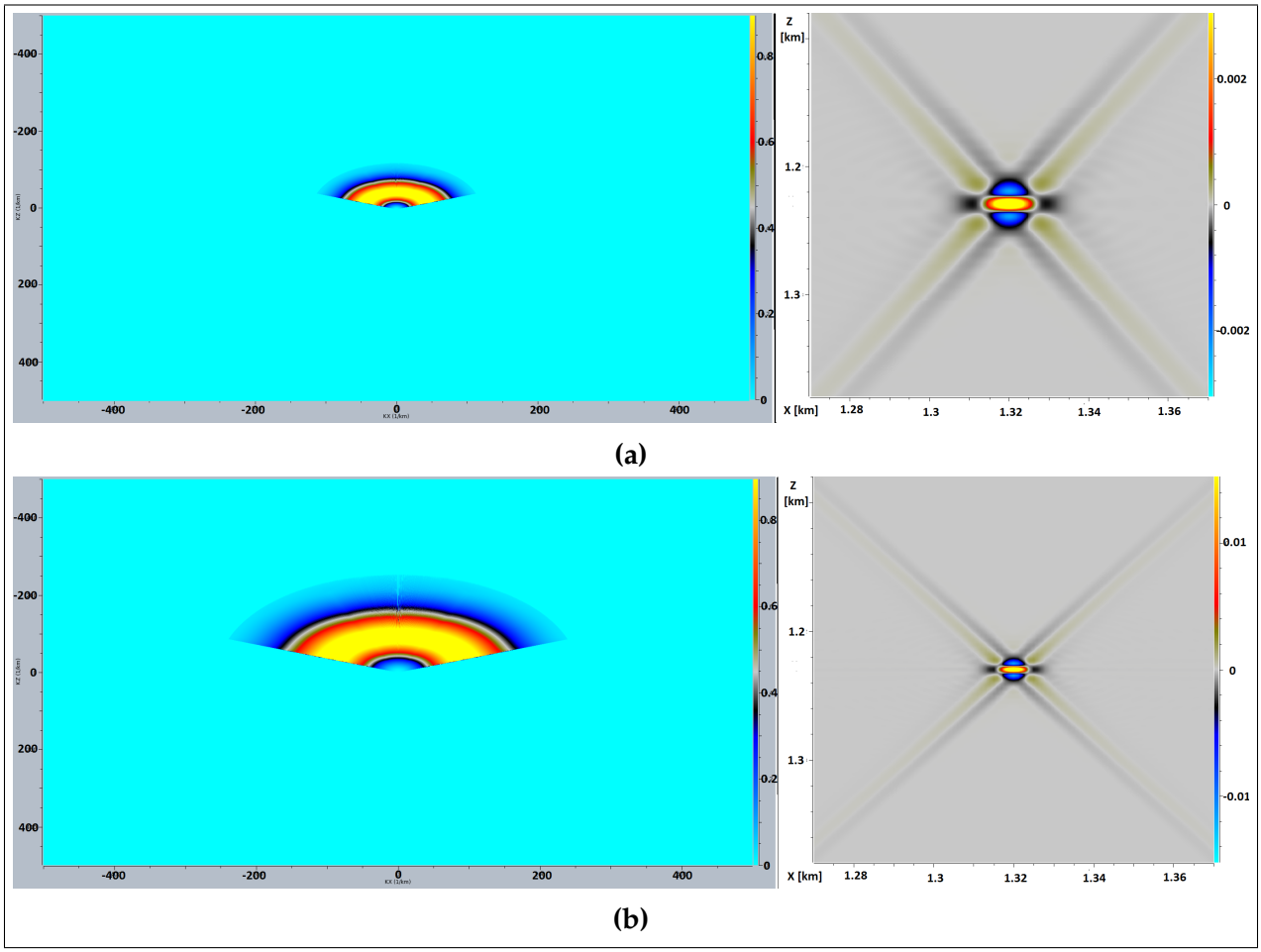

Figure 5.22: Local-target PSDM simulator showing PSDM filter and the corresponding PSF for a) 40 Hz, and b) 85 Hz.

Chapter 6

Discussion

The following chapter will outline the discussion of the results, and methods used in this study. Results are compared to known theory and assumptions made for modelling procedures used. More precisely, the discussion aims to present and evaluate the main findings, as well as highlight potential uncertainties and pitfalls associated with the BSR detection of gas hydrates. This chapter will evaluate the reliability and validity of the geological model, rock physics methods, and seismic modelling performed in this study.

Geological model

The reliability of the geological models used in this study will be discussed in this sub-section. The geological model created is based on the geological setting on the southern Vøring plateau. Mineral constituents found in this area have been used in the rock physics modeling, hence implemented in the seismic modelling.

Gas hydrate distribution in pore voids is greatly affected by the host sediments properties. Clennell et al. (1999) proposed that some minerals could promote heterogeneous hydrate growth, but most organic and inorganic minerals would inhibit hydrate formation. Fine-grained sediments like clay and silts will prohibit large hydrate formation and result in segregated heterogeneous growth, while coarser sediments are proposed to

be a better environment for massive hydrate formation (Clennell et al., 1999). The sediments used to create the geological model in this study, are reportedly composed of contouric hemipelagic deposits in the Naust formation (Mienert et al., 2005). Hemipelagic sediments are muds, coarser than pelagic clays. The sediments at the southern Vøring plateau are coarse enough to promote hydrate formation, but the hemipelagic muds may be an inhibitor, preventing large gas hydrate growth. This poses a great uncertainty, because the sediments may be too fine-grained for gas hydrates to cement grains, and achieve high saturations in the pore voids in this study. However, elastic properties would not vary significantly for other mineral compositions. In addition, the proposed composition have been gathered from geotechnical information from a known gas hydrate reservoir, giving sufficient validity for use in this study (Bünz et al., 2005).

The geological models created with the 2D model-builder assumes constant elastic properties in each layer, except for when the sampled function tool is used. The assumption of isotropic homogeneous materials without lateral variations will pose limitations. Marine sediments generally exhibit composition changes in layers, creating local variations in reflection strength. Vertical and lateral velocity variations will not be taken into account in the geological model, due to 2D model-builder limitations. This will make the results slightly less comparable to real seismic, but for the study of gas hydrate effect on seismic reflections in this study, the models are sufficient.

The BSR is believed to coincide with the BGHS in this study. However, it should be noted that discrepancies have been observed in some cases between the predicted depth of the BGHS and the BSR (Clennell et al., 1999). This is due to the fact that water in-situ sediments is less saline, and especially small contributions of H_2S will make the hydrate more stable, shifting the stability zone. Therefore it is of special importance to have good geotechnical information about the area of interest. The BSR in the study area is reported to coincide well with the predicted BGHS (Mienert et al., 2005).

Rock physics model

Forward modelling methods in rock physics are based on assumptions and approximated parameters. Although this is a pre-existing condition, associated uncertainties will pose limitations on the models. Knowing the limiting factors will help to gain confidence in the results.

The hybrid rock physics method proposed by Dvorkin et al. (1999) and Johansen et al. (2003) illuminate a potential critical gas hydrate saturation for cementing of grains in this study. Gas hydrate saturation and distribution have been shown to affect the stiffness of the sediments in various manners. The rock physics models show that gas hydrates replacing pore water, will have an almost insignificant effect on the sediment stiffness up to a saturation of 40%, where cementing of grains is initiated. Above the critical saturation at 40%, gas hydrates are observed to cement grains, increasing the stiffness remarkably. This observation coincide well with observed P- and S- velocities for lower and higher gas hydrate saturations (Bünz et al., 2005; Andreassen et al., 2003; Ecker et al., 1998; Dvorkin et al., 1999; Sloan and Koh, 2007). In addition, free gas saturated sediments experience a substantial decrease in P-wave velocity with only small amounts of gas present in the pore voids. Both gas hydrate and gas saturation affects the P-velocity greatly.

An important part of rock physics modelling is to understand the assumptions behind the methods, as they act as uncertainties for the results. Coupling CCT with SCA, assumes spherical grains and pore inclusions for an isotropic material (Mavko et al., 2009). Pores and grains are often composed of various shapes (ellipsoidal, spherical, etc.) and aspect ratios. Hyndman and Spence (1992) performed a study using ellipsoidal inclusions with aspect ratio of 0.1. The results revealed that the gas hydrate/water mixture would gain shear strength at 33% saturation as proposed to 40%. Johansen et al. (2003) observed the same result for partially frozen water in permafrost. Spherical inclusions is a simplified assumption done in this study, and the critical gas hydrate saturation would be lower following a decrease in aspect ratio (Avseth et al., 2014). Berryman (1980) claimed that the SCA method predicting the shear modulus rigidity threshold at 40% for spherical inclusions, failed to locate the threshold precisely. This study acknowledge the potential

effect of different pore/grain shapes and distribution on the sediment stiffness. However, the results in this thesis work for spherical inclusions seem to match well with results obtained previously.

This study assumes that the critical porosity is 40%, and the coordination number is 8.2. The critical porosity of 40% have been proposed by other authors such as Bünz et al. (2005) and Andreassen et al. (2003), doing modelling on the same gas hydrate system as in this study. The critical porosity is an important parameter in the SCA and CCT method, because it governs the shear modulus threshold of the sediments greatly (Berryman, 1980). The coordination number of grains depend on the grain size distribution and compaction related to porosity. The most important relation, is that the coordination number increases with a decreasing porosity (Mavko et al., 2009). There are no exact answers related to the coordination number, but correlations suggest that a value of around 8 for 40% porosity can be appropriate (Mavko et al., 2009). The coordination number and critical porosity affect the rock physics models greatly, and pose uncertainties, but values in this study coincide well with other studies and is deemed appropriate (Dvorkin et al., 1999; Johansen et al., 2003; Mavko et al., 2009).

The S-velocity calculated for gas hydrates and gas/brine saturated sediments can be observed as too high, compared to marine sediments. This is due to slip and/or torsion at the grain contact interfaces (Avseth et al., 2014). The shear modulus and hence the S-velocity calculated by contact-cement and contact (H-M) theory will be too high in the results. The shear modulus should have been assigned a shear relaxation factor between 0 and 1, to account for the high S-velocity as proposed by Avseth et al. (2014).

In general, elastic properties for pure gas hydrate structure 1 and 2 is obtained through laboratory experiments (Clennell et al., 1999). Bulk and shear modulus is calculated based on predicted or measured salinity, gas composition, and temperature/pressure at the proposed gas hydrate stability zone. Studies have shown, that elastic properties vary substantially from each experiment (Yun et al., 2005). This study illustrates briefly the effect different gas hydrate structures exhibit on the P- and S- wave velocity. The results give reason to believe that structure and gas composition can create large contrasts in predicted sediment velocities, hence caution should be taken when applying and calculating these values.

Gas hydrates below the critical saturation of 40% in Figure 6.1, are assumed to behave as a fluid. However, the assumption to mix gas hydrate and water in this manner, poses some problems. Gas hydrates have shear stiffness, and do not behave as a fluid. The assumption using Gassmann's formula implies that the shear stiffness of the fluid is zero. Although, this is assumed below the critical saturation using the SCA method, the physical behavior of gas hydrates might behave different. Gassmann's formula can only be used for low gas hydrate saturations, and might even be inaccurate for concentrations up to 40% (Sain et al., 2010). This assumption might provide the greatest uncertainty to the model. However, authors have advocated that this rock physics assumption is the closest to real values found in marine sediments (Ecker et al., 1998; Jakobsen et al., 2000; Winters et al., 2004). The apparent match between unconnected gas hydrates floating in water and Gassmann formula, might be due to lack of a better method. However, results in this study also show that this method gives reasonable results compared to real data.

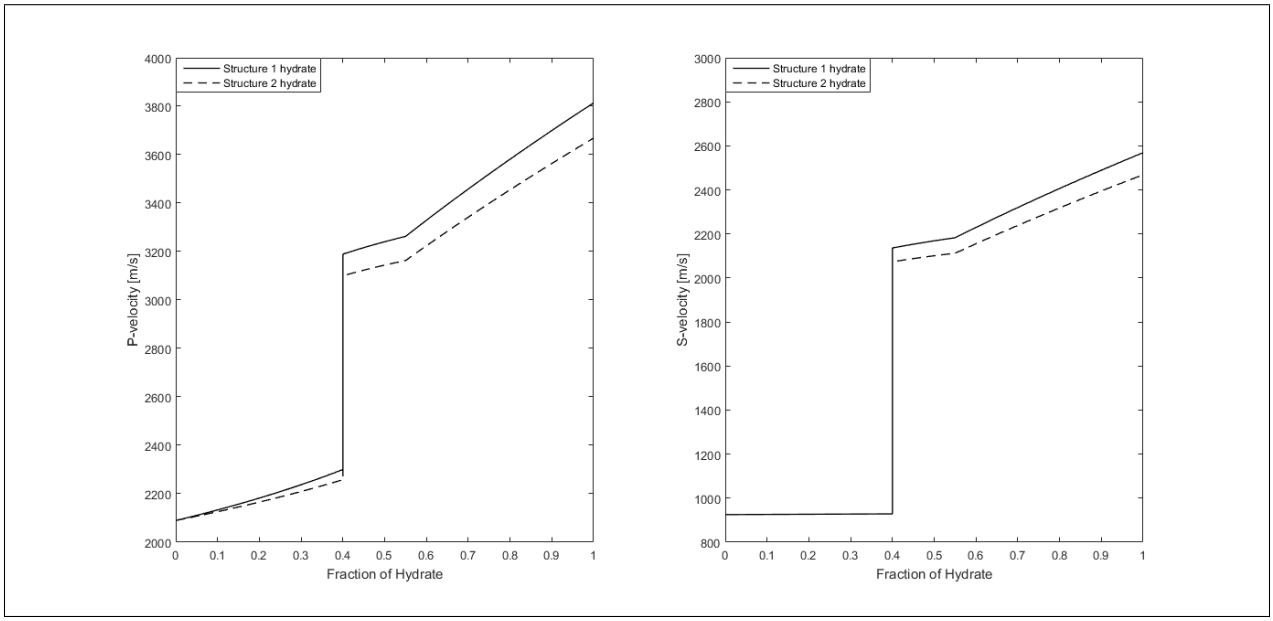

Figure 6.1: Water/hydrate mixture saturated sediments. P- and S-velocity versus gas hydrate saturation for sediments saturated with water/gas hydrate mixture (scheme 1).

The entire pore void is assumed to be saturated with fluids in the rock physics models. This assumption will in general not hold for natural sediment systems, because of

permeability, cracks and closed pore limitations. A proposed patchy saturation, as performed in case 3 of the seismic modelling might give results closer to reality. The mixing of brine and gas is assumed to be uniform. The gas can move more easily between pores than water, and might be trapped in closed pores or cracks (Sain et al., 2010). In that case a more realistic modelling strategy would be to use a patchy saturation model with Hill average equation.

Gas hydrates have been distributed as cement and pore-filling material, as well as solid inclusions suspended in fluid through this study. Gas hydrates/ice cementing grains have been proposed by Dvorkin et al. (1999), Ecker et al. (1998), and Johansen et al. (2003). However, large enough saturations for this method to apply, have mainly been observed in permafrost areas, and rarely in marine sediments (Sloan and Koh, 2007). Helgerud et al. (1999) propose that a better model is to treat gas hydrates as a part of the sediment grains. Hydrates as inclusions and part of the matrix framework have been advocated to give a better fit to real data from marine systems (Helgerud et al., 1999; Chand et al., 2004; Bünz et al., 2005). This might be correct estimates for low gas hydrate saturations, but the proposed model in this thesis (Figure 6.1) might be a better model for higher gas hydrate saturations. It has been proposed by Tohidi et al. (2001) through experiments on hydrate formation, that growing of hydrate-crystals start at the water/gas interface, or around dissolved gas bubbles in water. Methane have low solubility in water, and will favor crystal-growth away from grain-contact, if the sediments are water-wet. However, Tohidi et al. (2001) propose that when most of the pore void is saturated with gas hydrates, cementation of grains is the most likely outcome.

The distribution of gas hydrates in sediments is extremely difficult to predict, when using rock physics methods. Clennell et al. (1999) advocate that findings from around the world suggests that gas hydrates typically occur in the form of segregated bodies such as, lenses, nodules, pellets, or sheets. Collett (2002) proposed the same distributions schemes, and found that most recovered off-shore gas hydrate samples consisted of individual grains and particles, fitting to the unconnected model in this study. The different distributions will constrain whether the accumulation is heterogeneous or uniform through the pore voids (Collett, 2002). Rock physics methods have not yet the ability to implement the variety of distribution schemes posed by gas hydrates. In any case, gas hydrates

cementing grains might provide the closest method to high saturations as proposed in this study. Therefore, the validity of the rock physics method provided in this thesis, should be acknowledged as a potential for further investigation.

Seismic modelling

Seismic modelling have been performed using the ray-based 2D convolution method. Different gas hydrate distribution and saturation schemes show different results on the Bottom Simulating Reflector (BSR). The BSR arises from the P-velocity contrast between gas hydrate saturated sediments, and sediments beneath. Hyndman and Spence (1992) proposed that the BSR visibility due to gas hydrates with no free gas layer beneath, only shows clear reflections when gas hydrate saturations are above 33% of the pore space. Similar observations was done by Ecker et al. (1998), where no BSR was observed for gas hydrates deposited away from grain contact. The most evident reflection at the BSR, comes from gas hydrates cementing at grain contact with free gas beneath. From the results, it is apparent that a gas hydrate saturation above 40% will have an effect on the BSR even without a gas saturated layer beneath. For saturations lower than 40%, the reflection becomes to weak, and will be neutralized by interfering noise (Ecker et al., 1998).

The velocity model chosen in the target for the background model have strong constraints on the propagation of waves and the backscattering of energy in PSDM based modelling techniques (Lecomte et al., 2015). The velocity have been chosen as an average between the observed values in the target. Case 2 and 3 in this study shows the BSR as a dipping reflector. In this case, the velocity model might affect the resolution to some degree, due to substantial velocity variations in the target. Majority of models created in this study will in any case, have results within a reasonable range of the average velocity chosen. However, for the extreme case of 100% gas hydrate saturated sediments in case 2, the velocity contrast compared to the background model becomes significant. Therefore, these results might have somewhat of a reliability issue, when it comes to reflection strength and resolution of the respective reservoir.

The marine survey configuration chosen for the local-target PSDM simulator, is based on the real seismic data. Shot-line length is varied from 3 km in case 2, and 5 km in case 3. The change in shot-line length will result in an increased range of incident angles. Incident angle will affect illumination vectors, hence the resolution of the seismic image (Lecomte et al., 2003). The average angle option used in this study creates vectors for all illumination points. Generally for a larger offset, some structures could potentially not be illuminated (Lecomte et al., 2015). The incident angle and offset can act as important parameters, but in this study however, the illumination of structures fits well with the geological models.

The gas hydrate cement model creates a high velocity zone, compared to other sediments, yielding a strong reflection amplitude. Real seismic data is often contaminated with noise, which would likely make the reflection amplitudes for lower gas hydrate saturations (below 40%) negligible (Ecker et al., 1998). Interfering acoustic noise would illuminate the reflection visibility in a more realistic way, and lower gas hydrate saturated sediments would probably not be visible on its own.

Attenuation of acoustic waves in sediments are higher for higher frequencies, and when fluids are present in sediments (Dai et al., 2008; Gelius and Johansen, 2010). Attenuation or Q-factor for P- and S-waves is possible to implement in the 2D model-builder software, but is absent in this study, assuming no attenuation. However, the attenuation will have an effect on the amplitude intensity of the seismic image. Gas and gas hydrates present in sediments will result in increasing attenuation, hence less energy propagating down (Dai et al., 2008). For case 2, a cemented gas hydrate accumulation of high saturation as observed in Figure 5.15, will attenuate a large amount of the wave energy. The attenuation will play an important part in the illumination of the BSR, because gas/water in sediments above the gas hydrates might decrease the observed reflection at the BSR (Lee and Dillon, 2001). It is important to note that accounting for interfering noise and attenuation in this study, would give much more realistic seismic images more comparable to real seismic.

If gas hydrates are cementing the grains at the BGHS, gas and water will eventually be trapped beneath the gas hydrates, unable to penetrate through the sediments (Ecker et al.,

1998). Thus fluid flux into the stability zone will stop, and gas hydrates will decrease in saturation away from the BGHS. The strongest reflections are observed at the BSR, while the gas hydrate saturation decreases upwards often causing amplitude blanking in real seismic. The amplitude blanking occurs when the acoustic impedance show little or no variation between sedimentary layers. Above the BSR, the lower gas hydrate saturation causes a negligible acoustic impedance contrast with the marine sediments, resulting in amplitude blanking (Lee and Dillon, 2001). Therefore, the gas hydrate accumulation in case 2, and its apparent reflection at the top of the hydrate zone, will give an unrealistic seismic reflector.

The sampling interval is much smaller for the models in this study, compared to the seismic acquisition of real data. However, the sampling needs to be small in this case, because it will affect the geological structure illumination in addition to the PSDM filter (Lecomte et al., 2003). If the sampling were to coincide with the CDP distance, a distorted seismic image would be obtained (Figure 5, Appendix A). This is a constraint using the 2D convolution modelling method. In real seismic processing, it is possible to design specific frequency filters in order to prevent loss of seismic energy related to coarse sampling.

Because the layers in the survey area are reported to have small thicknesses, the frequency will have an impact on the vertical resolution (Bünz and Mienert, 2004). A 40 Hz wavelet has a larger wavelength than many of the smaller gas layers, which will result in interfering reflections. Choosing a wavelet of 85 Hz will solve this problem, as the tuning thickness covers layer thicknesses down to 5 m. However, as discussed the sampling interval has to be smaller for higher frequency band-widths.

The modelling performed for case 3, aims to represent the real gas hydrate system from the southern Vøring plateau, as realistic as possible. The gas hydrate saturations in this area have been reported as low, following a distribution of hydrates away from grain contact (Bünz et al., 2005). Because of low hydrate saturations, it is difficult to predict whether the BSR reflection originates from gas hydrates or the underlying gas layers (Bünz et al., 2005). As observed in Figure 6.2, the synthetic seismic sections match the real seismic image relatively good. However, the smoothness of the real seismic reflections coincide better with the results for the 40 Hz wavelet. This is believed to be related to the

processing of the seismic data compared to the 2D convolution model used in this study.

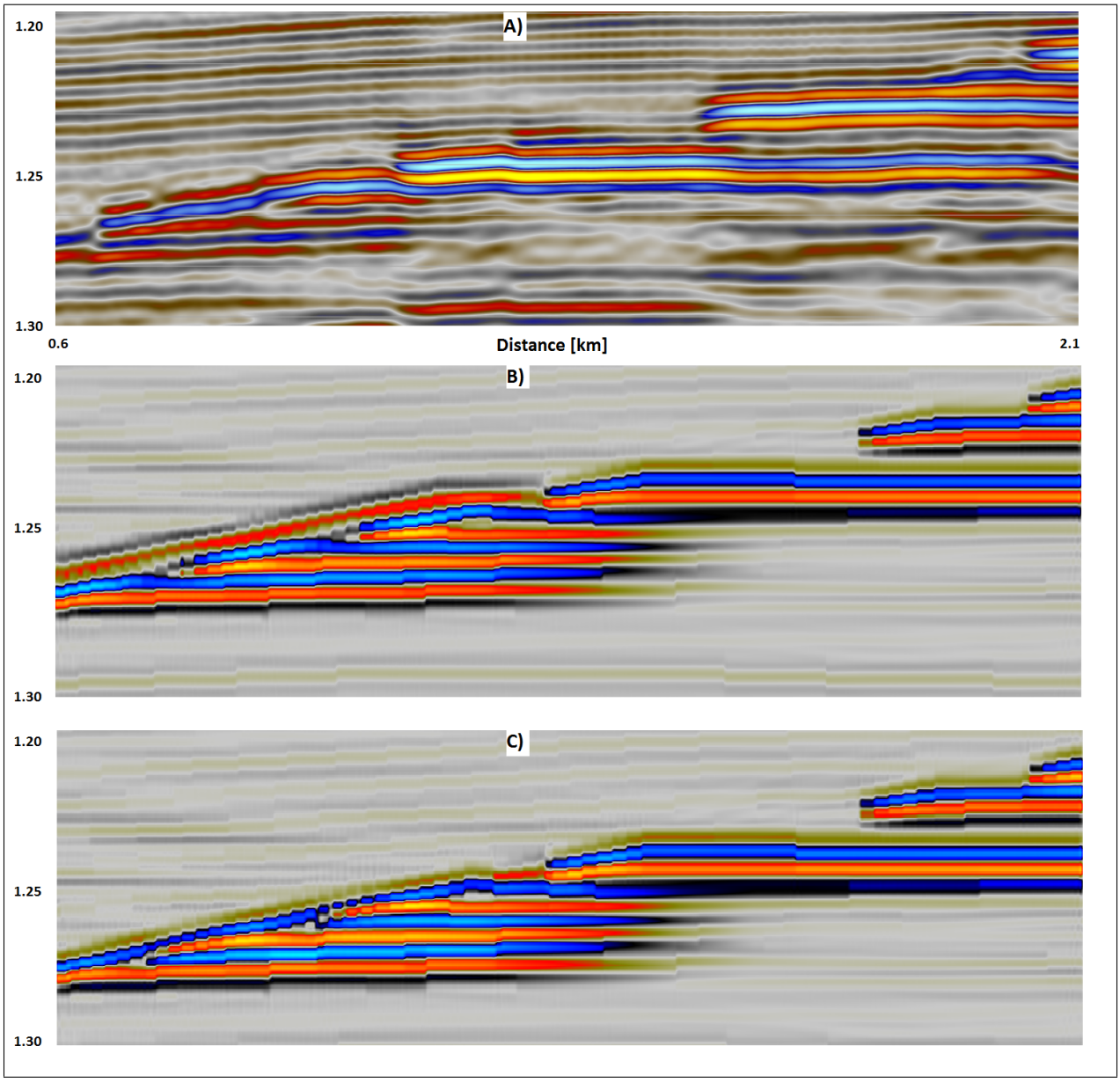

Figure 6.2: Comparing the real seismic data (A), with the synthetic data with gas hydrates (B), and only gas (C).

From the results, it is clear that gas present in sediments beneath the BSR makes the greatest contribution to the observed BSR reflection. For gas hydrate saturations below 40%, the impedance contrast becomes too small when brine is situated beneath the BSR.

Without gas saturated sediments, the BSR would be difficult near to say impossible to detect. The results for case 3, show a much lower acoustic impedance where no gas is present. In real seismic data, the reflection amplitude for the BSR proper seems to be continuous, and cross-cutting several sedimentary layers. An explanation to this observed difference could be that gas is situated below the entire gas hydrate zone at this area (as in Figure 5.21), due to vertical permeability in the form of cracks or permeable sediments. Another possibility, is that low saturation of gas hydrates is present as suggested by Andreassen et al. (2003); Bünz et al. (2005), but the frequencies available in the seismic band-width is too coarse sampled, resulting in tuning at the BSR proper. This would result in a continuous reflection, while the gas hydrate distribution might occur in a patchy and discontinuous manner.

Most off-shore gas hydrate reservoirs have low gas hydrate saturations (5-20%) inhabiting the pore voids of marine sediments (Sloan and Koh, 2007). The study area, for which elastic properties of sediments have been retrieved from a geotechnical bore-hole, shows evidence of low gas hydrate saturations (Bünz et al., 2005). However, gas hydrates present in permafrost areas are observed to have a much higher saturation compared to off-shore accumulations. The Mallik and Ignik Sikumi fields in Canada and Alaska have been reported to have gas hydrate saturations higher than 50%. Gas hydrates are observed to cement grains in these areas, stiffening the sediments, and resulting in high P and S-velocities (Chand et al., 2004; Riedel et al., 2014).

This study assumes that cementing initiate at a specific high gas hydrate saturation. However, most of the off-shore gas hydrate accumulations are below 40%, probably governed by host sediments, grain size distribution, and fluid influx. It have been suggested by (Sloan and Koh, 2007), that the worldwide off-shore gas hydrate saturation has an average of 3.5% of pore voids. High saturations only exist in very local areas off-shore such as the Hydrate Ridge and Gulf of Mexico sites (Sloan and Koh, 2007). The identification of gas hydrate saturations without free gas beneath, will probably make it impossible to observe the BSR. Locations exist where gas hydrates exhibit no BSR reflection. At the northern Gulf of Mexico, gas hydrates were recovered without showing a BSR on the seismic image (Kvenvolden et al., 1993). For higher gas hydrate saturations cementing grains, the BSR will be visible. In addition, the S-velocity will be

elevated, making it possible to detect gas hydrates with converted P-S waves. In any case, the entrapment of free gas beneath the gas hydrate stability zone, seems to be the most prominent evidence of gas hydrates. For lower gas hydrate saturations, AVO techniques can be used in order to raise the level of security in the observations. V_p/V_s ratio will increase with gas hydrate saturations up to 40%, due to the nearly constant S-velocity (Ecker et al., 1998). For hydrate saturations above 40%, the S-velocity will increase with the P-velocity making the detection more difficult for AVO.

The BSR reflection is in many cases a direct method of detecting gas hydrates, but several factors might influence the findings. It is important to understand how, where and why gas hydrates form, in order to increase the level of security in the BSR reflection. Gas hydrates can be present even without an observed BSR (Kvenvolden et al., 1993).

Chapter 7

Concluding Remarks

7.1 Conclusion

The results obtained in this study, gives important insight into the effect of gas hydrates on seismic reflection data. The most significant findings obtained from this study, is outlined as follows.

- A rock physics method have been created based on gas hydrate saturation and distribution in pore voids throughout this thesis work. The method is able to calculate the potential critical saturation for when gas hydrates start to cement sediment grains. The critical saturation for spherical grains have been predicted to occur for saturations above 40% using this method.

- Distribution of gas hydrates in pore voids are modeled for three different scenarios. Hydrate cement deposited at grain contact results in the largest velocity contrast, while hydrates deposited away from grain contact show the weakest contrast.

- Frequency, illumination and sampling are important when looking at the seismic resolution of gas hydrate reservoirs. Tuning thickness and sampling effects will affect the ability to distinguish between a continuous or discontinuous gas hydrate accumulation. A frequency of 40 Hz shows a continuous reflection, while 85 Hz

distinguish the same reflection as discontinuous for the gas hydrate zone in this study.

- A clear seismic reflection is observable for gas hydrate saturations above 40% without a free gas saturated layer beneath. For lower saturations the reflections become weak, implying that free gas needs to be present beneath the gas hydrate zone, in order to observe a visible reflection.

- The southern Vøring plateau gas hydrate system have low gas hydrate saturations, but sufficient saturation in order to trap free gas. The synthetic seismic images show results within reason, compared to the real seismic data.

- Comparison with real seismic data, suggests that the method provided in this study can be used in order to predict gas hydrate distribution and saturation relatively accurate. In any case, the rock physics approach and seismic modelling performed, will give important information regarding gas hydrates cementing grains at high saturations.

- The evidence of a bottom simulating reflection will need a good understanding of the gas hydrate saturation and distribution, in order to increase the certainty of the seismic interpretation. Sufficient information about gas hydrate structure through laboratory experiments, distribution in pore voids and formation mechanisms are needed, in order to quantify potential gas hydrate reservoirs off-shore. This study have provided a possible relation between gas hydrate saturation, distribution and seismic imaging.

7.2 Future work

The BSR is in many cases the best identification tool for detecting gas hydrates. However, care must be taken when interpreting gas hydrate accumulations based on the BSR reflection. AVO have been introduced as a potential detection method for finding gas hydrates. Several seismic acquisitions have used Ocean Bottom Cables (OBC), in order to investigate the converted P to S waves (Bünz et al., 2005). The S-velocity can be an important indicator for gas hydrates both above and below the critical saturation found in this thesis. V_p/V_s ratio is able to predict an increase in gas hydrate saturation below 40% saturation, due to a slight increase in P-velocity and a nearly constant S-velocity. Above the critical saturation, S-velocity is predicted to show an elevated reflector where gas hydrates are present. The rock physics model created in this thesis, based on the work of Dvorkin et al. (1999) and Johansen et al. (2003), will give an important physical insight into gas hydrates, but fail to include several important factors regarding hydrate formation. Increasing the knowledge of gas hydrate saturation and distribution effect on the S-velocity might prove to be a potential important identification tool in the future.

The importance of a carbon-neutral way of producing methane gas from gas hydrates at low costs, is an important subject in the future. A production method, of exchanging methane with CO_2 in order to produce the methane gas, have been proposed by Kvamme et al. (2007). Field tests performed by Conoco Phillips on the Ignik Sikumi field, resulted in produced methane and storage of CO_2 in gas hydrates. However, the exchange process was observed to occur slower than expected.

During my masters degree, I was able to work as a co-author on an article, studying the effect of adding H_2S to CO_2 and N_2 in order to increase the hydrate stability and accelerate the exchange process. By injecting the gas mixture into a gas hydrate reservoir, the thermodynamic stability of the hydrate would increase, resulting in a faster exchange process. The results highlights that only a small amount of H_2S will act to increase the stability of the formed CO_2 hydrate. (Kvamme et al., 2017). The process deposits CO_2 in hydrates, and produce methane that can in turn be used as an energy source. When burning methane for energy, one of the products for the process is CO_2. This means that

the exchange act as a carbon-neutral process. Mapping of gas hydrate accumulations off-shore is important, in order to find potential sites where CO_2, H_2S and N_2 could be injected and deposited. This could potentially be an important carbon-neutral energy source in the future. A potential project surrounding this article, could be to use seismic modelling to observe fluid substitution effects when H_2S is exchanged with CO_2 in the gas hydrate. Using AVO investigations to give cause for potential 4D seismic monitoring of such gas hydrate systems. The article written during this thesis can be found through this citation Kvamme et al. (2017).

Bibliography

Andreassen, K., Berteussen, K. A., Sognnes, H., Henneberg, K., Langhammer, J., and Mienert, J. (2003). Multicomponent ocean bottom cable data in gas hydrate investigation offshore of norway. *Journal of Geophysical Research: Solid Earth*, 108(B8).

Ashcroft, W. (2011). *A petroleum geologist's guide to seismic reflection*. John Wiley & Sons.

Avseth, P., Johansen, T. A., Bakhorji, A., and Mustafa, H. M. (2014). Rock-physics modeling guided by depositional and burial history in low-to-intermediate-porosity sandstones. *Geophysics*, 79(2):D115–D121.

Berndt, C., Bünz, S., Clayton, T., Mienert, J., and Saunders, M. (2004). Seismic character of bottom simulating reflectors: examples from the mid-norwegian margin. *Marine and Petroleum Geology*, 21(6):723–733.

Berryman, J. G. (1980). Long-wavelength propagation in composite elastic media ii. ellipsoidal inclusions. *The Journal of the Acoustical Society of America*, 68(6):1820–1831.

Bouriak, S., Vanneste, M., and Saoutkine, A. (2000). Inferred gas hydrates and clay diapirs near the storegga slide on the southern edge of the vøring plateau, offshore norway. *Marine Geology*, 163(1):125–148.

Bridge, J. and Demicco, R. (2008). *Earth surface processes, landforms and sediment deposits*. Cambridge University Press.

Bryn, P., Berg, K., Forsberg, C. F., Solheim, A., and Kvalstad, T. J. (2005). Explaining the storegga slide. *Marine and Petroleum Geology*, 22(1):11–19.

Buffett, B. and Zatsepina, O. Y. (2000). Formation of gas hydrate from dissolved gas in natural porous media. *Marine geology*, 164(1):69–77.

Bugge, T., Befring, S., Belderson, R. H., Eidvin, T., Jansen, E., Kenyon, N. H., Holtedahl, H., and Sejrup, H. P. (1987). A giant three-stage submarine slide off norway. *Geo-marine letters*, 7(4):191–198.

Bünz, S. and Mienert, J. (2004). Acoustic imaging of gas hydrate and free gas at the storegga slide. *Journal of Geophysical Research: Solid Earth*, 109(B4).

Bunz, S., Mienert, J., and Berndt, C. (2003). Geological controls on the storegga gas-hydrate system of the mid-norwegian continental margin. *Earth and Planetary Science Letters*, 209(3):291–307.

Bünz, S., Mienert, J., Vanneste, M., and Andreassen, K. (2005). Gas hydrates at the storegga slide: Constraints from an analysis of multicomponent, wide-angle seismic data. *Geophysics*, 70(5):B19–B34.

Chand, S., Minshull, T. A., Gei, D., and Carcione, J. M. (2004). Elastic velocity models for gas-hydrate-bearing sediments—a comparison. *Geophysical Journal International*, 159(2):573–590.

Chand, S., Minshull, T. A., Priest, J. A., Best, A. I., Clayton, C. R., and Waite, W. F. (2006). An effective medium inversion algorithm for gas hydrate quantification and its application to laboratory and borehole measurements of gas hydrate-bearing sediments. *Geophysical Journal International*, 166(2):543–552.

Chand, S., Rise, L., Knies, J., Haflidason, H., Hjelstuen, B., and Bøe, R. (2011). Stratigraphic development of the south vøring margin (mid-norway) since early cenozoic time and its influence on subsurface fluid flow. *Marine and Petroleum Geology*, 28(7):1350–1363.

Chopra, S., Castagna, J., and Portniaguine, O. (2006). Seismic resolution and thin-bed reflectivity inversion. *CSEG recorder*, 31(1):19–25.

Choy, T. C. (2015). *Effective medium theory: principles and applications*, volume 165. Oxford University Press.

Clennell, M. B., Hovland, M., Booth, J. S., Henry, P., and Winters, W. J. (1999). Formation of natural gas hydrates in marine sediments: 1. conceptual model of gas hydrate growth conditioned by host sediment properties. *Journal of Geophysical Research: Solid Earth*, 104(B10):22985–23003.

Cohen, J. E. (2003). Human population: the next half century. *science*, 302(5648):1172–1175.

Collett, T. S. (2002). Energy resource potential of natural gas hydrates. *AAPG bulletin*, 86(11):1971–1992.

Dai, J., Snyder, F., Gillespie, D., Koesoemadinata, A., and Dutta, N. (2008). Exploration for gas hydrates in the deepwater, northern gulf of mexico: Part i. a seismic approach based on geologic model, inversion, and rock physics principles. *Marine and Petroleum Geology*, 25(9):830–844.

Dickens, G. R., O'Neil, J. R., Rea, D. K., and Owen, R. M. (1995). Dissociation of oceanic methane hydrate as a cause of the carbon isotope excursion at the end of the paleocene. *Paleoceanography*, 10(6):965–971.

Dickens, G. R. and Quinby-Hunt, M. S. (1997). Methane hydrate stability in pore water: a simple theoretical approach for geophysical applications. *Journal of Geophysical Research: Solid Earth*, 102(B1):773–783.

Dvorkin, J., Berryman, J., and Nur, A. (1999). Elastic moduli of cemented sphere packs. *Mechanics of materials*, 31(7):461–469.

Dvorkin, J., Mavko, G., and Nur, A. (1991). The effect of cementation on the elastic properties of granular material. *Mechanics of Materials*, 12(3-4):207–217.

Dvorkin, J. and Nur, A. (1996). Elasticity of high-porosity sandstones: Theory for two north sea data sets. *Geophysics*, 61(5):1363–1370.

Dvorkin, J. and Nur, A. (2002). Critical-porosity models. *MEMOIRS-AMERICAN ASSOCIATION OF PETROLEUM GEOLOGISTS*, pages 33–42.

Ecker, C., Dvorkin, J., and Nur, A. (1998). Sediments with gas hydrates: Internal structure from seismic avo. *Geophysics*, 63(5):1659–1669.

Gelius, L.-J. and Johansen, T. A. (2010). Petroleum geophysics. *UniGEO as*.

Guéguen, Y. and Palciauskas, V. (1994). *Introduction to the physics of rocks*. Princeton University Press.

Haacke, R. R., Westbrook, G. K., and Hyndman, R. D. (2007). Gas hydrate, fluid flow and free gas: Formation of the bottom-simulating reflector. *Earth and Planetary Science Letters*, 261(3):407–420.

Haq, B. U. (1999). Methane in the deep blue sea. *Science*, 285(5427):543–544.

Helgerud, M., Dvorkin, J., Nur, A., Sakai, A., and Collett, T. (1999). Elastic-wave velocity in marine sediments with gas hydrates: Effective medium modeling. *Geophysical Research Letters*, 26(13):2021–2024.

Hillman, J. I., Cook, A. E., Sawyer, D. E., Küçük, H. M., and Goldberg, D. S. (2017). The character and amplitude of 'discontinuous' bottom-simulating reflections in marine seismic data. *Earth and Planetary Science Letters*, 459:157–169.

Hustoft, S., Mienert, J., Bünz, S., and Nouzé, H. (2007). High-resolution 3d-seismic data indicate focussed fluid migration pathways above polygonal fault systems of the mid-norwegian margin. *Marine Geology*, 245(1):89–106.

Hyndman, R. and Spence, G. (1992). A seismic study of methane hydrate marine bottom simulating reflectors. *Journal of Geophysical Research: Solid Earth*, 97(B5):6683–6698.

Jakobsen, M., Hudson, J. A., Minshull, T. A., and Singh, S. C. (2000). Elastic properties of hydrate-bearing sediments using effective medium theory. *Journal of Geophysical Research*, 105:561–577.

Johansen, T. A., Digranes, P., van Schaack, M., and Lønne, I. (2003). Seismic mapping and modeling of near-surface sediments in polar areas. *Geophysics*, 68(2):566–573.

Kaschwich, T., Gjøystdal, H., and Lecomte, I. (2011). Impact of diffraction on resolution of psdm. In *73rd EAGE Conference and Exhibition incorporating SPE EUROPEC 2011*.

Kaschwich, T. and Lecomte, I. (2010). Improved ray-based seismograms by combining modeling by demigration with a prestack depth migration simulator. In *72nd EAGE Conference and Exhibition incorporating SPE EUROPEC 2010*.

Kvamme, B., Graue, A., Buanes, T., Kuznetsova, T., and Ersland, G. (2007). Storage of co 2 in natural gas hydrate reservoirs and the effect of hydrate as an extra sealing in cold aquifers. *International Journal of Greenhouse gas control*, 1(2):236–246.

Kvamme, B., Iden, E., Tveit, J., Veland, V., Zarifi, M., and Qorbani, K. (2017). Effect of h2s content on thermodynamic stability of hydrate formed from co2/n2 mixtures. *Journal of Chemical & Engineering Data*.

Kvenvolden, K., Ginsburg, G., and Soloviev, V. (1993). Worldwide distribution of subaquatic gas hydrates. *Geo-Marine Letters*, 13(1):32–40.

Kvenvolden, K. A. (1993). Gas hydrates-geological perspective and global change. *REVIEWS OF GEOPHYSICS-RICHMOND VIRGINIA THEN WASHINGTON-*, 31:173–173.

Lecomte, I. (2006). Illumination, resolution, and incidence-angle in psdm: a tutorial. In *SEG Technical Program Expanded Abstracts 2006*, pages 2544–2548. Society of Exploration Geophysicists.

Lecomte, I. (2008). Resolution and illumination analyses in psdm: A ray-based approach. *The Leading Edge*, 27(5):650–663.

Lecomte, I., Gjøystdal, H., and Drottning, Å. (2003). Simulated prestack local imaging: a robust and efficient interpretation tool to control illumination, resolution, and time-lapse properties of reservoirs. In *SEG Technical Program Expanded Abstracts 2003*, pages 1525–1528. Society of Exploration Geophysicists.

Lecomte, I., Lavadera, P. L., Anell, I., Buckley, S. J., Schmid, D. W., and Heeremans, M. (2015). Ray-based seismic modeling of geologic models: Understanding and analyzing seismic images efficiently. *Interpretation*, 3(4):SAC71–SAC89.

Lecomte, I., Lavadera, P. L., Botter, C., Anell, I., Buckley, S. J., Eide, C. H., Grippa, A., Mascolo, V., and Kjoberg, S. (2016). 2 (3) d convolution modelling of complex geological targets beyond–1d convolution. *First Break*, 34(5):99–107.

Lee, M. W. and Collett, T. S. (2001). Elastic properties of gas hydrate-bearing sediments. *Geophysics*, 66(3):763–771.

Lee, M. W. and Dillon, W. P. (2001). Amplitude blanking related to the pore-filling of gas hydrate in sediments. *Marine Geophysical Research*, 22(2):101–109.

Makogon, Y., Holditch, S., and Makogon, T. (2007). Natural gas-hydrates—a potential energy source for the 21st century. *Journal of Petroleum Science and Engineering*, 56(1):14–31.

Makogon, Y. F. (2010). Natural gas hydrates–a promising source of energy. *Journal of Natural Gas Science and Engineering*, 2(1):49–59.

Maslin, M., Owen, M., Betts, R., Day, S., Jones, T. D., and Ridgwell, A. (2010). Gas hydrates: past and future geohazard? *Philosophical Transactions of the Royal Society of London A: Mathematical, Physical and Engineering Sciences*, 368(1919):2369–2393.

Mavko, G., Mukerji, T., and Dvorkin, J. (2009). *The rock physics handbook: Tools for seismic analysis of porous media*. Cambridge university press.

Mienert, J., Posewang, J., and Baumann, M. (1998). Gas hydrates along the northeastern atlantic margin: possible hydrate-bound margin instabilities and possible release of methane. *Geological Society, London, Special Publications*, 137(1):275–291.

Mienert, J., Vanneste, M., Bünz, S., Andreassen, K., Haflidason, H., and Sejrup, H. P. (2005). Ocean warming and gas hydrate stability on the mid-norwegian margin at the storegga slide. *Marine and Petroleum Geology*, 22(1):233–244.

Norsar (2016). Norsar software suite.

Rempel, A. and Buffett, B. (1997). Formation and accumulation of gas hydrate in porous media. *Journal of Geophysical Research: Solid Earth*, 102(B5):10151–10164.

Riedel, M., Goldberg, D., and Guerin, G. (2014). Compressional and shear-wave velocities from gas hydrate bearing sediments: Examples from the india and cascadia margins as well as arctic permafrost regions. *Marine and Petroleum Geology*, 58:292–320.

Sain, K., Ghosh, R., and Ojha, M. (2010). Rock physics modeling for assessing gas hydrate and free gas: a case study in the cascadia accretionary prism. *Marine Geophysical Researches*, 31(1-2):109–119.

Satyavani, N., Sain, K., and Gupta, H. K. (2016). Ocean bottom seismometer data modeling to infer gas hydrate saturation in krishna-godavari (kg) basin. *Journal of Natural Gas Science and Engineering*, 33:908–917.

Sloan, E. D. (2003). Fundamental principles and applications of natural gas hydrates. *Nature*, 426(6964):353–363.

Sloan, E. D. and Koh, C. (2007). *Clathrate hydrates of natural gases*. CRC press.

Tohidi, B., Anderson, R., Clennell, M. B., Burgass, R. W., and Biderkab, A. B. (2001). Visual observation of gas-hydrate formation and dissociation in synthetic porous media by means of glass micromodels. *Geology*, 29(9):867–870.

Waite, W. F., Helgerud, M. B., Nur, A., Pinkston, J. C., Stern, L. A., Kirby, S. H., and Durham, W. B. (2000). Laboratory measurements of compressional and shear wave speeds through methane hydrate. *Annals of the New York Academy of Sciences*, 912(1):1003–1010.

Winters, W. J., Pecher, I. A., Waite, W. F., and Mason, D. H. (2004). Physical properties and rock physics models of sediment containing natural and laboratory-formed methane gas hydrate. *American Mineralogist*, 89(8-9):1221–1227.

Yang, R., Yan, P., Wu, N., Sha, Z., and Liang, J. (2014). Application of avo analysis to gas hydrates identification in the northern slope of the south china sea. *Acta Geophysica*, 62(4):802–817.

Yun, T., Francisca, F., Santamarina, J., and Ruppel, C. (2005). Compressional and shear wave velocities in uncemented sediment containing gas hydrate. *Geophysical Research Letters*, 32(10).

Appendix A - Seismic modelling

When using the local-target PSDM simulator in the seismic modelling, a survey, background model and target needs to be defined. In the 3D model-builder viewer, it is possible to observe the setup for the simulation.

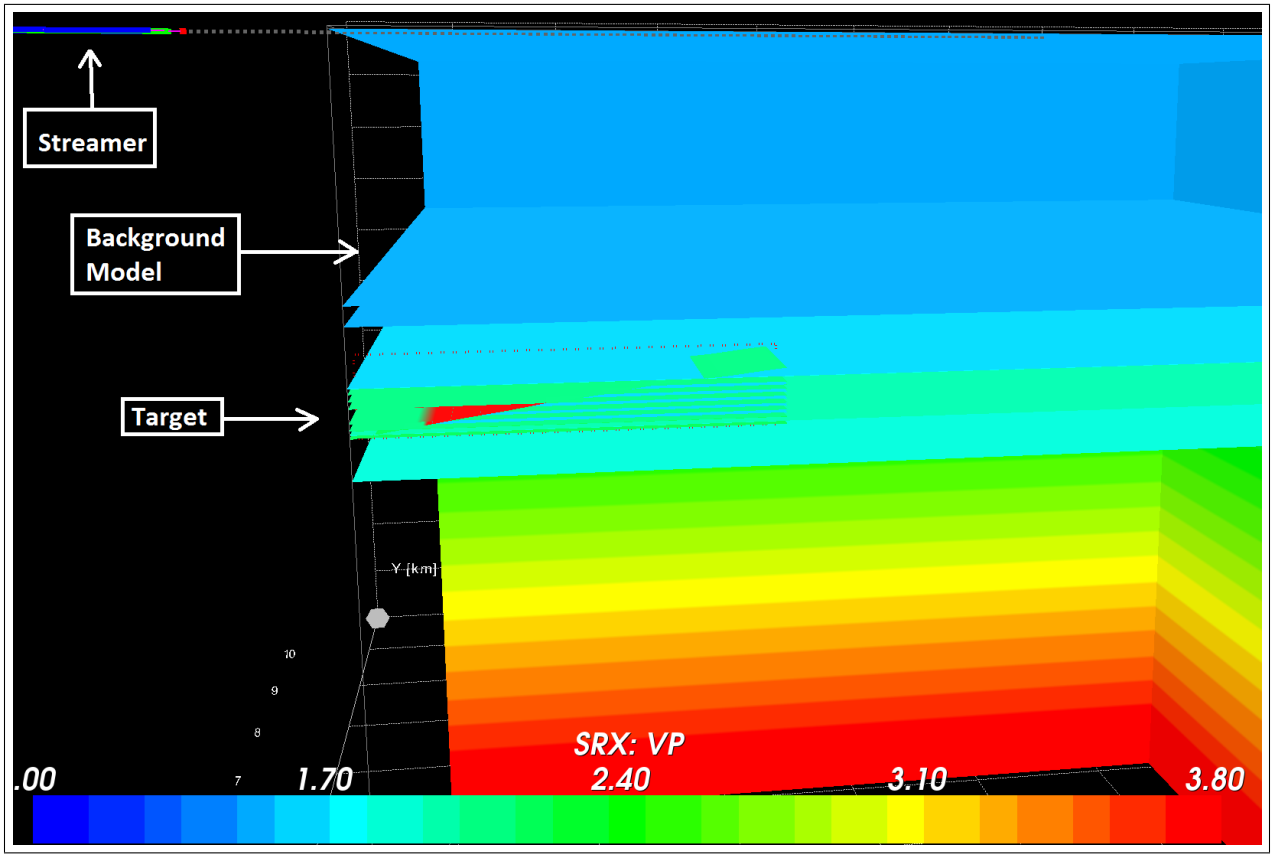

Figure 1: Setup for case 2. Showing the streamer and shots (stippled line), together with the background model and the target of interest. P-velocity is displayed for the background model and the target.

In Figure 1, the setup for case 2 is outlined. Showing the streamer with the associated shot configuration, overlying the background model and target. The background model have been created using a grid-layer cake model, with constant velocity above and at the target, but with increasing velocity with depth below. Surrounding the target, red dots mark the working box, where the reflectivity and PSDM filters are calculated. The large

gas hydrate accumulation with 100% saturation for scheme 1, can be observed as the area with high P-velocity (red).

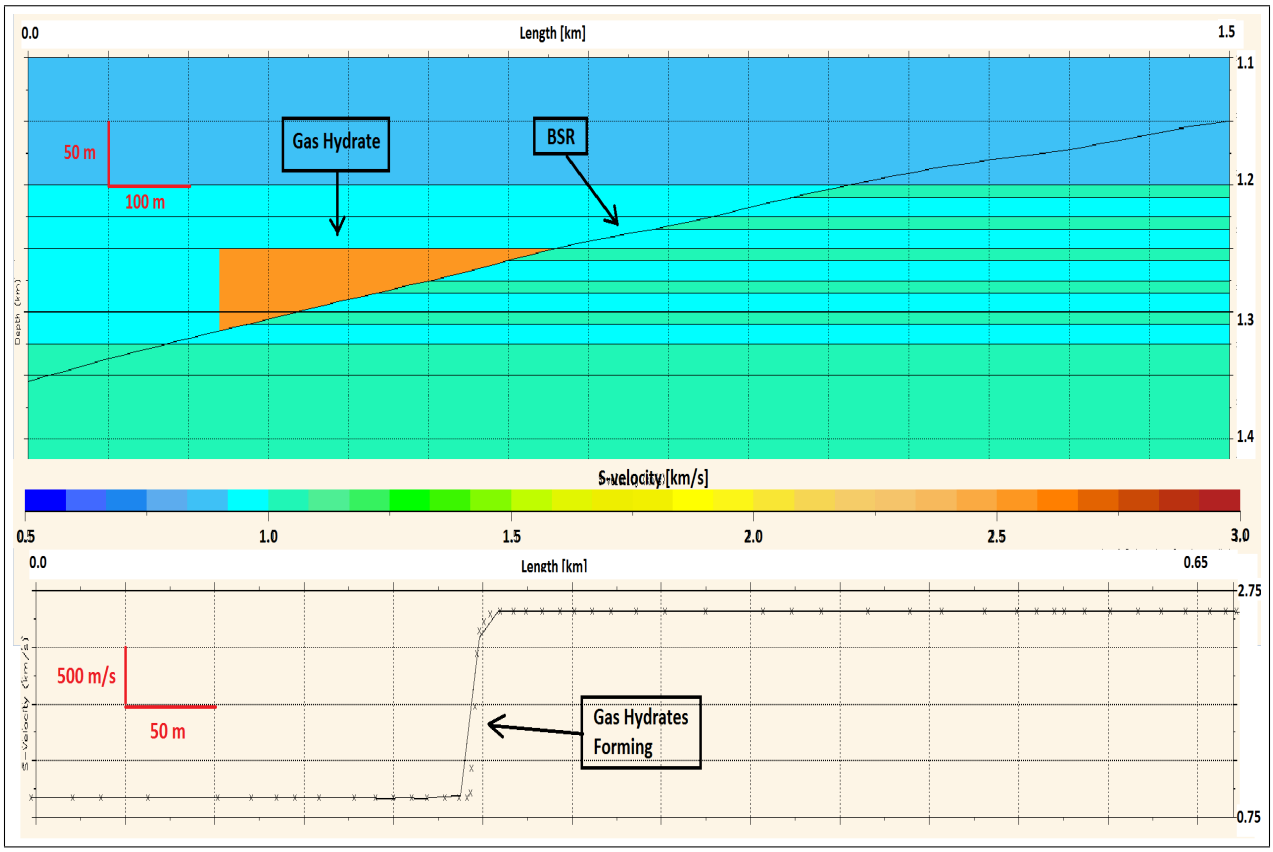

Figure 2: S-velocity assigned to the geological model, with the sampled function assigned to the gas hydrate saturated layers. Model is for 100% gas hydrate saturation (scheme 1).

In case 2, a sampled function is assigned to the gas hydrate saturated layer. In Figures 2 and 3 the density and S-velocity for the model are displayed. The gas layers have lower density than the fully brine saturated layers. The S-velocity is somewhat similar, but observed to be slightly higher for the gas saturated sediments due to the lower density. The sampled function for the density show that the 100% gas hydrate saturated layer have lower density than the fully brine saturated layers. The sampled function for the S-velocity show similar behavior as observed in the rock physics model (Figure 5.2a). For case 3, the setup is similar, but with different velocity for layers in the background model (Figure 4). The background model is assigned velocity and density properties based on the velocity chart (Figure 4.3) of Bünz et al. (2005). The target is smaller, in order to

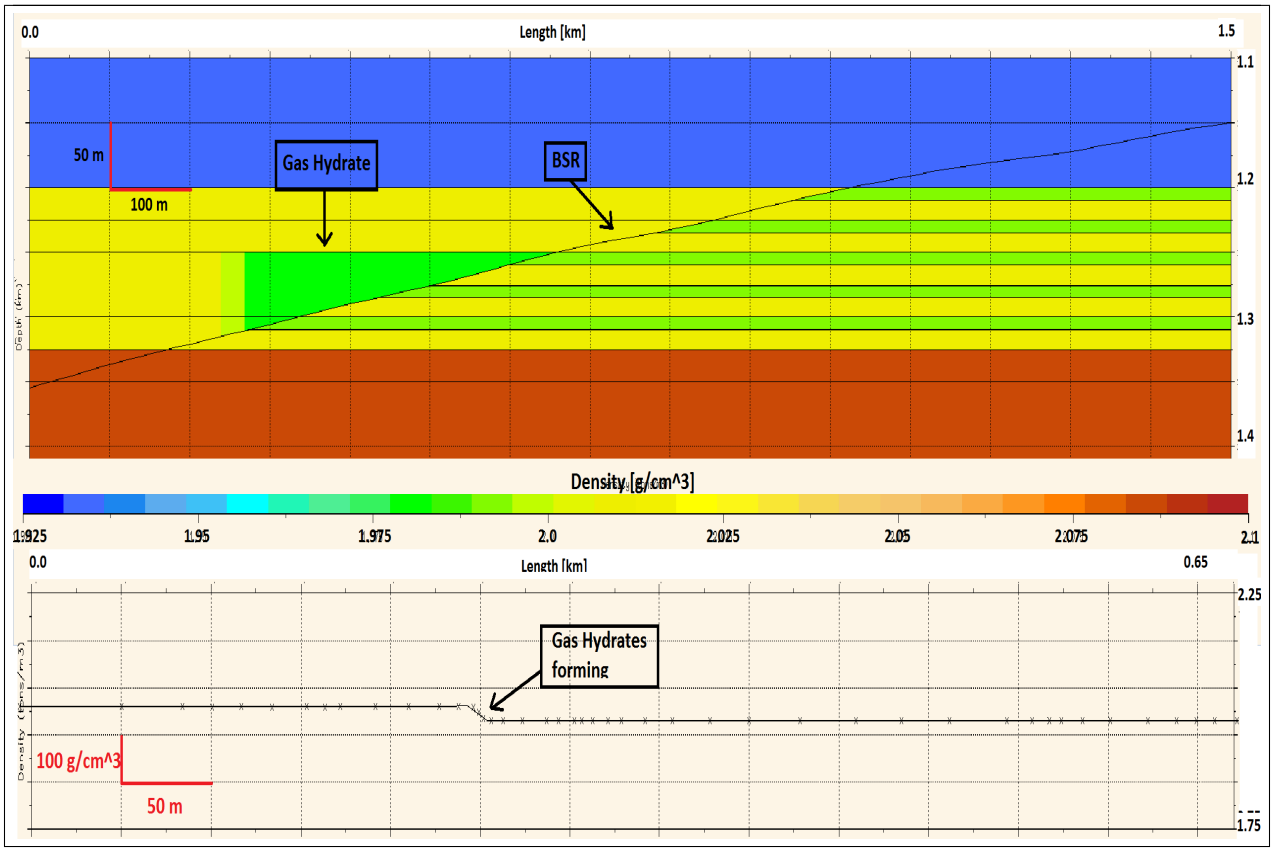

Figure 3: Density assigned to the geological model, with the sampled function assigned to the gas hydrate saturated layers. Model is for 100% gas hydrate saturation (scheme 1).

observe the BSR proper reflection.

In Figure 5, the geological model for case 3 have been simulated for a 85 Hz wavelet, but with a sampling of 12.5 m horizontally, and 5 m vertically. The sampling is similar to the real seismic acquisition, coinciding with CDP distance, or binning distance. The reflections are aliased, interfering with each other, and are unable to account for the varying lateral interfaces. The associated PSDM filter is displayed in Figure 6. It can be observed that alot of the seismic energy is lost, due to the coarse sampling. The result is a distorted seismic image, with aliased reflections. Figures 5 and 6, shows how important it is to select an appropriate sampling in the 2D convolution modelling method.

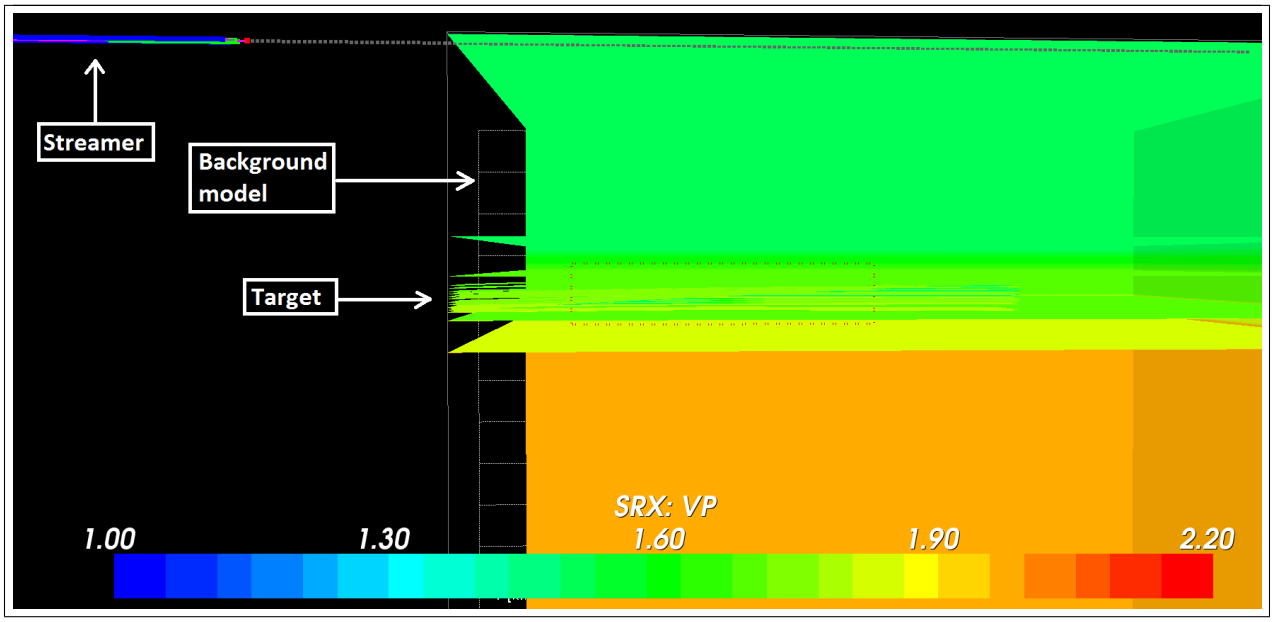

Figure 4: Setup for case 3. Showing the streamer and shots (stippled line), together with the background model and the target of interest. P-velocity is displayed for the background model and the target.

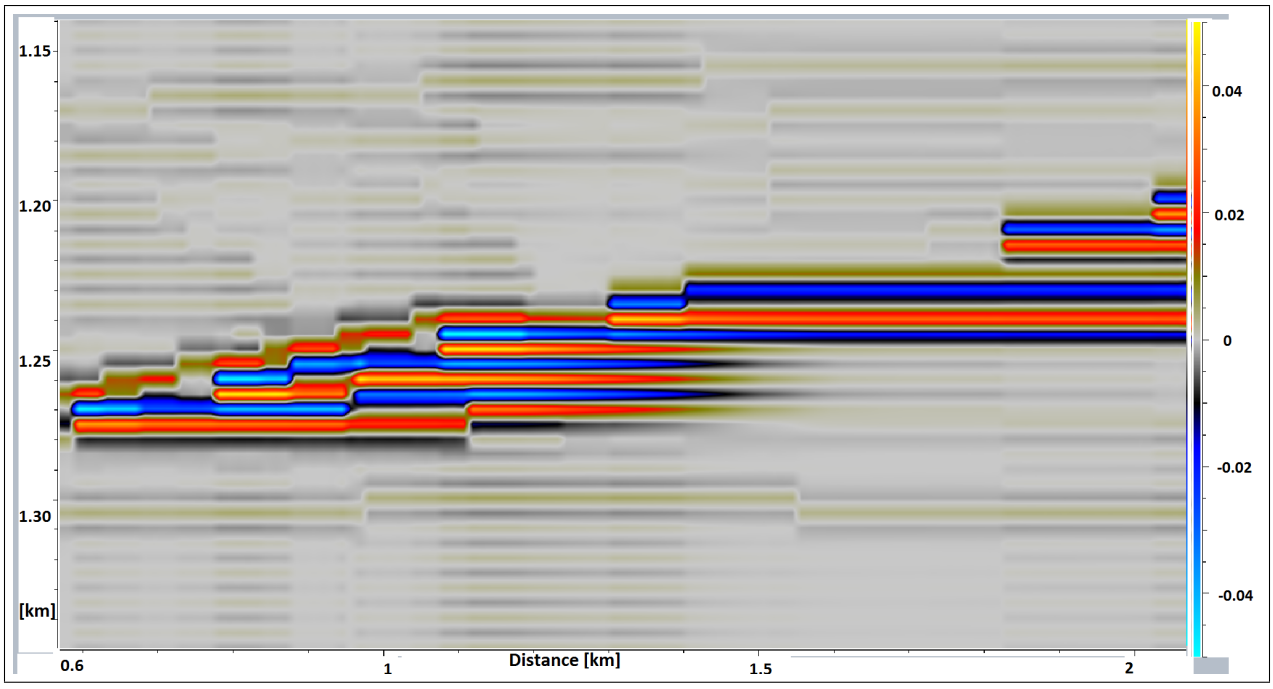

Figure 5: Seismic image showing distorted and aliased reflections. Sampling is to coarse for a 85 Hz wavelet.

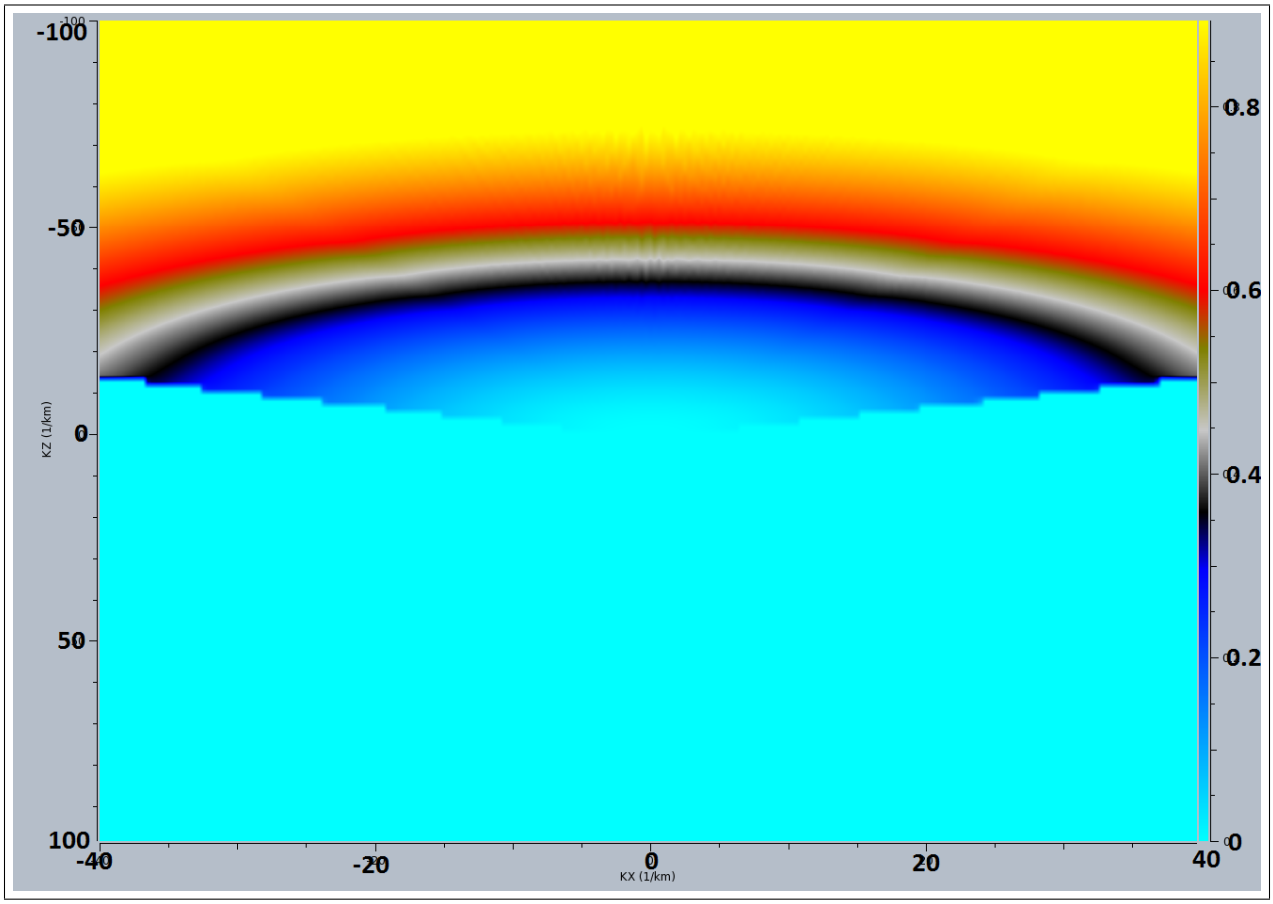

Figure 6: PSDM filter for 85 Hz, case 3. Sampling is 12.5 m horizontally and 5 m vertically.

Appendix B - MATLAB scripts and definitions

During the MATLAB modelling, scripts for various rock physics equations was utilized. A MATLAB package with equations and models was provided by Erling Jensen and Åsmund Drottning (Rock Physics technologies). The self-consistent methods used in this thesis was found by modifying a script written by Berryman (1980). The contact-cement theory scripts was modified using a script written by Dvorkin et al. (1999). All other scripts used to calculate Hertz-Mindlin, Gassmann equation, Hill, Reuss and Voigt was found in the MATLAB package.

Definition of S_n and S_τ

S_n and S_τ are proportional to the normal and shear stiffness of cement situated between two grains (Ecker et al., 1998). The normal and shear stiffness parameters depend on the amount of gas hydrate cement at grain contact (scheme1), enveloping grains (scheme 2), and pure gas hydrate. The normal stiffness S_n is defined as,

$$S_n = A_n(\Lambda_n)\alpha^2 + B_n(\Lambda_n)\alpha + C_n(\Lambda_n) \tag{1}$$

$$A_n(\Lambda_n) = -0.024153\Lambda_n^{-1.3646} \tag{2}$$

$$B_n(\Lambda_n) = 0.20405\Lambda_n^{-0.89008} \tag{3}$$

$$C_n(\Lambda_n) = 0.00024649\Lambda_n^{-1.9864} \tag{4}$$

and the shear stiffness S_τ is defined as,

$$S_\tau = A_\tau(\Lambda_\tau, \nu)\alpha^2 + B_\tau(\Lambda_\tau, \nu)\alpha + C_\tau(\Lambda_\tau, \nu) \tag{5}$$

$$A_\tau(\Lambda_\tau, \nu) = -10^{-2}(2.26\nu^2 + 2.07\nu + 2.3)\Lambda_\tau^{0.079\nu^2+0.1754\nu-1.342} \tag{6}$$

$$B_\tau(\Lambda_\tau, \nu) = (0.0573\nu^2 + 0.0937\nu + 0.202)\Lambda_\tau^{0.0274\nu^2+0.0529\nu-0.8765} \tag{7}$$

$$C_\tau(\Lambda_\tau, \nu) = 10^{-4}(9.654\nu^2 + 4.945\nu + 3.1)\Lambda_\tau^{0.01867\nu^2+0.4011\nu-1.8186} \tag{8}$$

where Λ_n, Λ_τ and α is defined as,

$$\Lambda_n = \frac{2\mu_H}{\pi\mu}\frac{(1-\nu)(1-\nu_H)}{1-2\nu} \quad , \quad \Lambda_\tau = \frac{\mu_H}{\pi\mu} \quad \text{and} \quad \alpha = \frac{a}{R} \tag{9}$$

In Equation 9 μ_H and ν_H is the shear modulus and poisson ratio of the gas hydrate, and μ and ν are for the grains, respectively. The parameter α is the ratio between the cemented contact radius (a), and the grain contact radius (R). It depends on the gas hydrate saturation (S), and the gas hydrate distribution at grain contact. For scheme 1, where gas hydrates cement at grain contact, α is given as,

$$\alpha = 2\left[\frac{S\phi_0}{3n(1-\phi_0)}\right]^{0.25} \tag{10}$$

and for scheme 2, where gas hydrate cement evenly envelopes grains,

$$\alpha = \left[\frac{2S\phi_0}{3(1-\phi_0)}\right]^{0.5} \tag{11}$$

Where n is the coordination number, and ϕ_0 is the initial porosity. The procedure described in this section, have been found in Ecker et al. (1998) and Dvorkin et al. (1999).

Definition of P_{mi} and Q_{mi}

The parameters P_{mi} and Q_{mi} are tensors, depending on the elastic properties of the host medium (H), and the inclusion material (GH = Gas hydrates, D = dry voids) (Johansen et al., 2003). Definition of P and Q depends on the inclusion shape. This study only utilize spherical inclusions, and the reader is referred to Mavko et al. (2009) in order to find P and Q equations for other inclusion shapes.

Here i denotes which material the parameters are chosen for (i = H,GH,D), and m denotes the yet-unknown effective host material. They are used in the SCA method, and are defined as,

$$P_{mi} = \frac{K_m + (4/3)\mu_m}{K_i + (4/3)\mu_m} \tag{12}$$

$$Q_{mi} = \frac{\mu_m + Z}{\mu_i + Z} \tag{13}$$

where the bulk and shear modulus denoted m, is for the effective background medium calculated using iteration. The parameter Z, is defined in Equation 3.24. The procedure have been outlined by Dvorkin et al. (1999).